Ida Hilde Gunleiksrud

Brittle Deformation in Central Telemark, South Norway, Unravelled by Remote Sensing, Field Structural Analysis and Magnetic Modelling

Master's thesis in Petroleum Geosciences and Engineering
Supervisor: Espen Torgersen
January 2019

Master's thesis

NTNU
Norwegian University of Science and Technology
Faculty of Engineering
Department of Geoscience and Petroleum

NTNU
Norwegian University of Science and Technology

NORGES GEOLOGISKE UNDERSØKELSE
NGU

Ida Hilde Gunleiksrud

Brittle Deformation in Central Telemark, South Norway, Unravelled by Remote Sensing, Field Structural Analysis and Magnetic Modelling

Master's thesis in Petroleum Geosciences and Engineering
Supervisor: Espen Torgersen
January 2019

Norwegian University of Science and Technology
Faculty of Engineering
Department of Geoscience and Petroleum

NTNU
Norwegian University of
Science and Technology

PROBLEM

1) How can the complex fault and fracture pattern of the bedrock in the Drangedal and Nome municipalities be described through a study of structural field data and be used to understand the regional brittle deformational framework?
2) What causes magnetic low signatures of lineaments in Drangedal and Nome municipalities?

ABSTRACT

The morphology of old and deeply eroded geological terranes are often controlled by abundant fracturing and faulting that reflects their long and often complex deformational history. This study investigates the brittle structures of one such terrane – the Sveconorwegian bedrock in the Drangedal and Nome municipalities, Central Telemark – with the aim to unravel the brittle deformational history of the area. The studied structures are investigated in a multidisciplinary and multiscalar approach comprised of (1) a remote sensing lineament study using high-resolution topographic and aeromagnetic data, (2) a structural study of field-data, and (3) an investigation of the magnetic signatures of the lineaments.

During the lineament study, which was carried out as a separate project (Hilde Gunleiksrud, 2017), nearly 9000 lineaments were identified and separated into three fault populations based on their orientations; (1) NE–SW, (2) NNW–SSE, and (3) NW–SE. Analysis of field data show a good correspondence with the remote sensing results, and provides the necessary structural, kinematic and environmental information to further constrain the fault populations into respective deformational events. Paleo-stress inversion analysis using Win-Tensor allowed for three separate stress regimes to be determined; (1) NW–SE extension creating NE–SW striking normal faults, (2) E–W transpression related to mainly NE–SW striking dextral strike-slip faults, and (3) NE–SW extension creating NW–SE striking oblique normal faults. It is proposed that regime 1 is related to the collapse of the Sveconorwegian orogen, with Late Triassic reactivation, regime 2 to E–W compression during the Caledonian orogeny and regime 3 to the rifting of Rodinia and possible Permian to Triassic reactivation.

Several of the largest topographic lineaments are associated with a pronounced low magnetic anomaly on the aeromagnetic maps. By integrating geophysical-, petrophysical- and structural field data in a 2D model across such a lineament, it is proposed that the anomalous magnetic response is due to a combined effect of hydrothermal alteration and deep weathering which ultimately reduce the magnetization of the rocks within the lineament. The alteration and weathering processes within the lineaments is discussed in context with the proposed brittle evolution (of the studied area) and a general geomorphological evolution of the region.

ACKNOWLEDGEMENTS

This thesis marks the end of my 5-year degree in Petroleum Geoscience and Engineering at the Department of Geoscience and Petroleum, Norwegian University of Science and Technology (NTNU). The project has been funded by NTNU and the Geological Survey of Norway (NGU).

Firstly, I would like to thank my main supervisor, Espen Torgersen, for giving me the opportunity to write my thesis in co-operation with NGU and the BITE (Bedrock Infrastructure in Telemark) project. Espen, thank you for invaluable guidance throughout both my specialization project and thesis. It has been a great learning experience to work with you as my supervisor. I would also like to thank my co-supervisors, Marco Brönner and Tim Redfield. Marco, thank you for your great support and guidance, especially with the magnetic modelling in my thesis. Tim, thank you for great guidance regarding structural geology and incredible help throughout my field-work.

It has been inspirational and a great learning experience to be included in the BITE project team, both during the field-work in the spring of 2018 and while writing my thesis at NGU. Thank you to all the BITE team members, for taking the time to include me in your work and paying interest to my project. Bernard Bingen, thank you for your time and effort to modify your map-figures so I could use these in my project. Aziz Nasuti, thank you for helping me with geophysical data-sets and technical support with GM-SYS. Also, thank you to Arild Monsøy and Kjetil Eriksen at the thin-section laboratory at NTNU for preparing my thin-sections.

I would also like to thank my mom and dad for always supporting me and encouraging me throughout my years at NTNU, especially during this past semester when writing my thesis. To my dad, thank you for your great geological interest in my project, and taking the time to proof read my paper in detail. To my mom, thank you for valuable assistance with formatting – especially with my sources and EndNote.

TABLE OF CONTENTS

FIGURES

TABLES

ABBREVIATIONS

AM: Amphibolite

APFT: Apatite fission track

BITE: Bedrock Infrastructure in Telemark

BSD: Backscatter diffraction

CAT: Cataclasite

Chl.: Chlorite

C-S: Cambrian to Silurian lithologies (of the Oslo zone)

DTM: Digital Terrain Model

EDS: Electron dispersive spectrometer

Fv.: Regional road (Norwegian: Fylkesvei)

FS: Feldspar

GRA: Granite

GRAG: Granitic Gneiss

LiDAR: Light Detection and Ranging

Loc.: Locality

MINS: Mineral Resources in Southern Norway

NGU: The Geological Survey of Norway

NTNU: Norwegian University of Science and Technology

P-K: Porsgrunn-Kristiansand

R: Stress ratio

R': Modified stress ratio

Rv.: National road (Norwegian: Riksvei)

RMS: Root-mean-square error

SE: Secondary electron

SEM: Scanning Electron Microscope

1. INTRODUCTION

The surface of the Earth only displays a miniscule fraction of the vast geology concealed below. Nevertheless, it provides geologists with an incredible display of structural features that are of great importance in understanding the subsurface. These structures, such as faults and fractures, act as a bedrock's unique signature created through its lifetime of deformation. In a brittle environment, faults and fractures are amongst the most common structural features displayed in the crust. A *fracture* is defined as any brittle discontinuity in a rock-mass, whereas a *fault* is a fracture that has evidently accommodated displacement (Park, 1983). Such structures can be analysed and interpreted to obtain insight into the rock's brittle evolution. However, this may prove a challenge in highly fractured bedrock terrains affected by a long and complex deformational history. Nevertheless, a good understanding of the brittle deformation and its implications for both surface and sub-surface geology is of great importance in many geoscience fields such as neotectonic and seismic studies, analysis of slope stability, mineral and petroleum exploration and in the planning and building of infrastructure.

This master thesis aims to create an understanding of the history of brittle deformation of the bedrock in the Drangedal and Nome municipalities within the Telemark province, using remote sensing and structural field data. A conceptual model for the area's brittle deformational history is constructed based on fault character and kinematics analysed through a paleo-stress inversion. In addition, aeromagnetic data is utilized to give insight into fault zone properties from a geophysical point of view. Used in combination with in-situ petrophysical data, a 2D depth model is constructed to better understand magnetic anomalies associated to major linear structures found the studied area. This thesis is part of a larger geological investigation of the Nissedal-Drangedal-Nome area initiated by The Geological Survey of Norway (NGU).

The Drangedal and Nome area (Figure 1) has until recently been considered one of the poorest mapped areas in Norway with regards to the bedrock geology. The bedrock geology map currently covering this area was published in 1978 (Dons & Jorde, 1978), and is one of the oldest bedrock maps currently in use. Detailed mapping and studies of certain mineral occurrences, such as the Nissedal supracrustals and pegmatites (Miyawaki et al., 2015) have been conducted, but apart from this, the Drangedal and Nome area has until recently only been covered by reconnaissance-style mapping (e.g. NGU, 2017). As an attempt to improve our understanding of the geology of the Drangedal and Nome area, NGU has initiated the Telemark-based project, BITE (Bedrock Infrastructure in Telemark).

Prior to this thesis, a lineament study of the Drangedal and Nome area was conducted using terrain- and aeromagnetic data (Hilde Gunleiksrud, 2017). Results from this study give an overview of the linear features contained in the topographic surface and aeromagnetic signature, which likely represent faults and fractures. Although lineament studies can encompass a remarkable number of structural features, it has clear limitations in terms of detailed structural analysis. Such a detailed analysis is vital in characterizing stress accommodation in faults and fractures and to further associate this data to a deformational setting. Detailed fault and fracture characterization is performed in this thesis by analysis of structural field measurements and observations and by thin section analysis. Together with the results from the lineament study, this study provides a comprehensive and multi-scalar study of the brittle structures in Drangedal and Nome.

This study also explores the magnetic anomalies related to significant brittle bedrock structures by integrating geophysical-, petrophysical- and structural field data.

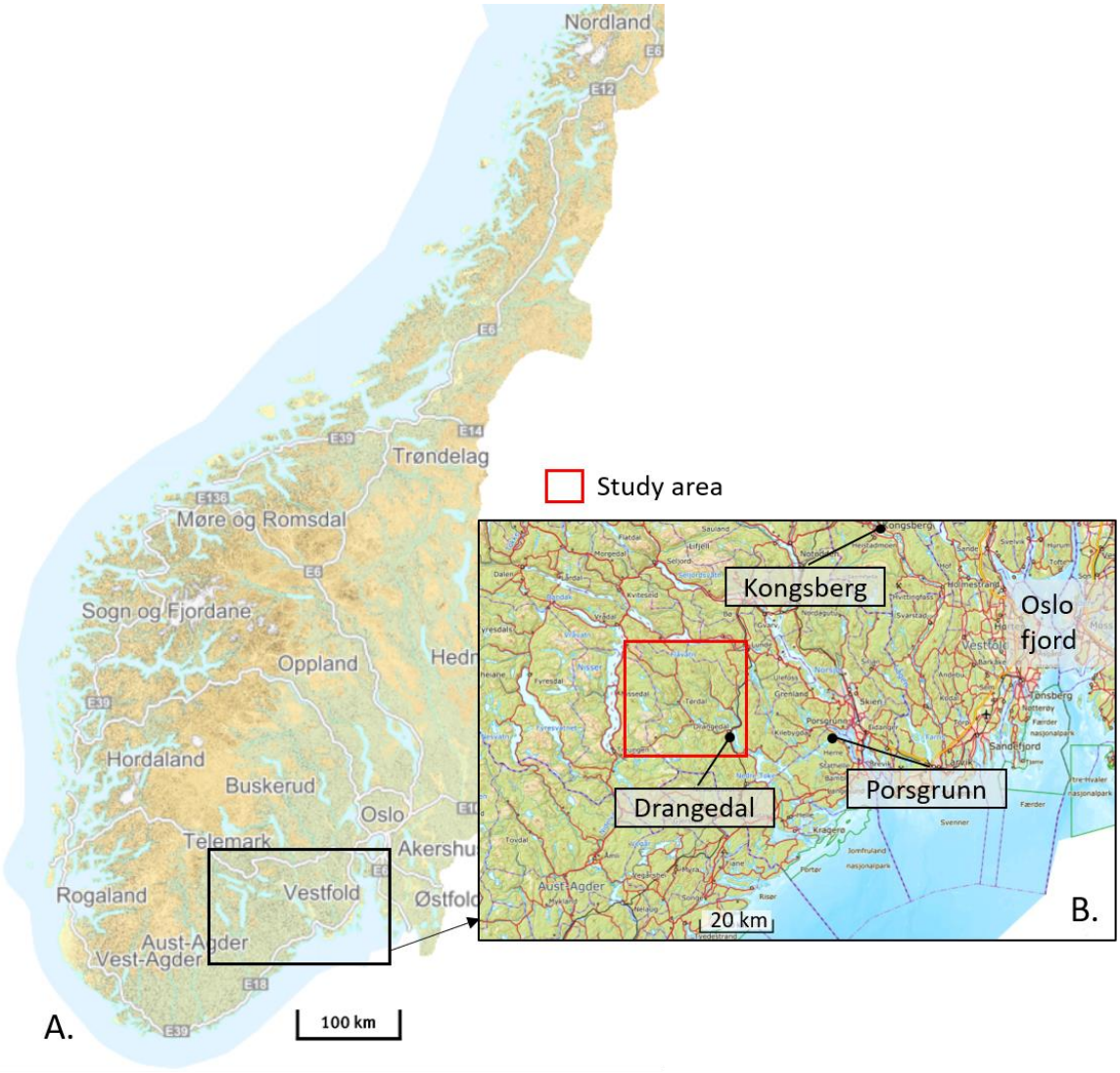

Figure 1. Overview map showing the geographic context of the studied area. A.) Southern Norway with B. as an excerpt to show the region wherein the studied area of Drangedal and Nome is located. B) Regional surroundings of the study area with the red square indicating the approximate location of the study area. Some large cities/towns in the region are also shown on the map. Both maps are taken from Kartverket (Kartverket, 2018).

2. GEOLOGICAL SETTING

The area studied in this project, the municipalities of Drangedal and Nome, is situated in the south-central part of Telemark, South Norway (Figure 2). Like the rest of the crustal basement in southern Norway, the Telemark (geographic) region is part of the Proterozoic basement formed through the Gothic and Sveconorwegian orogenies (Bingen et al., 2003; Fossen et al., 2007; Piper, 2009). Tectonically, the area belongs to the Telemarkia lithotectonic unit, which is dominated by Mesoproterozoic gneiss complexes in the south, by supracrustal successions in the north and granitic plutons throughout (Bingen et al., 2003). All these major constituents are present within the study area (Figure 2).

The earliest recorded geological event in southern Norway is the Gothic orogeny, which took place between 1650 and 1550 Ma as a result of oceanic crust subduction beneath the southwestern margin of the Fennoscandian shield (Fossen et al., 2007). The early phase of the orogeny hosted a period of strong volcanism and development of a high mountain range. A subsequent period of erosion of the Fennoscandian shield deposited thick packages of sediments, which through later modification and deformation would form the Paleo- and Mesoproterozoic terranes of the Proterozoic basement (Fossen et al., 2007; Piper, 2009).

Following the Gothic orogeny was a period of tectonic quiescence and transgression in southern Norway. Continued erosion of the Fennoscandian shield fed the deposition of sediments into the ocean covering southern Norway. These deposits, along with the magmatic domains from the period of rifting, are the origin of supracrustal complexes of Telemarkia shown by the dark green domains in Figure 3 (Fossen et al., 2007).

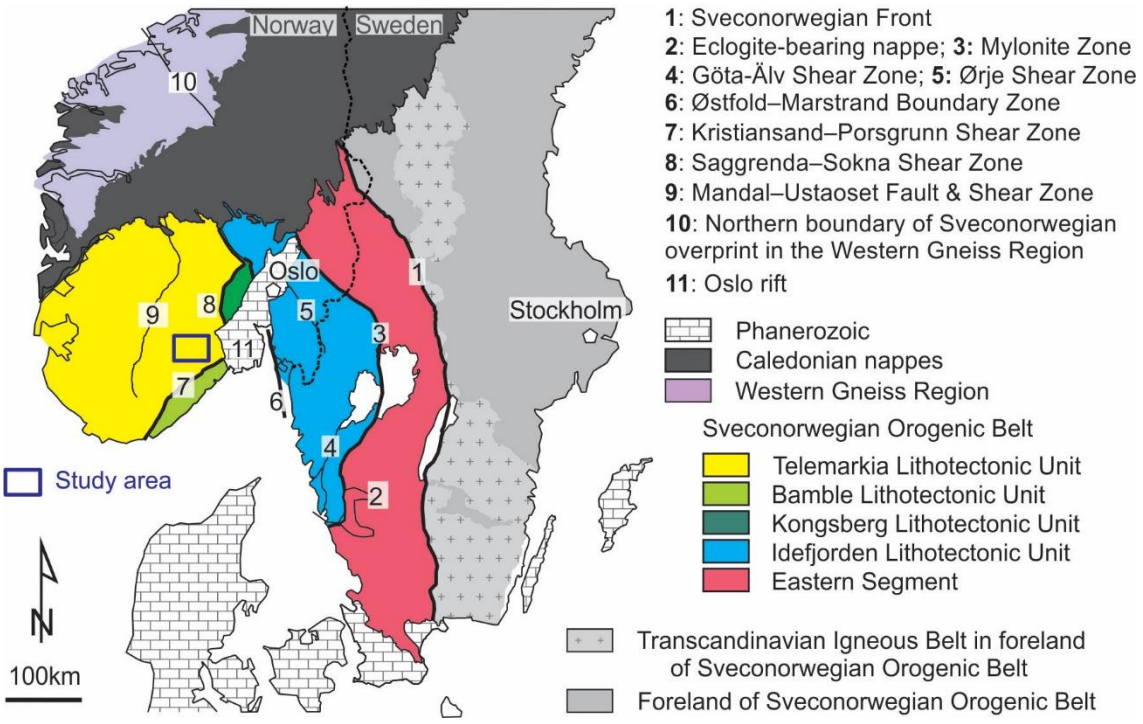

Figure 2. The Sveconorwegian province showing the five lithotectonic units of the Sveconorwegian Orogenic Belt. General location of the studied area is indicated by the blue rectangle. Map by Bingen (2018).

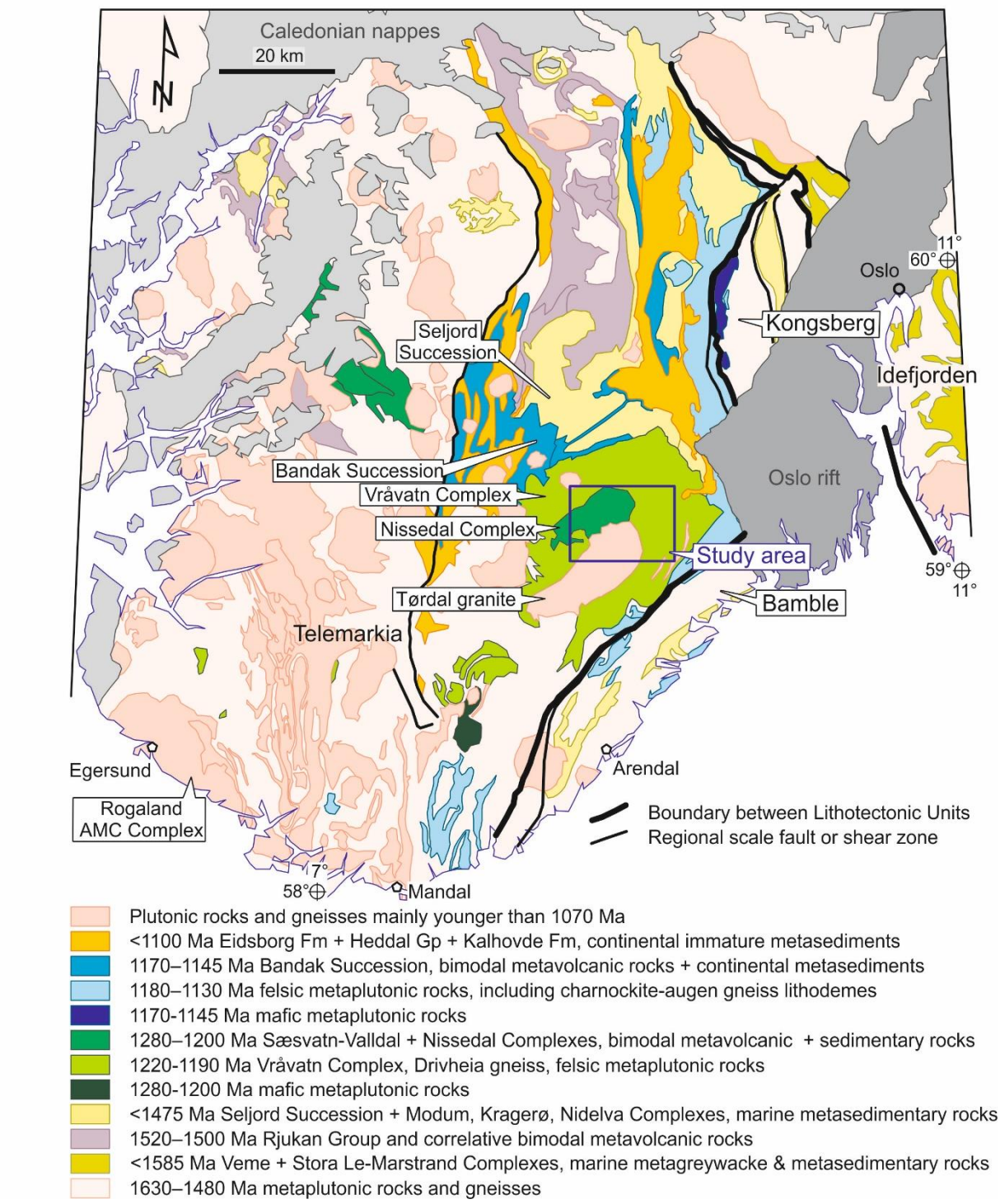

Figure 3. Southern Norway as the western part of the Sveconorwegian province. The map shows various constituents of the Telemark lithotectonic unit. Those of most relevance for the geological setting of this study are labelled. General location of the studied area is indicated by the blue rectangle. Map by Bingen (2018).

The Sveconorwegian orogeny occurred around 1190–950 Ma and was caused by subduction and continent collision along the western part of the Fennoscandian Shield (Bingen et al., 2003; Viola et al., 2011). The resulting Sveconorwegian belt is 500 km wide and extends from the coastal area of Rogaland in the west to central-southern Sweden in the east as seen in Figure 2. In the north, the belt disappears under the Caledonian nappes. The Sveconorwegian belt was formed during two main orogenic phases; the early phase (1190–1100 Ma) characterized by an extensional regime with

volcanic and magmatic activity, and a later phase (1030–950 Ma) characterized by a sinistral transpressive regime (Bingen et al., 2003; Piper, 2009). The latter accommodated the stacking of different lithotectonic domains onto the Fennoscandian foreland (Bingen et al., 2003).

The Telemarkia lithotectonic unit, wherein this study is located, consists of Mesoproterozoic gneiss complexes and large supracrustal sequences, as well as Early Neoproterozoic granitic plutons formed towards the end of the Sveconorwegian orogeny (Bingen et al., 2003) (Figure 3). The gneiss complexes of the oldest origin are part of the Proterozoic basement that was formed during the Gothian orogeny and later reworked during the Sveconorwegian orogeny. The supracrustal sequences are subdivided into the Rjukan, Seljord and Bandak successions and were formed in between the Gothic and Sveconorwegian orogeny. These were, like the gneiss complexes, deformed further during the Sveconorwegian orogeny (Spencer et al., 2014). The study area for this project consists mainly of granitic gneisses of the c. 1250 Ma *Vråvatn Complex*, structurally overlain by the *Nissedal Supracrustal Complex*, both of which were intruded by the *Tørdal granite* at c. 950 Ma (Andersen et al., 2007). Figure 3 shows this in a regional-geological setting, and Figure 4 shows the current bedrock geology for Drangedal and Nome municipalities and the surrounding area.

The southern part of the Telemarkia lithotectonic unit terminates against the Bamble lithotectonic unit (Figure 2, Figure 3). Bamble was juxtaposed against Telemarkia by the NE–SW *Porsgrunn-Kristiansand (P-K) shear zone* (Figure 4B). Movements along this shear zone may have begun as early as 1250 Ma with a sinistral shear (Piper, 2009), but were at least active as a thrust by c. 1140 Ma (Henderson & Ihlen, 2004). During the collapse of the Sveconorwegian belt, around 880 Ma, the zone was reactivated in a brittle and extensional manner (Mulch et al., 2005).

The western part of the Telemarkia lithotectonic unit (Figure 2) consists of a gneiss complex that was penetratively deformed and intruded by granitic plutons during the Sveconorwegian orogeny. The complex was intruded around 850 Ma by a swarm of NE–SW trending, vertical dikes – the *Hunnedalen dike swarm* (Walderhaug et al., 1999). In a regional tectonic context, this event is interpreted to reflect the initiation of rifting in Rodinia (c. 850 Ma) that would eventually lead to the opening of the Iapetus ocean (Li et al., 2008). The final phase of rifting is in southern Norway constrained by the c. 615 Ma WNW–ESE striking *Egersund dike swarm,* also situated in the western part of the Telemarkia lithotectonic unit (Bingen et al., 1998). Some evidence of mild extension further east in southern Norway has, however, been found to slightly postdate the emplacement of these dikes. The Fen complex is interpreted to have resulted from c. 580 Ma extension (Torsvik et al., 1996), and intrudes the Vråvatn complex east of the studied area, by the town of Ulefoss (Figure 4).

In the Ordovician, the NW–SE convergence between Baltica and Laurentia had begun. This convergence caused the closure of the Iapetus Ocean and the development of the Caledonides. A general NW–SE compression caused thrusting of nappe complexes onto the Baltic shield (Figure 2). (Hossack & Cooper, 1986). Hossack and Cooper (1986) locates the Caledonian front on the Fennoscandian shield and shows that the area of Drangedal and Nome is located close to the original front of orogenic activity. The Caledonian collision was followed by a period of extensional collapse (from c. 400 Ma) due to the overthickened and unstable crust. The earliest stages of the extensional collapse mainly reactivated pre-existing thrust faults, while later period of collapse was accommodated by steeper faults that extended into the basement domains (Gabrielsen et al., 2010).

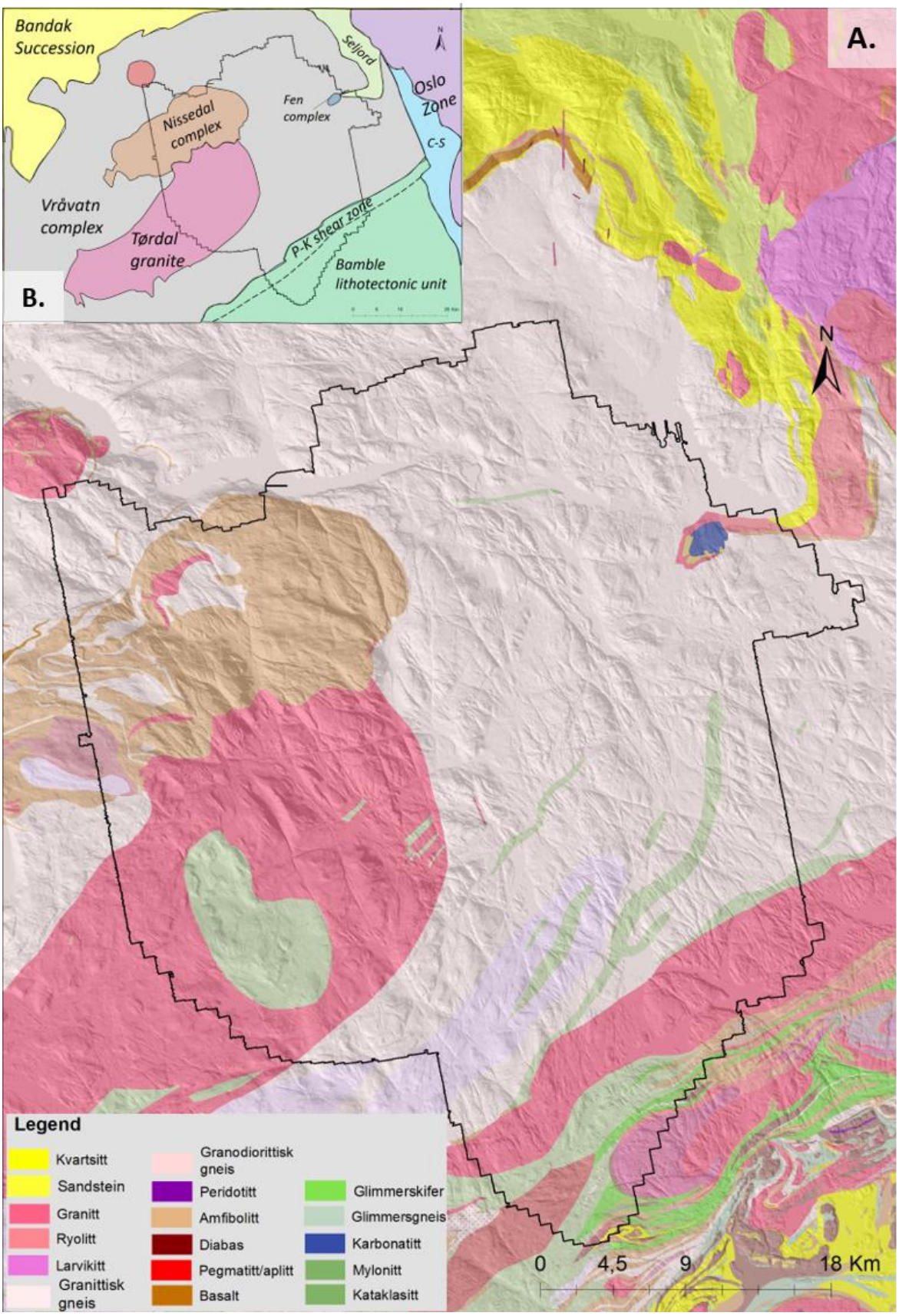

Figure 4. Bedrock geology of the Drangedal and Nome municipalities and the surrounding area. A.) Lithological map. The study area (Drangedal and Nome municipalities) is precisely outlined in black. B.) Overview of lithological complexes, successions and lithotectonic units of significance in this study. Seljord = Seljord Sucession. P-K shear zone = Porsgrunn-Kristiansand shear zone. C-S = Cambro – Silurian lithologies of the Oslo Zone.

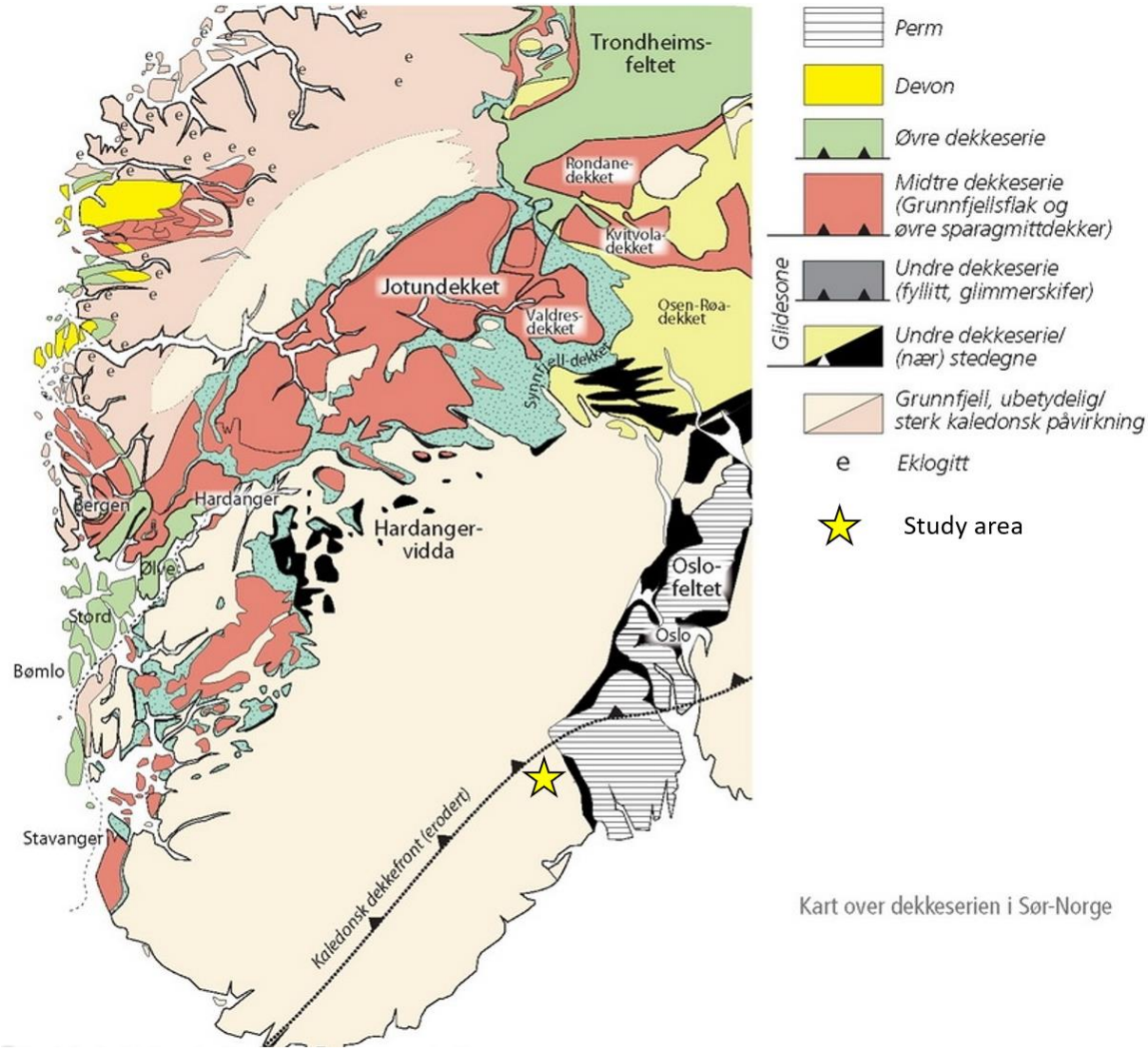

Figure 5. Tectonostratigraphical map of the allochtons in southern Norway. The (now eroded) paleo-front of the Caledonides is shown by the dashed line. The location of the studied area relative to the Caledonian front is indicated by the yellow star. Modified from Fossen et al. (2007).

The late Paleozoic and early Mesozoic hosted several stages of E–W to NW–SE-directed extension, creating structures like the Carboniferous–Permian *Oslo Graben* (R.H. Gabrielsen et al., 2010) and *Skagerrak Graben* (Gabrielsen et al., 2004) (Figure 6). Rifting was initiated in late Carboniferous, reaching a peak around 270 – 280 Ma, and ceasing in early Triassic (Heeremans & Faleide, 2004). The extension was likely initiated by dextral movements along the Sorgenfrei-Tornquist Zone (Figure 6) related to the Variscan Orogeny (Olaussen et al., 1994). The Oslo rift-zone borders the eastern margin of the Telemarkia lithotectonic unit; at the closest it is less than ten kilometres away from the study area. NNW–SSE trending Silurian lithologies (Figure 4B) by the town of Porsgrunn define this margin. The offshore segment of the rift, the Skagerak Graben, continues southeast-wards from the Oslo Graben, merging with the Sorgenfrei-Tornquist Zone in the south (Figure 6). A series of NE–SW striking half grabens characterize the graben structure (Neumann et al., 1991), and run parallel to the coastline of Telemark and southeastern Norway.

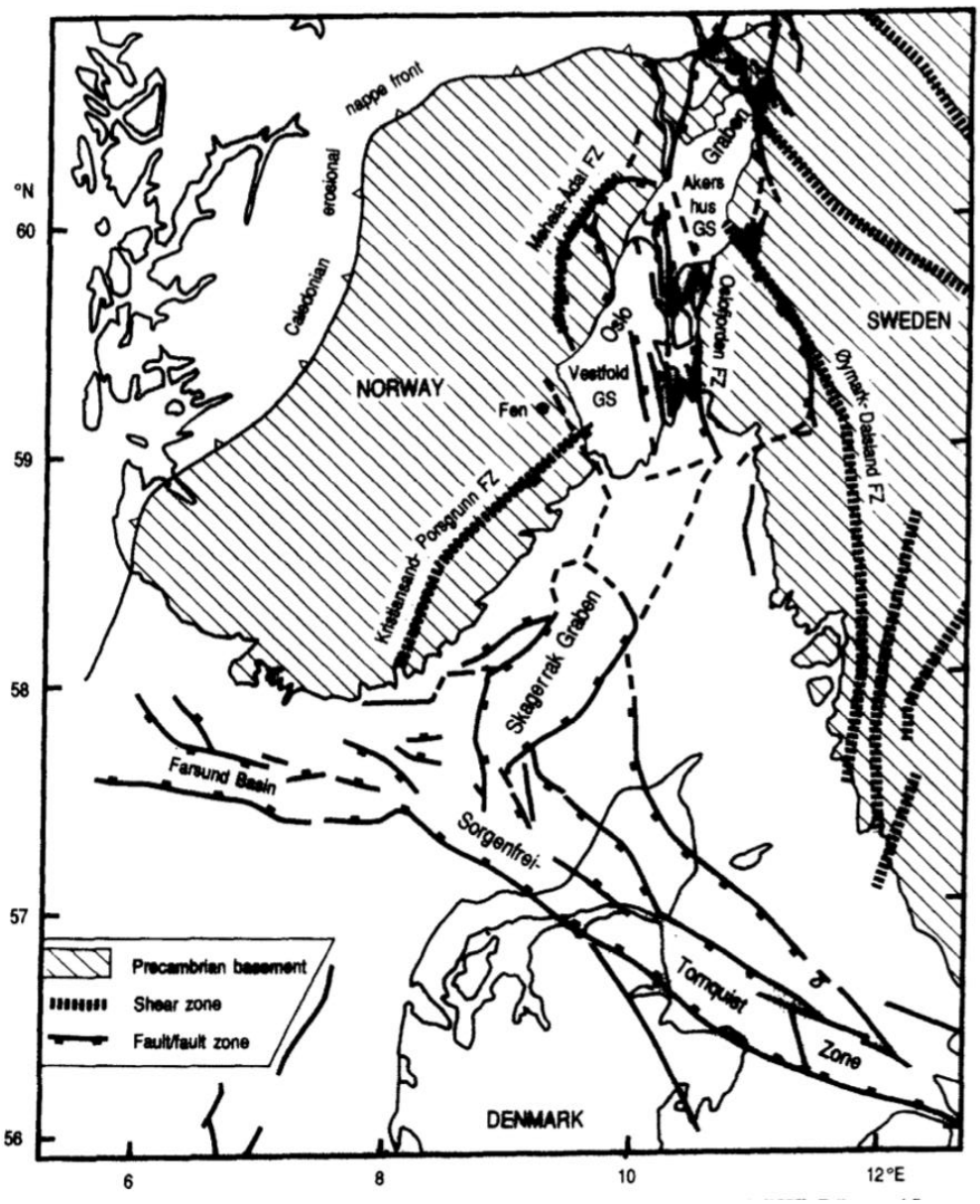

Figure 6. Overview of the Oslo Rift (with Oslo Graben and Skagerak Graben components) and the Sorgenfrei – Tornquist Zone seen in relation to southwestern Scandinavia. (Neumann et al., 1991)

Regional extension continued into the Triassic and early Jurassic, mostly influencing the southwestern coast of Norway and the North Sea (Scheiber & Viola, 2018), creating structures like the Viking Graben (Gabrielsen et al., 2017). Concurrently, a northward drift of Pangea and opening of the Tethys ocean caused a gradual change in the global climate – increasing humidity and atmospheric CO_2 concentration. In the late Triassic, basement rocks of southwestern Scandinavia were exhumed and exposed to the tropical climate, allowing an intense chemical weathering. Such in-situ weathering, *saprolitization*, produces clay assemblages at the expense of crystalline basement rock (Fredin et al., 2017). As proposed by Fredin et al. (2017), potentially large areas of Southwestern Scandinavia were affected by intense weathering in the late Mesozoic and Cenozoic. This left the basement covered in saprolitic sediments, which were later eroded in the Neogene and Pleistocene. Despite extensive glacial erosion, some saprolite occurrences are preserved in heavily fractured basement rock, as documented in southwestern Norway by Fredin et al. (2017) and in southern Sweden by Olvmo et al. (2005).

The surface relief of the bedrock in southern Norway, as it appears today, has been shaped by a period of continental uplift and erosion over the past c. 200 years (Lidmar-Bergstrom et al., 2000 ; Rohrman et al., 1995) with the Pleistocene glacial erosion marking the final stage of landscape formation (Vorren & Mangerud, 2007). However, the exact timing and mechanism of uplift and erosion is not fully agreed upon (Lidmar-Bergstrom et al., 2000). Based on apatite fission track analysis (AFTA), Rhorman et al. (1995) identified two periods of uplift and erosion in southern Norway; one during the Triassic to Jurassic and another starting in the late Oligocene. Together, these two periods of uplift and erosion were calculated to a vertical extent between 1.8 and 5 km (Rohrman et al., 1995). In south-eastern Norway, wherein this study is located, Pleistocene glacial erosion is assumed to follow patterns of an earlier fluvial erosion and account for c. 250 m of the total vertical erosion (Lidmar-Bergstrom et al., 2000 ; Vorren & Mangerud, 2007).

3. METHOD

3.1 Data

To build a solid understanding of the brittle deformational features of the bedrock in Drangedal and Nome, this study uses various sources of data; topographic and aeromagnetic data, structural field data and data from rock samples. This section describes how the various data is collected.

3.1.1 Remote sensing – lineament study

To obtain an overview and understanding of the general structural architecture and terrain morphology of the Drangedal and Nome area, a lineament study was carried out using Digital Terrain Models (DTMs) and aeromagnetic data. This study was conducted as a separate project (Hilde Gunleiksrud, 2017) in the fall of 2017, in cooperation with NGU and NTNU.

In the terrain interpretation, two DTMs were utilized; one with a resolution of 10 m, and another with a resolution of 1 m (Figure 7). The model with 10 m resolution is extracted from a national DTM that is mainly derived from an interpolation of mapped contour lines. The high-resolution model covers the entire municipalities of Drangedal and Nome and is compiled from newly acquired data using Light Detection and Ranging (LiDAR). To create a DTM with resolution of 1m, an average point (of measurement) density of 0.7 points/m^2 is used. The point clouds are then gridded by interpolation (Scheiber et al., 2015). Hillshading techniques were applied to the terrain models and interpretation was conducted in ArcMap at three map-scales; 1:250 000, 1:50 000 and 1:10 000.

The geophysical interpretation of the bedrock is based on high resolution aeromagnetic data acquired by NGU in 2013 and 2014 in conjunction with the MINS project (Rodionov et al., 2014; Stampolidis & Ofstad, 2014). Surveying was conducted by a helicopter-borne system flown at an average of 80 m above the terrain surface with a line distance of 200 m. The acquired data is gridded with a cell size of 50 x 50 m (Stampolidis & Ofstad, 2014) (Figure 8). Due to the restricted resolution of the aeromagnetic data compared to the terrain data, the interpretation is limited to a map-scale of 1:250 000.

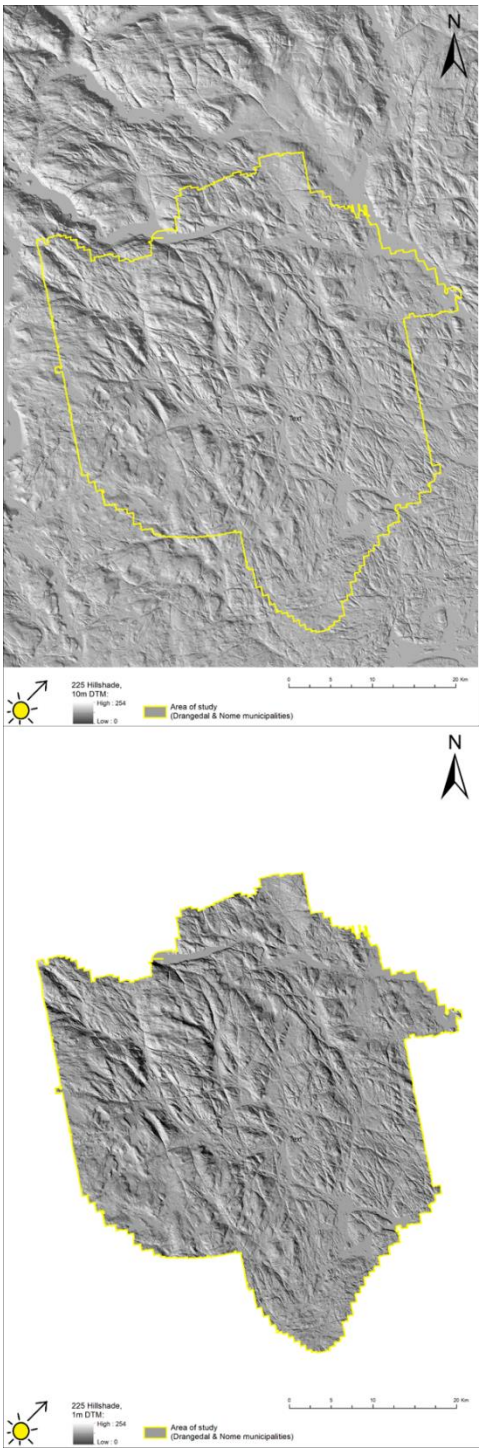

Figure 7 Digital terrain models (DTMs) with hillshade illumination from 225°. Upper: regional DTM with resolution of 10m. Lower: DTM constructed from high resolution LiDAR data with resolution of 1m. Area of study is outlined in yellow.

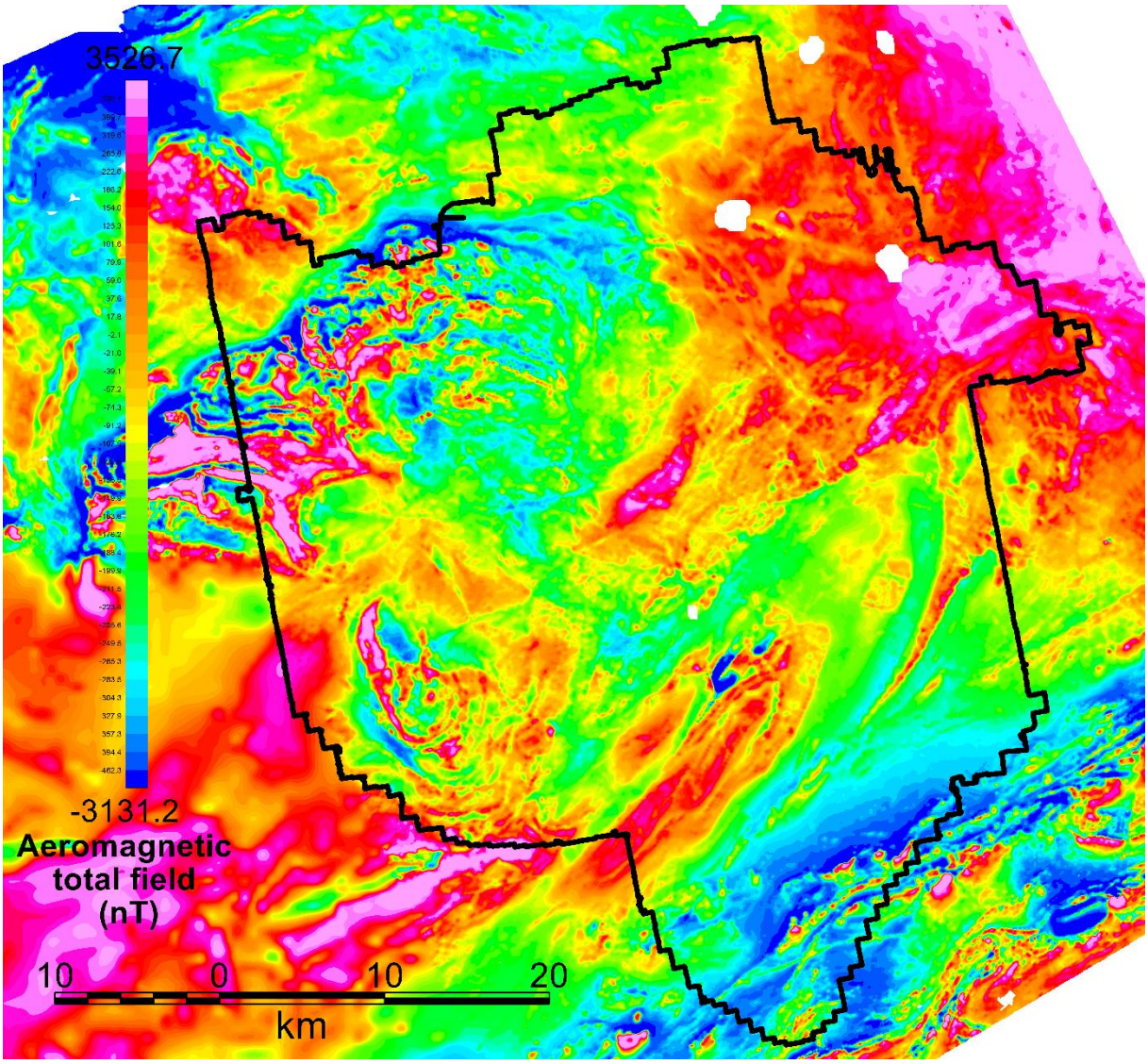

Figure 8. Aeromagnetic total field data covering the Drangedal and Nome municipalities. The studied area of Drangedal and Nome is outlined in black.

3.1.2 Field work – collection and observations of field structural data and samples

To understand the complex bedrock fault and fracture patterns created through a long (potentially up to 1200 Ma) period of brittle deformation, it is essential to do a detailed field investigation of the orientation, geometry, kinematics and mineralogical properties of brittle structural features. This information was collected through ten days of fieldwork in cooperation with the BITE project team from NGU in May/June 2018.

Field-data was collected within the area constrained by the high-resolution 1m DTM (Drangedal and Nome municipalities) and was focused on road-cut localities along roads Rv38, Fv109 and Fv302 (Figure 9). A total of 73 outcrops were studied. From these outcrops, structural data were collected, lithologies determined, fracture mineralogy analysed and fault characteristics (fault plane surface, fault rock type, fault width) described. Collecting structural data accounted for a significant part of the field work. It consisted of measuring dip and dip-direction of fault planes, fracture planes, foliation, igneous contacts and veins, measuring trend and plunge of lineations (slip-lines; slickensides, striations, grooves etc.), and determining kinematics where indicators could

be identified and interpreted. To differentiate between fault planes and fracture planes, the following criterium was used; if indicators of movement (lineations, displacement etc.) along the plane were apparent, the plane was determined to be a fault plane, whereas if these indicators were absent, it was registered as a fracture plane.

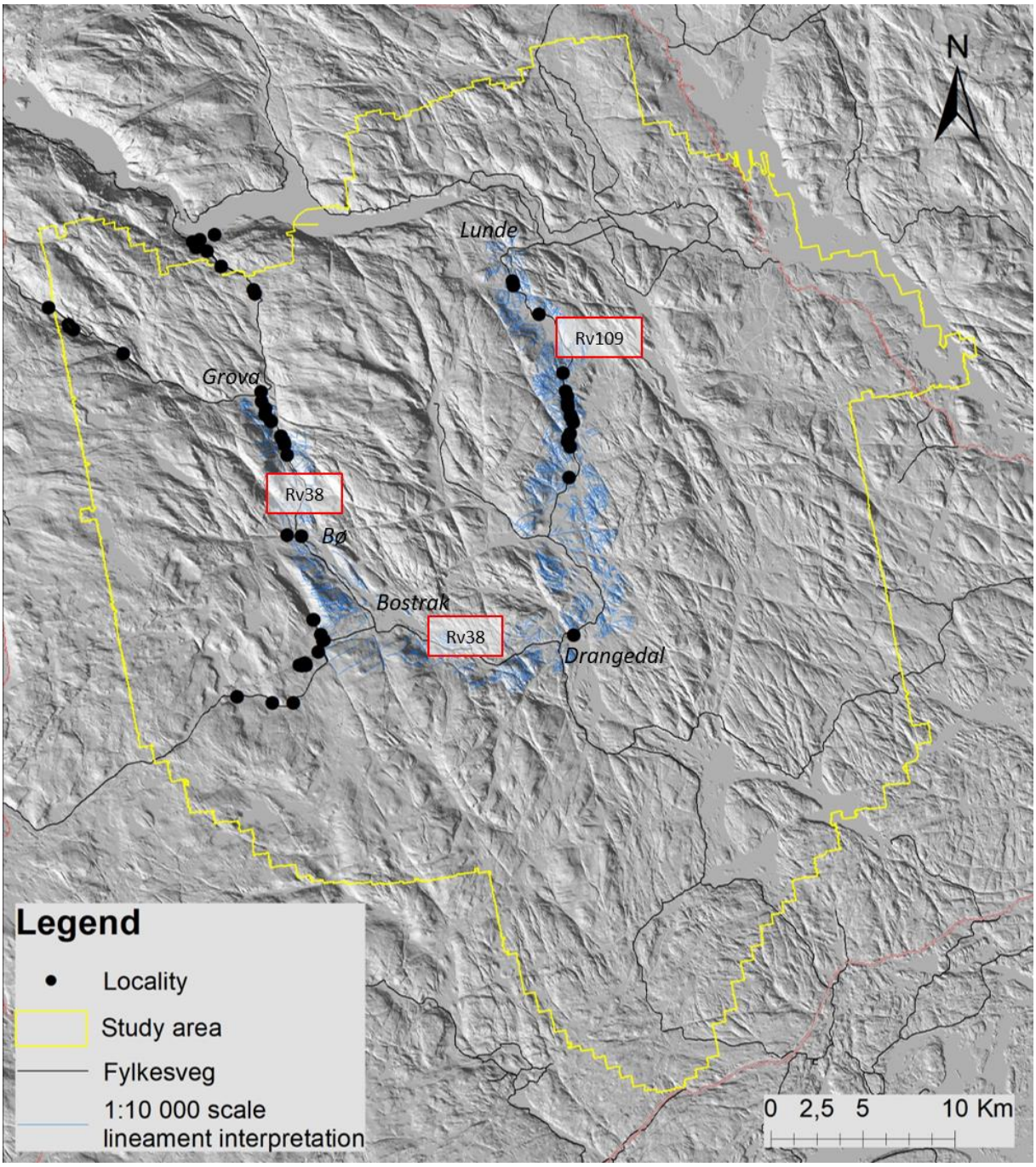

Figure 9. Overview of area where the field-work (mostly road-cut outcrops) was focused. Blue lines illustrate the lineament interpretation of the 1:10 000 scale (Hilde Gunleiksrud, 2017), which was also focused around the roads where the field-work was planned.

Field samples were collected for further structural, mineralogical and petrophysical analysis. Petrophysical sample acquisition and analysis is explained in detail in section 3.3. Structural samples were carefully oriented to ensure representativeness. Lineations on the fault plane together with one other suitable orientation (top-direction or a compass-direction) were used to systematically orient the samples. Structural and

mineralogical samples were mainly extracted from fault planes and fault zones, to supplement the field data in building an understanding of the fault systems.

The collection of data was registered digitally on a field-tablet with ArcGIS and the mapping extension Sigma created by British Geological Survey (BGS, 2015). Mapping for this study was mainly done by me, with occasional and valuable assistance from other NGU geologists in the BITE team. Other data collected through the BITE project that were relevant for this study have also been utilized in this thesis, with proper acknowledgement.

3.1.3 Sample preparation

Analysis of samples collected during field work provided valuable information beyond what was observable and measurable in the field. Samples for structural and compositional analysis through thin section microscopy, mineralogical analysis through SEM analysis, and samples for petrophysical analysis were prepared at the NGU laboratory in Trondheim.

Mineralizations on fault and fracture plane surfaces can provide important information about various syn- and post-deformational conditions (pressure and temperature conditions, fluid compositions etc.) and assist in temporally constraining the deformation. The mineralizations of fault planes were observed and described to the best effort in field. Further and more precise analyses of mineralizations through SEM and thin section analysis of samples collected at key localities provide data with higher accuracy and validity to be used in the study. The collected rock samples were cut to appropriate size (28mm x 48mm) at NGUs laboratory. Samples for microscopy analysis were prepared and polished into 30 µm thick thin sections by the thin section laboratory at NTNU. Field-orientations were transferred onto the cut and polished samples. Care was taken to preserve the edges of the thin section samples, as these edges often contained the fault (slip) plane and lineations, which are of most interest in the structural and kinematic analysis.

3.2 Analysis

A single measurement contains important data that can reveal significant information about an isolated location, rock or structure. However, to analyse the studied area altogether and identify prominent trends, these individual pieces of data need to be put into a system of organized analysis. This section describes how the analysis of data was carried out.

3.2.1 Thin section microscopy

A total of 11 thin sections were analysed using polarized-light microscopy with a Zeiss microscope at NGU. Prior to the analysis of each sample, an understanding of the thin sections field-orientation was obtained by going through field notes and measurements and relating those to the orientation-arrows on the thin section. Once a general understanding of the orientation was obtained, the samples were analysed for kinematic indicators associated with brittle deformation features. The most frequently observed structural features were *Riedel fractures* extending laterally out from the fracture planes, *grain drag* along fracture planes, *displacement of fractured grains, releasing bends, veins* and *shear fractures.* These features were described and photographed, and their kinematics were related to the field-observed kinematics where possible. The thin sections were also analysed mineralogically, with a primary focus of identifying mineralizations and potential signs of alteration associated with deformation.

3.2.2 Scanning Electron Microscope (SEM) Analysis

SEM imaging assisted in characterizing mineral assemblage of the fault plane surfaces and allowed for highly detailed surface morphology observations of the fault planes. Three slab samples were analysed in the Scanning Electron Microscope (LEO Electron Microscopy Ltd) at NGU. Scanning was operated in variable pressure, and the samples were imaged and analysed by Secondary Electron (SE) and Backscatter Diffraction (BSD). Backscatter Electron imaging provides image contrast as a function of elemental composition. Based on this, chemical composition analysis using Energy Dispersive X-ray Spectrometer (EDS) was determined. Element proportions were calculated using the INCA software (Oxford Instruments, 2018). The Secondary Electron imaging provides high-resolution imaging of fine sample-surface morphology. These images were mainly used to study the very fine details of the slickensides and lineations on the fault plane surfaces.

3.2.3 Structural data analysis

Analysis of the structural field observations forms the basis for understanding the structural evolution of an area. Since this study aims to understand the evolution of brittle deformation, field work focused on understanding the orientations, kinematics, chronology etc. of fractures and faults, and associated sub-structures.

The field-measurements represent a variety of structural features and characteristics. All structural data were available in ArcMap through the Sigma extension. A series of stereonet plots and rose diagrams were constructed in order to identify and analyse patterns and relationships between the structural features. For this analysis, the data was exported from ArcMap and separated into pairs of *fault planes* and associated *kinematic indicators* (where these were available), *fracture planes*, *foliation*, *igneous contacts,* and *veins*. As the faults provide the most structural information, these were further separated based on other characteristics like *sense of slip* (dextral, sinistral, normal, reverse or oblique), *plane surface mineralization and character*, and wall rock *lithology*. Once the structural data were separated and categorised, they were imported into the *Stereonet 10* software (Allmendinger, 2018) and plotted as stereonets, contour diagrams and rose diagrams.

3.2.4 Fault Slip Data Analysis and Paleo-stress Inversion

Brittle deformation originates from stresses in the earth's upper crust, most often due to tectonic forces. The stress field is a three-dimensional stress tensor consisting of three principal stress axes, σ_1, σ_2 and σ_3, where convention of $\sigma_1 > \sigma_2 > \sigma_3$ is implemented (J. Angelier, 1984). As the orientation and magnitude of the stress field changes, so will the orientation and kinematic properties of the resulting structures (faults, fractures, veins etc.). The kinematics of a fault are characterised by the *orientation of the fault plane*, the *orientation of the slip direction (slip-line)* and the *sense of slip*. Combined, these data form a *fault-slip datum* (Marret & Allmendinger, 1990). In attempts to relate fault-slip datums to the stress field present at the time of deformation, the *paleo stress regime*, various inverse paleo-stress methods have been developed. These methods are based on the principle that slip-lines (commonly slickensides) on a fault plane develop with an orientation that is parallel to the principal stress axis (σ_1) (Angelier, 1979). This applies both for fault-slip occurring under Andersonian conditions, where the fault plane is oriented optimally in response to the stress tensor, and fault-slip that is accommodated along a pre-existing plane of weakness (reactivation) (Angelier, 1984). In order for the paleo-stress inversion to be valid, the following assumptions are necessary; (1) the direction of movement is parallel to the shear stress on the faults, (2) the faults to not

interact, (3) the blocks bounded by the fault planes do not rotate, and (4) the stress field activating the faults is time-independent and homogenous (Nemcok & Lisle, 1995; Žalohar & Vrabec, 2007).

The paleo-stress inversion conducted in this study is based on fourteen selected key localities. For each locality, the various structural measurements were plotted into one common stereonet in the Win-Tensor software (Delvaux & Sperner, 2003). Win-Tensor is a program for processing structural field measurements to reconstruct the paleo stress field responsible for generating these structures. Orientations of fault planes and associated slip-lines (with kinematics) are essential in this inverse processing. Since field measurements commonly have some uncertainties, necessary adjustments were performed to ensure that slip-lines lie perfectly on the great circles of the fault planes.

Most fault planes measured contain slip-lines of some sort. Kinematic indicators, however, were not always identified. Initially, faults and slip-lines lacking kinematic information were entered in Win-Tensor without any kinematics. This generates stress tensors based on few fault-slip datums relative to the large available dataset of faults and associated 'non-kinematic' slip-lines. At least four sets of fault-slip datums are required in order to reconstruct a stress-tensor (Angelier, 1984). Moreover, statistical studies performed by Lisle et al. (2006) suggest that great care should be taken when analysing stress-tensors generated by eight or less fault-slip datums. In an effort to improve the statistical basis of the stress-tensor results in this study, kinematic information was assigned to the 'non-kinematic' slip-lines. The assigned kinematic was determined based on a fault's resemblance to other faults with known kinematics. Field notes were actively used in this process in order to minimize the error. Nevertheless, this process introduces an element of uncertainty in the paleo-stress analysis. By assigning three degrees of certainty (C-certain, P-probable or S-supposed) when entering the kinematic information into Win-Tensor, this uncertainty was recorded. If field observations provide strong kinematic indications – C was selected. In situations of weaker or more subtle kinematic indications – P was selected. Lastly, where kinematics are assigned to slip-lines of faults originally lacking kinematic indications, S was selected.

At localities containing structural measurements of noteworthy variation, structures were grouped into internally (near) homogenous *sub-sets* based on plane orientation, kinematic sense and plane surface character. These sub-sets were then plotted independently of one another. This approach allowed to investigate the varying sub-sets of each locality more accurately and to further distinguish between varying stress-fields. This, however, also created a wide range of potential stress-regimes for each locality, thus representing a very complex and geologically unrealistic deformational history. A trial-and-error approach was implemented to test various combinations of sub-sets, reducing the number of sub-sets to ultimately represent a more rational and viable deformational history based on fewer stress-regimes. When reproducing the paleo stress-field, the Win Tensor program also calculates the *angular deviation*; a quantification of the deviation in the computed stress-field due to the variability of slip-data. If the angular deviation was considered too large, the combination of the sub-sets was reconsidered - either tested together with other sub-sets or left as individual sub-sets. Note that the angular deviation was assessed individually for each sub-set, but a strict limit for deviation was not implemented. Various parameters should be considered when assessing the angular deviation for a single sub-set, such as number of measurements, the quality of measurements and the general character of the fault (or other structure) measured. For instance, an undulating fault plane will yield variable measurements

compared to a planar fault plane. Thus, a higher angular deviation should be permitted (and expected) for the situation with an undulating plane. Generally, however, the angular deviation of the merged sub-sets did not exceed 20°, with the exception of two sub-sets that produced deviations of around 30°. Once the sub-sets were combined and re-organized sufficiently, the 28 "new" sub-sets of all fourteen key localities were analysed together. Using the same approach as for the individual localities, the sub-sets were combined once again to create a total of 3 *sets* with associated paleo stress field tensors to represent the brittle deformation in the studied area as a whole.

Through the paleo-stress analysis, various parameters describing the stress regime at the time of deformation were calculated. Of greatest significance in this study are; a) the orientation of the three principal stress axis (σ_1, σ_2 and σ_3) and b) the stress ratios R and R'. These data were computed for each inverted sub-sets and sets. The *stress ratio, R*, is defined as $(\sigma_2 - \sigma_3)/(\sigma_1 - \sigma_3)$ and ranges in value from 0 to 3 (Scheiber & Viola, 2018). The *modified stress regime, R'*, is an aid to further classify the deformational regime. If R=R', the deformation is purely extensional and σ_1 is (sub-)vertical. In a compressional setting, where σ_3 is (sub-)vertical, R'=2+R. In a strike-slip regime, where σ_2 is vertical, R'=2-R. Further, R'-values can aid in determining the type of strike-slip regime. Values of R' ranging between 0.75 and 1.25 indicate a transtensive regime, while a transpressive regime is indicated by values ranging between 1.25 and 2.25.

3.3 Petrophysical data and analysis

Petrophysical data has a vital role in relating geophysical measurements to geology. In this study, aeromagnetic data are utilized together with *susceptibility data* from subsurface specimens to understand magnetic anomalies associated with brittle fault structures. Susceptibility is a petrophysical property that quantifies the ease at which a rock can be magnetized in the current magnetic field of the Earth (Hinze et al., 2013). Variations in susceptibility is the main driver in creating the magnetic anomalies seen in the aero-magnetic total field data (Figure 8). Some of the major linear topographic lineaments match magnetic lineaments of corresponding magnitude - expressed by a lower magnetic signature than its surroundings. To create this signature, a significant reduction of the susceptibility within the lineament is required. The susceptibilities of the rocks are considered to be most influential in creating the anomalous response.

Samples collected for petrophysical analysis provide necessary susceptibility values for modelling the 2D sections across magnetic lineaments. The aeromagnetic map was used to determine where the samples should be acquired. Several low-magnetic lineaments were investigated. However, due to vegetation and overgrowth, only a few of these lineaments provided outcrops of sufficient quality to collect representative samples. For each potential modelling profile, at least one sample was collected as close to the centre of the magnetic low as possible, and one or two samples were collected of pristine rock on either side of the lineaments. The samples acquired from the centre of the magnetic lineament should theoretically give significant lower susceptibility values than the bedrock samples collected outside of the magnetic lineament.

Petrophysical samples were cut with a diamond saw at NGU to ensure a proper sample size and fresh, un-weathered surfaces (for the pristine samples), in preparation for further analysis. The petrophysical laboratory at NGU analysed the samples for various properties through standard procedures (Olesen et al., 2010).

3.4 Magnetic modelling

Major fault zones are often associated with a reduction in magnetic susceptibility of the fault rock (Olesen et al., 2007). To explain this observation, two processes are discussed; deep weathering and hydrothermal alteration. *Deep weathering* is caused by the transport of meteoric water from the surface along fractures and faults in the bedrock. The meteoric water disintegrates the rock along the fracture planes, creating a zone of physically and chemically altered rock gradually growing laterally out from the fracture plane and gradually extending deeper along the fracture plane (Olvmo et al., 2005). Through the weathering process, silicate minerals like feldspar and mica are converted into clay minerals. The weathering process commonly results in wedge-shaped weathering profiles narrowing with depth. Deep weathering in tropical climates results in the formation of saprolite, which also involves the oxidation of magnetite to hematite, thereby reducing the magnetic susceptibility of the rock (Olesen et al., 2007). Susceptibility reduction as a result of *hydrothermal alteration* is also associated to the oxidation of magnetite to hematite. Hydrothermal alteration is caused by the circulation of O_2-rich fluids heated by a subsurface source; a magmatic system, the geothermal gradient, radioactive decay or metamorphic reactions. The fluids are either generated below the surface through magmatic, juvenile, or metamorphic reactions or by a slow percolation of meteoric water or seawater (Sharma & Srivastava, 2014). In a fault zone, the hydrothermal fluids exploit the permeable fractures, altering the surrounding rock. Thus, the degree of alteration in a fault zone depends greatly on the degree of fracturing. Meller et al. (2014) found through a study of hydrothermally altered zones in granite that the alteration zones surrounding fractures could reach a lateral extent to tens of metres. Assuming the alteration fluid is heated by a geothermal gradient or a deep magmatic source, the effect of hydrothermal alteration will be greatest at depth and likely produce a wedge-shaped profile narrowing towards the surface. Geometrically, this profile is a counterpart to the deep-weathering profile.

The total magnetic field response varies significantly within the studied area; mostly from values between -1000 nT and 1000 nT (Figure 10A). Consequentially, great variation in magnetic response is also observed along the various magnetic lineaments, and the lineaments are not always easy to detect. Filtering techniques are used to enhance various features in the observed magnetic total field. Miller and Singh (1994) developed the *tilt angle filter* (1) to identify transitions between high and low responses in the magnetic field, thereby delineating edges of magnetized structures as for instance magnetic lineaments. The tilt angle derivative is the ratio of the vertical derivative to the absolute value of the total horizontal derivative, *THDR* (2), of the magnetic field (Miller & Singh, 1994);

$$Tilt = tan^{-1}\left(\frac{\frac{\partial T}{\partial z}}{THDR}\right) \qquad (1)$$

where,

$$\mathrm{THDR} = \sqrt{\left(\frac{\partial T}{\partial x}\right)^2 + \left(\frac{\partial T}{\partial y}\right)^2} \qquad (2)$$

In this study, the tilt angle filter is applied to enhance magnetic anomalies associated to lineaments (Figure 10B). Yet, several long (10's of km) and very linear magnetic anomalies are easily detected also in the magnetic total field data, even without the tilt-derivative filter (Figure 10A). These are associated with major topographic lineaments

and have a pronounced magnetic response which is lower than expected, relative to the surrounding rocks.

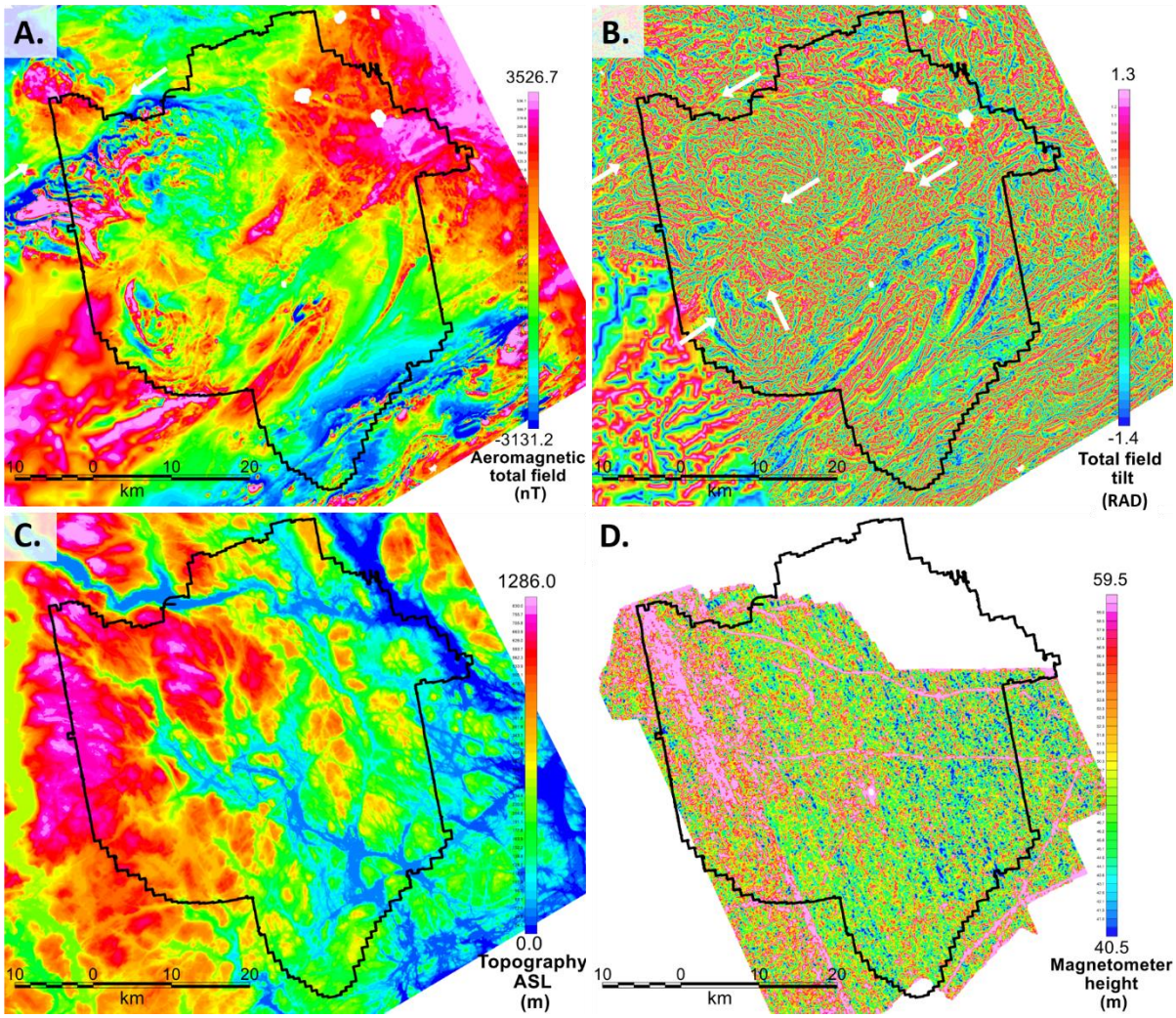

Figure 10. Geosoft grids used in the GM-SYS modelling of the magnetic anomaly. A.) aeromagnetic total field. B.) Tilt derivative of total field, a few magnetic lineaments are pointed out by white arrows. C.) Topography above sea level. D.) Magnetometer height (above topographic surface). The area of study is outlined in black.

As an attempt to describe the source of the distinctive signature associated with the pronounced magnetic lineaments, a 2D profile crossing a lineament is modelled in the GM-SYS extension of the Geosoft software Oasis Montaj (Geosoft Inc., 2015). Aeromagnetic data, topographic data and flight height data are utilized along with petrophysical data (susceptibility) from collected field samples and structural observations to create a model that is representative for the profile. Incorporating information and knowledge about the lithological and structural environment around this profile is essential in creating a model that is geologically viable.

The GM-SYS extension requires magnetic data, topographic data and "measuring-station" height as input parameters for a model setup. The magnetic data (Figure 10A) used for the modelling is extracted from the aeromagnetic dataset also utilized in the lineament study (see section 3.1.1 for details on acquisition), and has a resolution of 50 m. The applied topographic grid (Figure 10C) has a cell size of 25 m, and is based on data extracted from a national. Although the terrain grid has a higher resolution, the

resolution of the entire model is limited by the 50 m x 50 m resolution of the magnetic grid.

The total aeromagnetic field is measured by towing a magnetometer below a helicopter. The height of the magnetometer above the topographic surface represents the height of the so-called "measuring-stations" in the model. The magnetic field of a source decays with $1/r^3$, therefore the distance between the topographic surface and the magnetometer has a significant impact on the measured magnetic field. Although great effort was made to 'drape' the topography by maintaining a constant flight height above the topographic surface, variations in magnetometer height above the topography occur. To consider these variations during modelling, a grid representing the magnetometer height (above the topography) was made by subtracting the topographic grid from the magnetometer-height grid (derived from radar measured flight height data). Despite strong topographic variations, the helicopter generally succeeded in following the topographic variations, giving a relatively constant magnetometer height (Figure 10D). Greater variations (low- and high extremity of 40 m and 60 m) as illustrated in Figure 10D, are likely due to infrastructure like buildings or powerlines.

Lateral variations of magnetic properties create amplitude variations in the measured aeromagnetic field. Variations in bedrock mineralization from both surface and subsurface are the main cause of this effect - and is what this work aims at investigating. However, in airborne acquisition, major topographic depressions introducing increased volumes of air between the surface and aircraft *may* also account for part of this reduction. Through maintaining a near constant flight-height above the topography during the data acquisition (Figure 10D), this effect is minimized. Varying magnetometer heights that have an effect on the measured field, hereafter referred to as the *topographic effect*, are detected by comparing the magnetic response of a representative model with the topography calculated at the actual flight height to a constructed flight height that perfectly 'drapes' the topography. The difference between these two response-curves indicates a topographic effect in the measured data (see results, section 4.5.3, for more details). If significant, this effect needs to be accounted for when constructing the models.

Susceptibility values determined by the petrophysical analysis of field samples were used in the modelling of the lineament anomaly. An average susceptibility value for the samples of pristine (un-weathered) rock on both sides of the anomaly is utilized as a "background-susceptibility" in the model. The low-susceptibility value of weathered rock sampled close to the centre of the anomaly represents deep weathering in the model. Samples of cohesive rock with a low susceptibility were also collected close to the centre of the anomaly. Susceptibility values from these samples are assumed to represent hydrothermally altered rock in the model.

Susceptibility values are not necessarily lithology dependent and can vary greatly within a certain lithological body. In areas not affected by deep weathering and hydrothermal alteration, susceptibility variations are often caused by varying concentration and distribution of magnetite. Especially in metamorphosed bodies of rock, this property can vary greatly. A complex geometry of susceptibility distributions will create a fluctuating magnetic response, which can be a challenge when constructing the model. Due to the observed great variation of susceptibility within the granitic gneiss, associated to localized variations magnetite concentration, bodies of various susceptibilities were introduced in the model to mimic the magnetic response on either side of the magnetic

anomaly. This way, the lineament anomaly could be analysed and modelled independently of the surrounding rock properties.

Fault architecture of the model is constructed based on structural and petrophysical field observations at selected localities combined with a general theory of deep weathering and hydrothermal alteration within fault zones.

4. RESULTS

4.1 Remote sensing – lineament study

Through a remote sensing study of topographic and aeromagnetic data (Hilde Gunleiksrud, 2017) a comprehensive dataset of bedrock lineaments has been identified in the Drangedal and Nome study area (Figure 11, Figure 12). Analysis of the lineaments in terms of orientation, length and character resulted in the definition of three major lineament populations; NE–SW, NNW–SSE and NE–SW.

Generally, the lineaments identified in the aeromagnetic and topographic maps correspond well; all three lineament populations are recognized in both interpretations. This is largely a result of the well exposed bedrock in the study area. Despite the general correspondence, some deviations do occur. Situations in which magnetic lineaments lack and topographic lineaments are present are likely a result of limited resolution of magnetic data compared to topographic data, or that the lineaments are not associated with significant changes in the magnetic properties of the bedrock. Magnetic lineaments that lack corresponding topographic lineaments are likely not brittle structures, but instead either contacts between lithologies of contrasting magnetization without any corresponding topographic contrast, or plastic shear zones.

Several of the most pronounced topographic lineaments have a significant low magnetic signature. In addition, these lineaments are characterised by their long (10's of kilometres) and linear nature (see white arrows in Figure 13). Most of these lineaments trend NE–SW, but some also strike NNW–SSE. These lineaments are further investigated through modelling described in section 4.5.

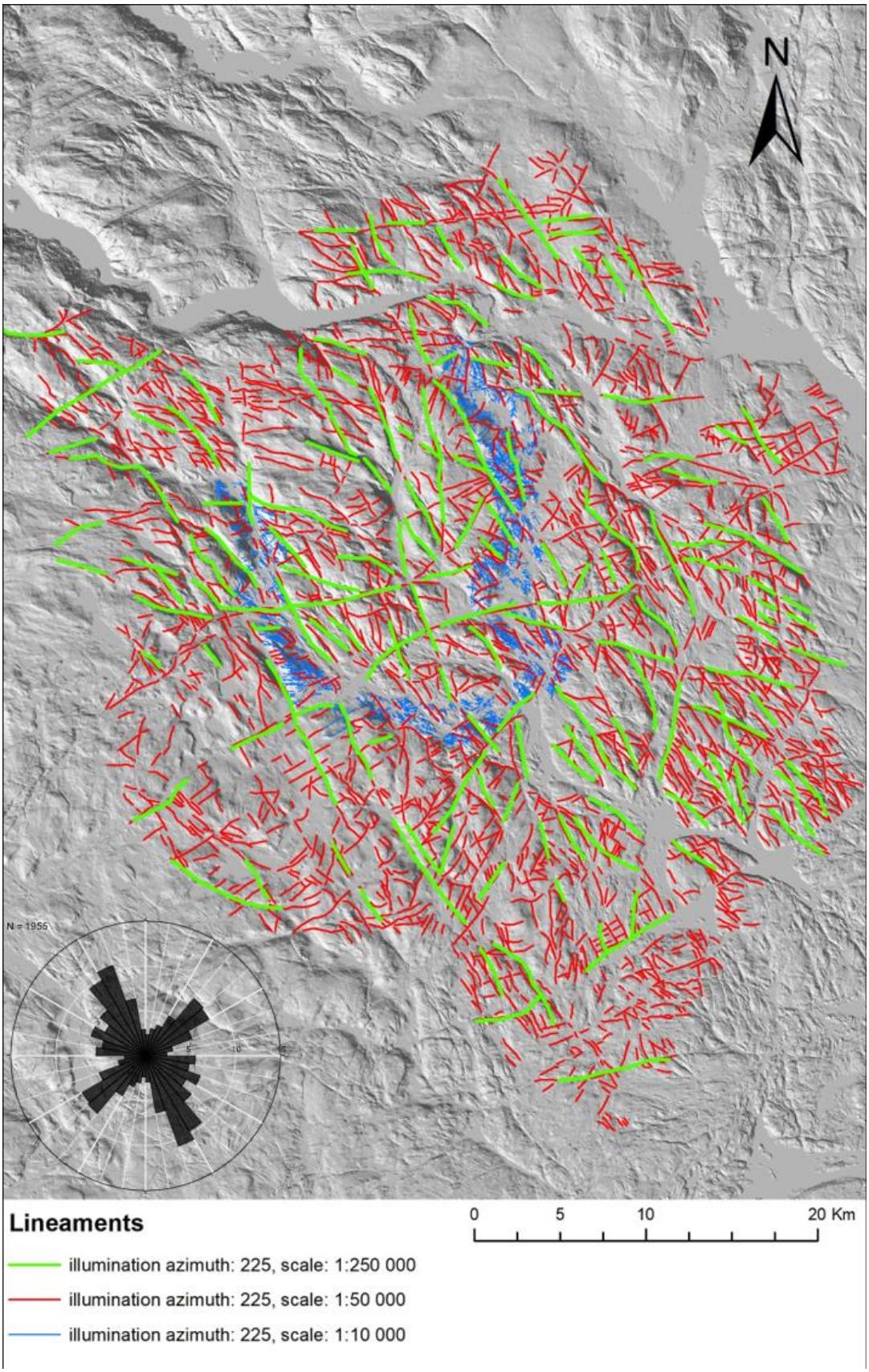

Figure 11. Topographic lineaments identified in the lineament study (Hilde Gunleiksrud, 2017). Hillshade illumination from 225° at three interpretation scales; 1:250 000, 1:50 000 and 1:10 000. The lineament orientations are presented in the rose diagram.

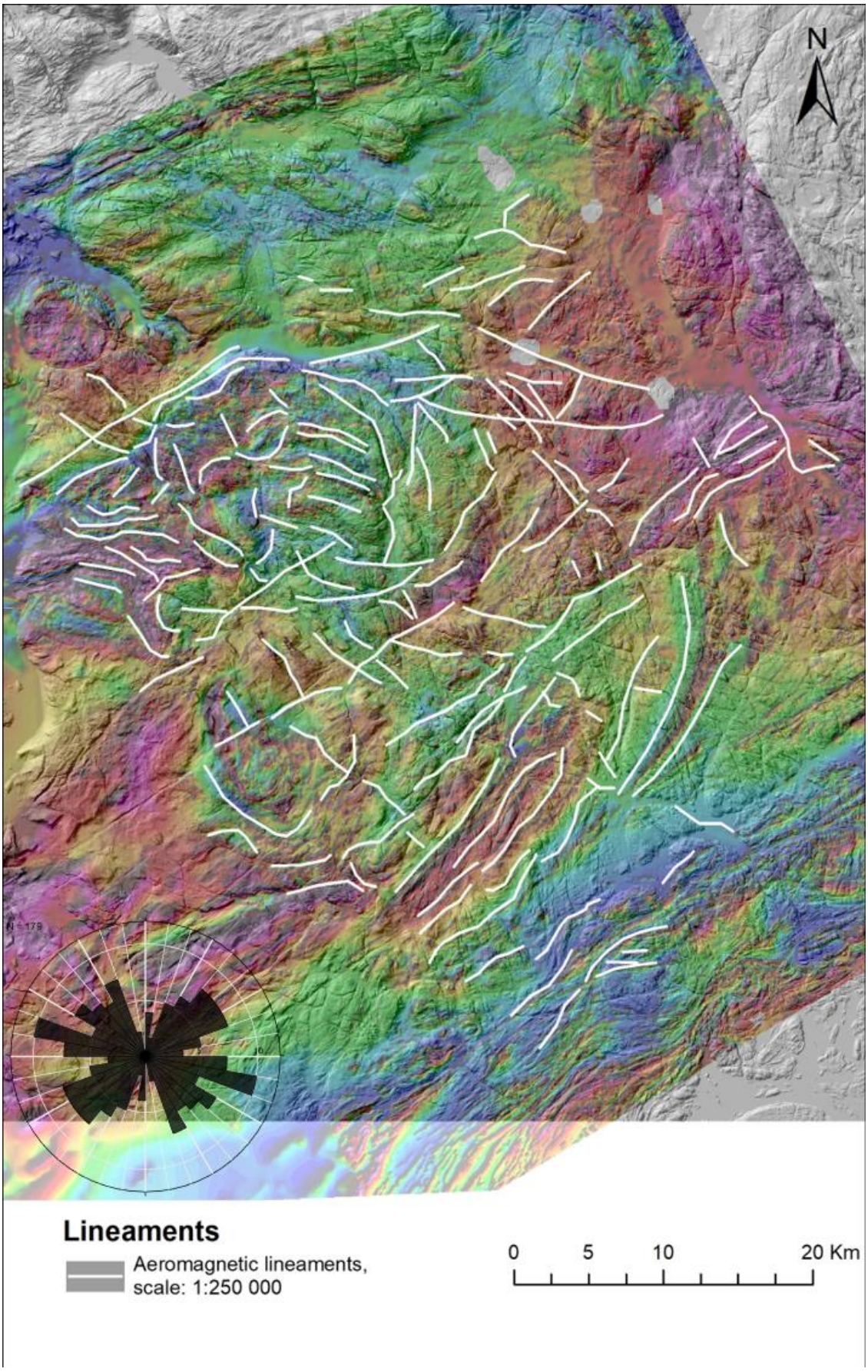

Figure 12. Magnetic lineaments identified in the lineament study (Hilde Gunleiksrud, 2017). The lineament orientations are presented in the rose diagram. Interpretation scale: 1:250 000.

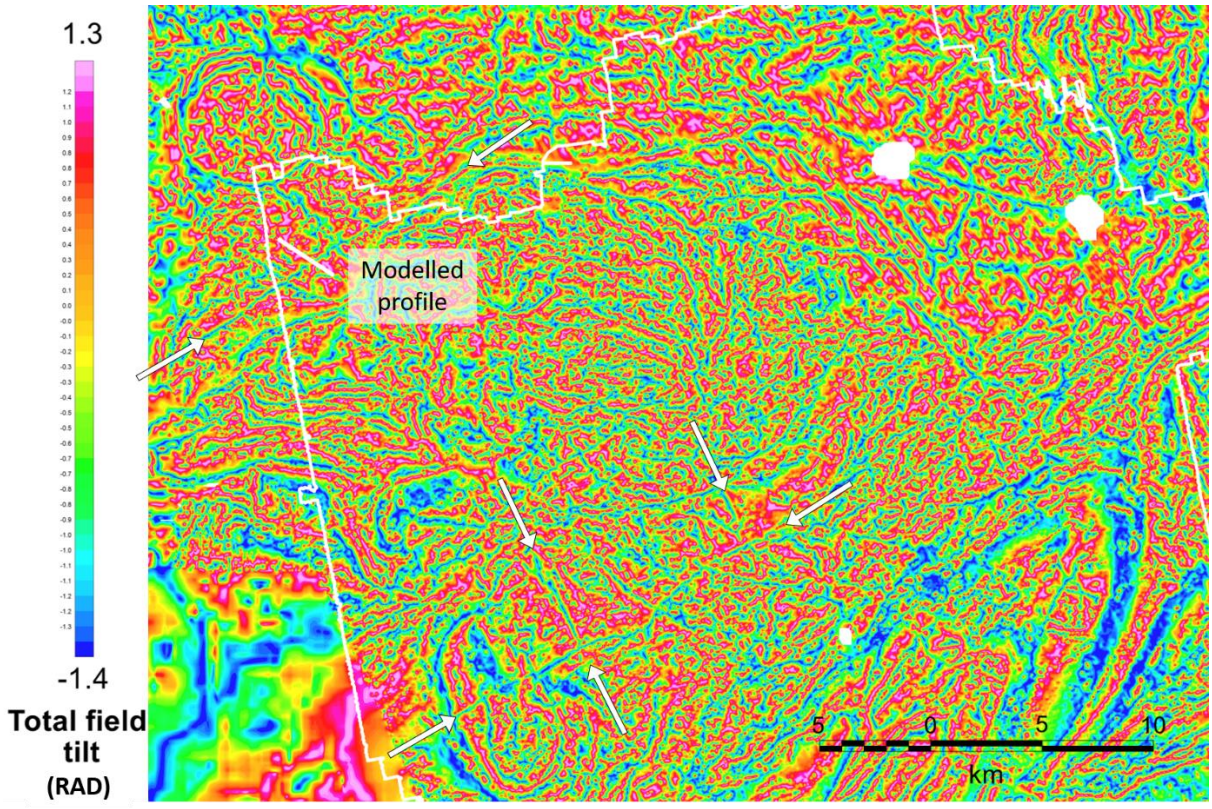

Figure 13. Tilt derivative filtered aeromagnetic data showing magnetic lineaments with anomalous signatures associated to brittle structures. The white outline shows the studied area. The modelled profile is described further in section 4.5.

4.2 General field-observations

The terrain and geomorphology of the Drangedal and Nome area is greatly influenced by the extensively fractured Precambrian basement (Figure 14). With a sparse sediment coverage, these features are well represented in both the remote sensing dataset and field observations. A system of valleys running NW–SE and NE–SW form major landforms in the area. Large lakes and rivers follow depressions in the terrain and generally comprise a NW–SE orientation. On the outcrop scale, the studied rocks are generally highly fractured. Fault planes are often moderately to intensely striated with slickensides or other types of lineation. Three main lithologies comprise the field area; *granitic gneiss*, *amphibolite*, and *granite* (Figure 14). The granitic gneiss is part of the *Vråvatn complex*, whereas the amphibolite forms part of the *Nissedal supracrustal complex*. Together, these make up most of the outcrops that were investigated in this study. At numerous localities, the amphibolite is observed as inclusions (or possibly as metabasaltic intrusions) in the granitic gneiss. The *Tørdal granite* intrudes the Vråvatn- and Nissedal supracrustal complexes and is somewhat less represented within the area of study (Figure 14).

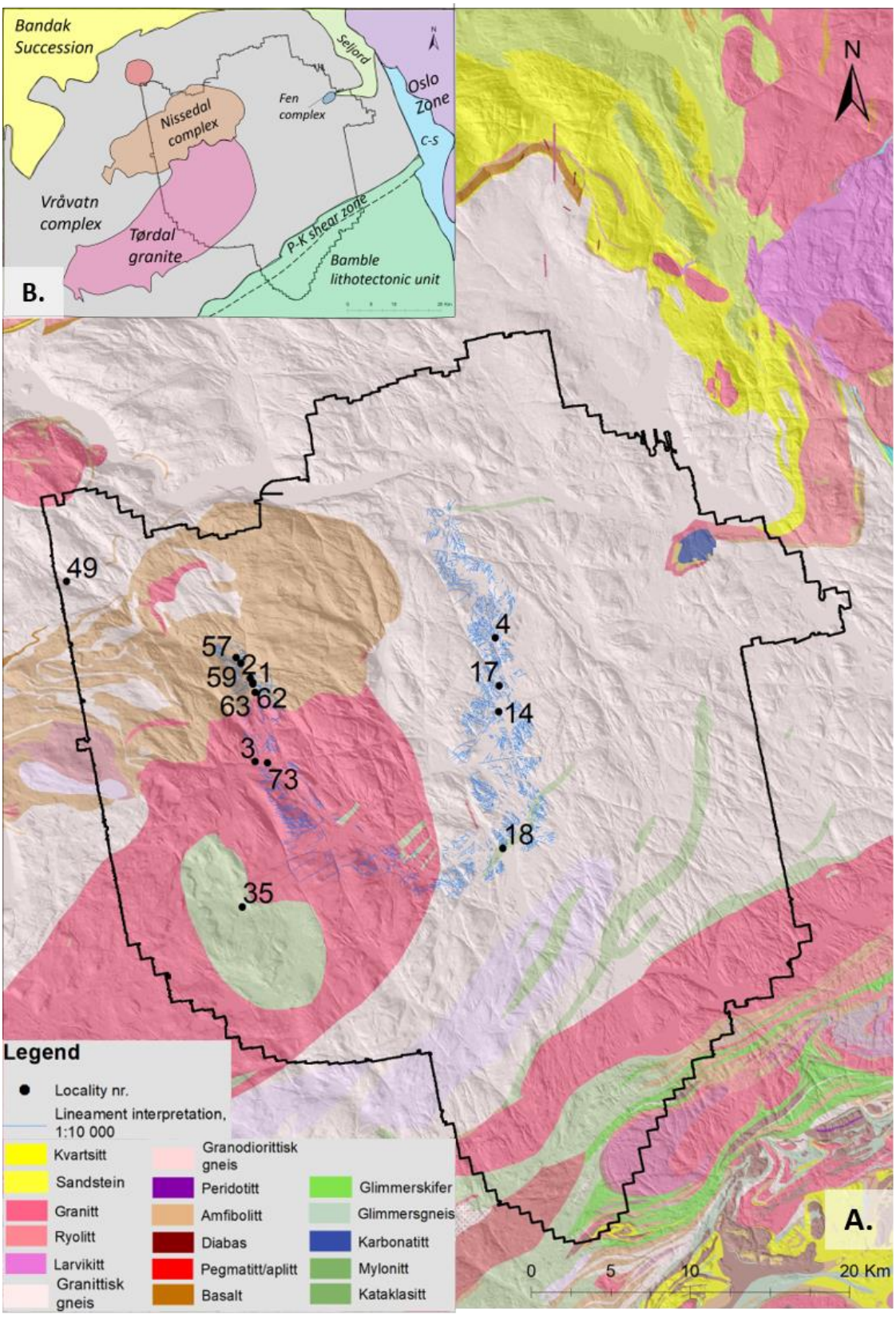

Figure 14

Figure 14. A.) Combined bedrock-map (NGU, 2018) and 10 m DTM of study area. 1:10 000 lineament interpretation and fourteen key localities are shown on the map. B.) Overview of lithological complexes, successions and lithotectonic units of significance in this study. Seljord = Seljord Sucession. P-K shear zone = Porsgrunn-Kristiansand shear zone. C-S = Cambro – Silurian lithologies of the Oslo Zone.

The *granitic gneiss* of the Vråvatn complex is generally characterised by a greyish pink, leuko- to mesocratic appearance, medium grained texture, strong banding, variably foliated and with frequent pegmatitic intrusions (Figure 15). The banding and foliation have near horizontal orientations and generally coincide well. Fault planes within the gneisses vary in both orientation and slip character as illustrated in the stereo- and rose diagrams in Figure 15. Despite the variation in strike, most planes are characterised by a steep dip. Mineralizations along the fault planes vary from light coloured quartz or calcite to polished, darker green/brown/black cataclasite and chlorite. Several fault planes with tectonically striated and grooved surfaces are also observed.

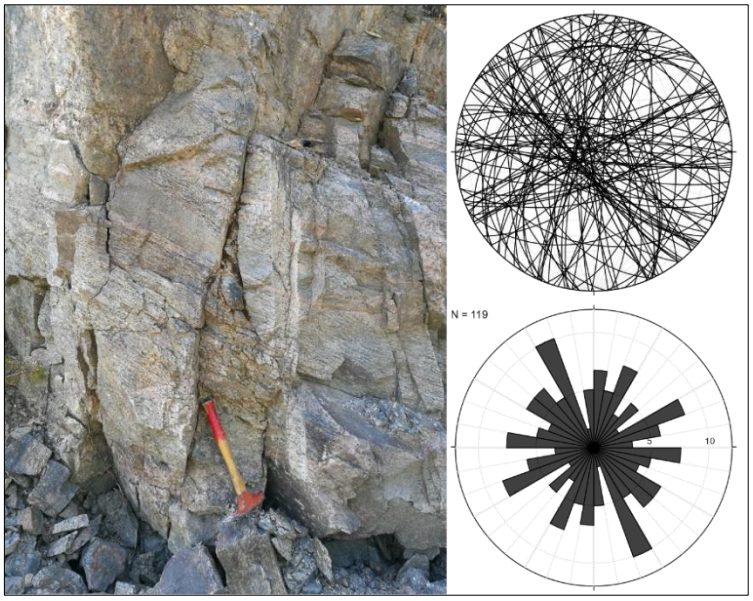

Figure 15. Vråvatn complex. Left: an example of a granitic outcrop displaying fracturing, banding and foliation. Right: stereo- and rose diagrams constructed from all fault plane measurements of granitic gneisses in the study.

The *amphibolites* of the Nissedal supracrustals are black-coloured, fine-grained and usually highly fractured and strongly foliated. Compared to the fault planes in the granitic gneiss, the fault planes in the amphibolite generally have a more consistent strike orientation of NE–SW to E–W (rose diagram in Figure 16). A less dominant set of planes striking NW–SE is also observed (rose diagram in Figure 16). The fault and fracture plane orientations appear to be highly controlled by the foliation, which comprises a similar NE–SW orientation (Figure 16). The kinematics indicated by slip-lines and lineations on the fault planes in the amphibolites are dominantly strike- to oblique-slip, with some influence of dip-slip. Fault plane surfaces are generally highly polished in a blackish green and brown coating of cataclastic or chloritic composition. Tectonically striated or grooved surfaces are, however, also well represented within the amphibolites. A few plane surfaces with light coloured mineralization (quartz or calcite) are also observed.

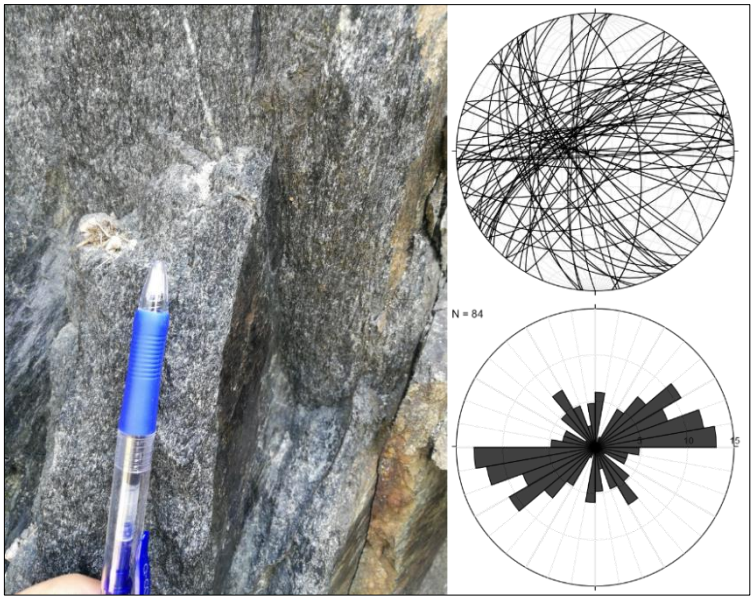

Figure 16. Nissedal Supracrustals. Left: an example of an amphibolitic outcrop displaying a set of steep, polished fault planes parallel to the foliation. Right: stereo- and rose diagrams constructed from all fault plane measurements of amphibolites in the study. area.

The *granite* (Tørdal granite) is characterized by a light pinkish grey colour and a fine to medium grain size (Figure 17). Being significantly more massive and homogenous than the other two lithologies, it is reasonable to assume that the granite has deformed in a more mechanically isotropic manner and that the deformational structures are oriented more optimally in terms of the stress field. Generally, there are significantly fewer brittle structural features in the granites relative to what was observed in the amphibolites and granitic gneisses. The fractures and fault planes observed comprise a very consistent orientation, with NE–SW-strike dominating. A less dominant set of planes striking NW–SE was also registered (rose diagram in Figure 17). Generally, the fault planes are mineralized by chlorite and exhibited lineations indicating dip-slip to oblique-slip kinematics. In contrast to the frequently polished fault planes of the amphibolites and granitic gneisses, the fault plane surfaces in the granite were of a considerably rougher character.

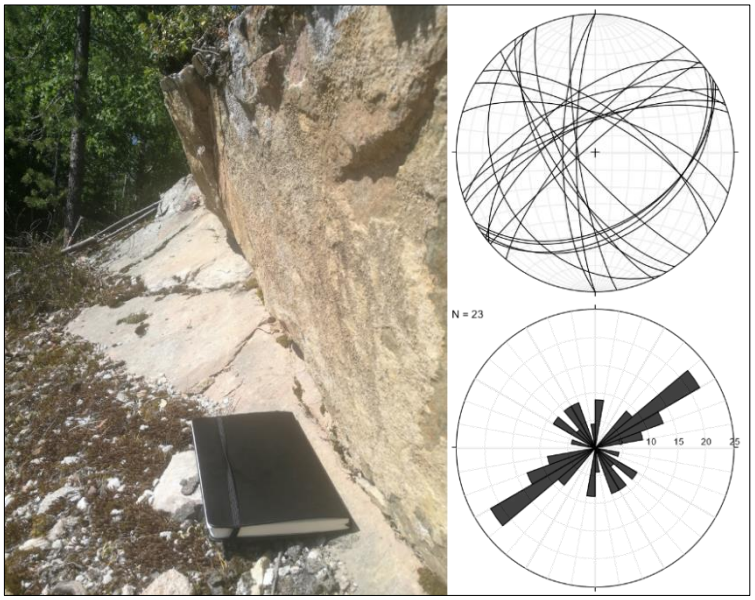

Figure 17. The Tørdal Granite. Left: an example of a granitic outcrop. Right: stereo- and rose diagrams constructed from all fault plane measurements of granites in the study area.

4.3 Key Localities

Well documented localities presenting important structural data, such as kinematic indicators, were selected as *key localities*. Fourteen key localities (Figure 14) were selected from various lithological domains, geographic locations and with varying feature characteristics in order to represent the entire Drangedal and Nome area. Figure 18 compares the fault plane measurements of the fourteen key localities (B) to fault plane measurements of the entire field dataset (A). The dominant NE–SW and NW–SE faults are represented in both datasets. Although less prominent than the NE–SW and NW–SE faults, a NNE–SSW fault population is represented in the measurements of the entire data-base (A). A few NNE–SSW faults are represented in the key localities (B), but are not very well represented. This is primarily due to the lack of kinematic indicators along these faults, which is a key requirement for structural analysis and paleo-stress inversion (Figure 18C)

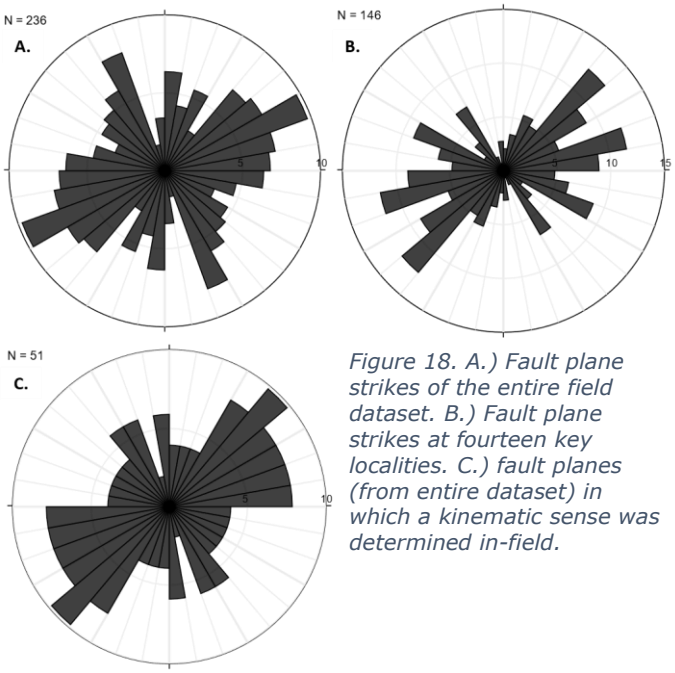

Figure 18. A.) Fault plane strikes of the entire field dataset. B.) Fault plane strikes at fourteen key localities. C.) fault planes (from entire dataset) in which a kinematic sense was determined in-field.

Detailed descriptions of six key localities are presented below along with microstructural observations and mineralogic analysis by SEM and optical microscopy.

4.3.1 Locality 1

Locality 1 (Figure 14) is located along Rv. 38 between Bø and Grova. It is dominated by mesocratic, grey, fine grained and highly foliated amphibolites of the Nissedal supracrustal complex. At this locality, a series of sub-vertical NE–SW-striking fault and fracture planes are developed (sub-)parallel to the foliation (Figure 19). The fault and fracture planes are straight and closely spaced, with a highly polished surface. No fault rock of significant thickness is observed, and all deformation seems to be accommodated along multiple discrete slip planes. Well-developed, flat-lying slickenside lineation in a brownish-green chlorite coating is found on many of the fault planes (Figure 19A-B). Vague steps in the slickensides indicate dextral movement (Figure 19) along these fault planes. An oriented thin section sample from this locality is analysed to further assess the kinematics. Riedel fractures, grain drag along fractures, and releasing bends (Figure 20) are all consistent with the dextral kinematics derived from field-observations.

Figure 21A shows incredible details of the fault plane surface imaged by Secondary Electron (SE). At this scale, the lineations resemble coarser striation grooves, but are still of a very linear character. Mineralization on the corresponding area of the fault plane is imaged by Backscatter Diffraction (BSD) scanning in Figure 21B. EDS analysis shows that it is composed of amphibole, pyroxene and cataclastic material of mixed mineral. The odd occurrence of zircons is also identified in the fault plane. Analysing the two images (Figure 21A–B) together, it appears that the light and grey linear domains correspond to striations scraped into the amphibolitic host rock, wherein cataclastic material appears to fill in depressions in the fault plane.

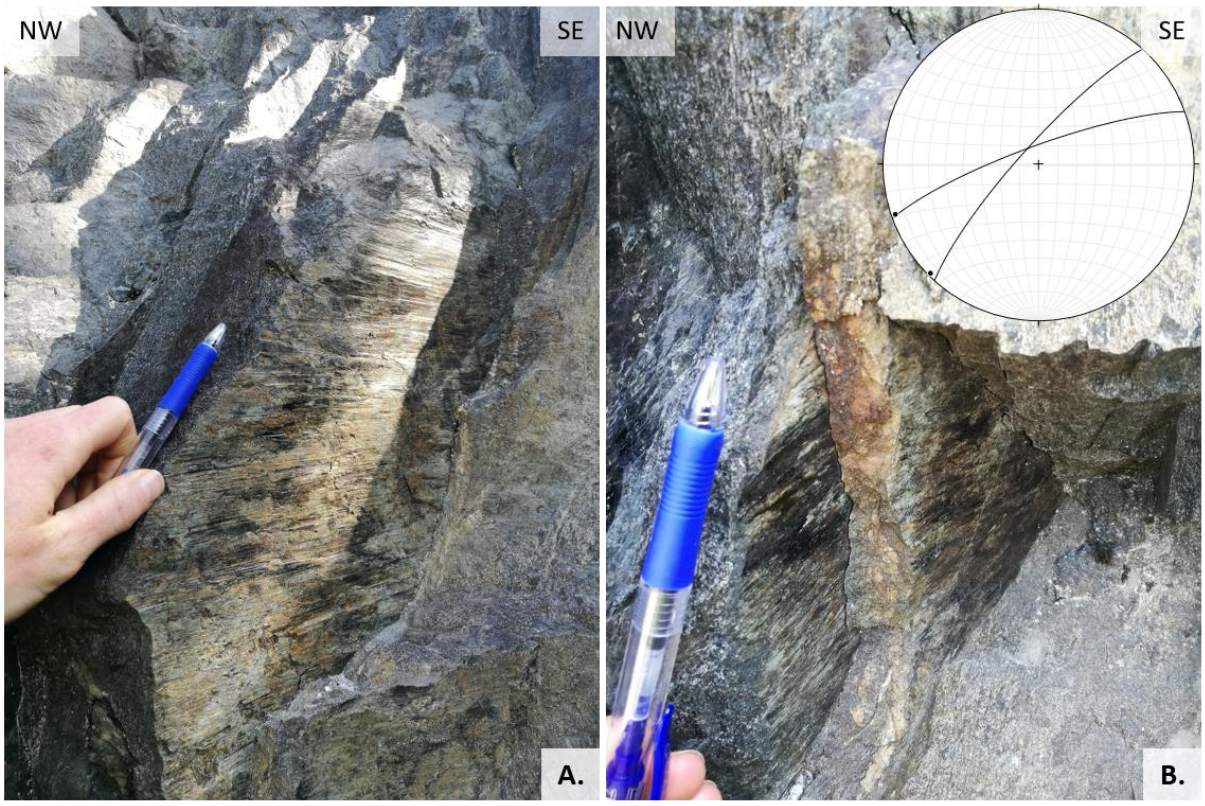

Figure 19. Locality 1. A. and B. show the amphibolite with a series of fault planes covered in slickenside lineations (slip-lines). These fault planes and associated slip-lines are plotted in the stereonet.

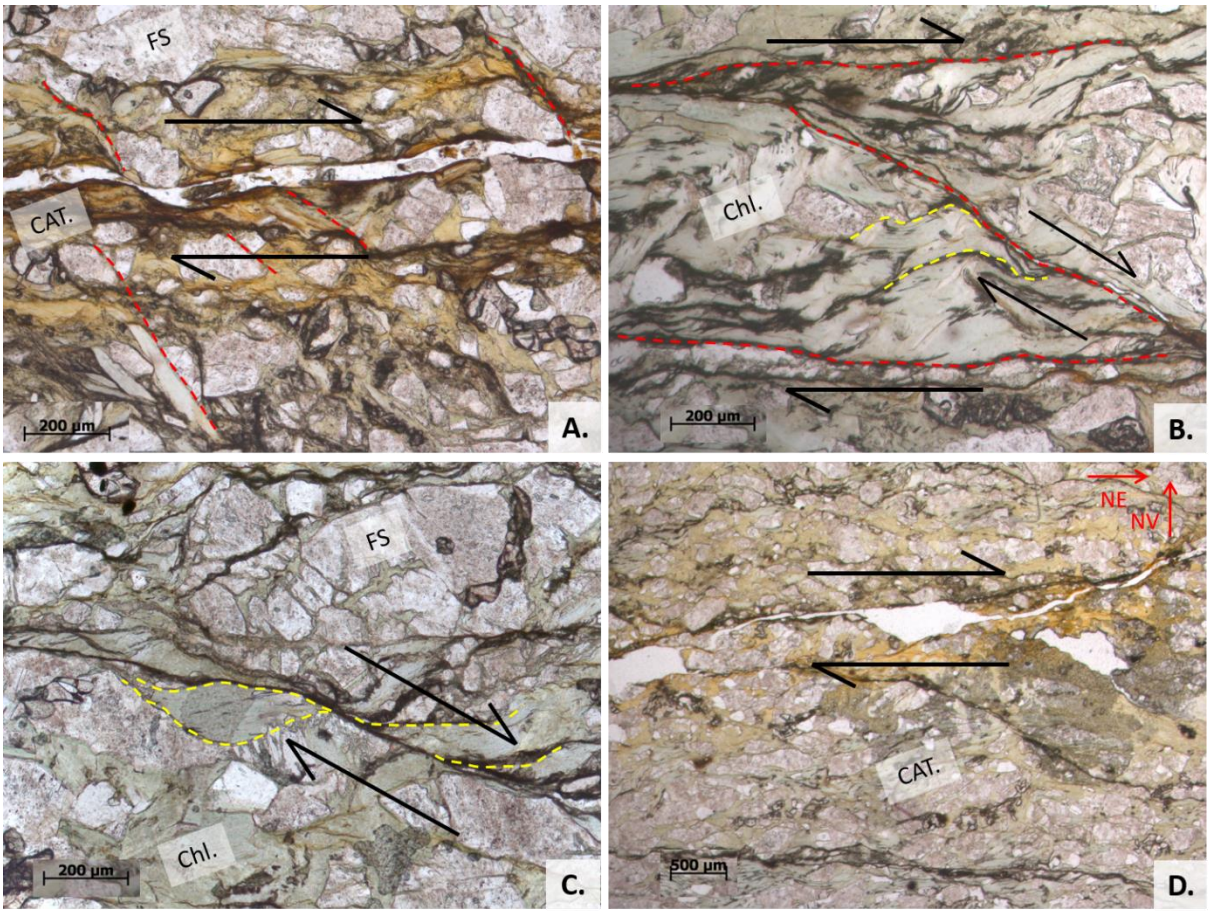

Figure 20. Thin section images of Sample 501 from locality 1. A. and B.) Riedel fractures running out from fault-parallel fracture planes shown. C.) Grain-drag along fault-parallel fracture planes. D.) Releasing bends in fault-parallel fracture planes. All structures indicate a dextral kinematic. Chl.: chlorite, CAT.: cataclasite, FS: feldspar. Orientation in D. also applies to A., B. and C.

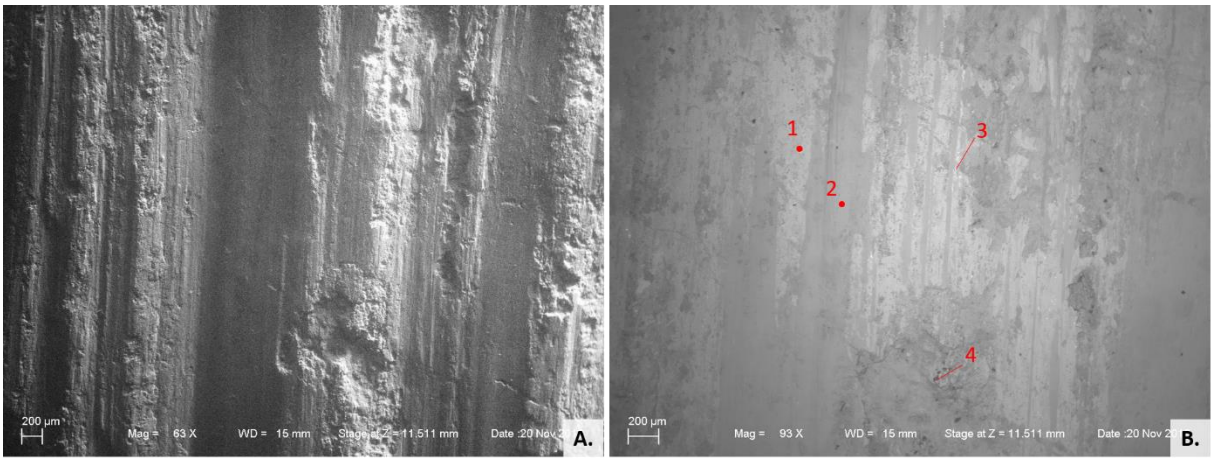

Figure 21. SEM images of Sample 501 showing the fault plane surface. A.) Secondary Electron (SE) imaging showing details of the well-developed fault plane lineation. B.) Backscatter Diffraction (BSD) imaging with mineralization interpretation as follows; 1: amphibole, 2: pyroxene, 3: zirconium, 4: cataclasite. Amphibole dominates the light domains, pyroxene the grey domains and cataclasite the dark domains. A. and B. show the same area of the sample.

4.3.2 Locality 3

Locality 3 (Figure 14), a fresh roadcut close to Bø, displays rocks and structural features nearly unaffected by surface weathering. The outcrop is composed of a leucocratic, light pink, even- and medium-grained granite (Tørdal granite) and is significantly more massive and homogenous compared to the other lithologies in the study area.

Both fault- and fracture planes are identified at the outcrop. The two sets of planes differ in both character and orientation. Fault planes have slickenside lineations in a mineralization of chlorite (and some pyrite) (Figure 22B–C). Measurements of these lineations indicate a dip-slip sense of movement and the presence of small steps in the mineral coating indicate normal kinematic. The fault planes dip moderately (c. 45°) towards the SE (Figure 22D). The fractures trend parallel to the fault planes, but dip much steeper (sub-vertical) (Figure 22A–B,D). A syntaxial growth of a light-coloured mineral (calcite) on the fracture planes, indicate tensile strain (Figure 22A). However, the distinction between a tensile fracture and a hybrid fracture can be a challenge – especially when based on field observations of direction of mineral growth. An influence of small components of shear in this fracturing can therefore not be ruled out. In any case, the geometrical association of steep tensile fractures is consistent with normal dip-slip movement along the fault planes (Figure 22).

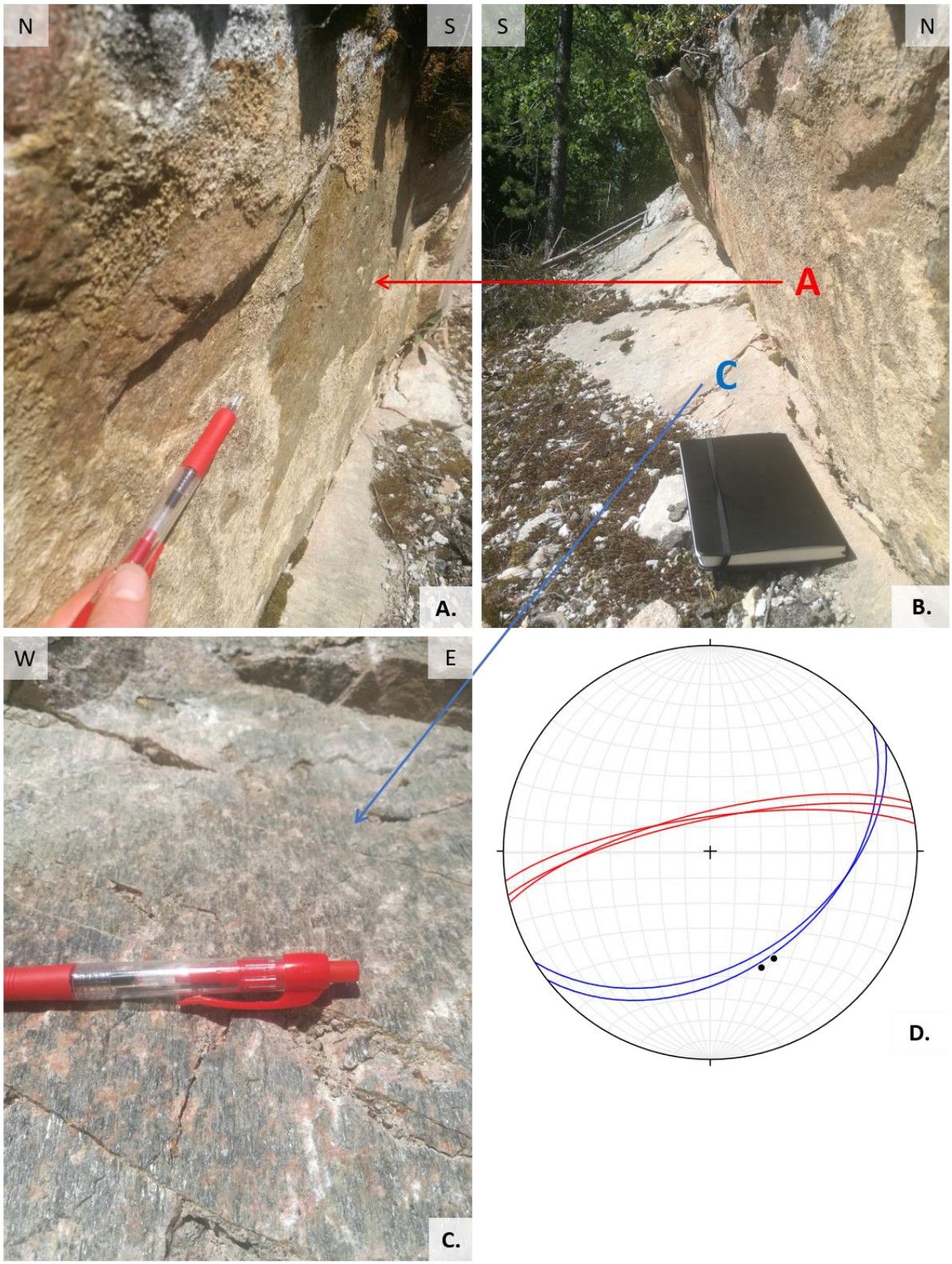

Figure 22. Granitic outcrop at locality 3. C) Fault plane with associated slickenside lineations and plotted as blue lines with black points in stereo net. A) Fracture plane with light mineralization and plotted as red lines in stereo net.

4.3.3 Locality 4

East in the study area (Figure 14), along the east side of Fv. 109, is a large roadcut of approximately 100 m (Figure 23). outcropping a leucocratic, light pink to grey granitic gneiss with grain size varying from medium- to coarse-grained. Banded structures and pegmatitic intrusions make the rock-mass highly heterogenous. Based on these observations the rock is identified as a granitic gneiss of the Vråvatn complex.

Figure 23. Overview of locality 4 displaying a highly fractured and banded granitic gneiss with two major sets of fault and fracture planes. Blue arrows show NE–SW striking fault planes of sub-set 4,1. NW–SE striking faults of sub-set 4,0 run parallel to the road and are therefore not as visible in this photo. Photo by Torgersen. Bingen for scale.

Two main structural groups are identified at this outcrop. One group consists of a set of steep, undulating planes with a SW dip (sub-set 4,0, Figure 24A–B,D). The other group consists of a set of slightly less steep, undulating planes, generally with a NW dip (subset 4,1, Figure 24C–D). Similar plane surface characteristics were observed in the two sets. The light coloured fault plane mineralization was identified to be mainly quartz and calcite (Figure 25) based on a combination of field-observations (visual and application of acid), thin section microscopy (Figure 25) and scanning electron microscopy. Slickenside lineations in this mineralized surface indicate dip-slip movement along both fault sets (Figure 24B–C). In some isolated areas, steps in the slickensides suggest normal kinematics. Moreover, the steep dip of the planes is also characteristic of extensional (dip-slip) regimes. Several fault cores of unconsolidated (breccia and fault gouge) material are observed throughout the outcrop. The fault cores are 3–15 cm thick and vary in colour between red/pink and greenish grey (Figure 24B). The majority of faults of this character were recorded in sub-set 4,1.

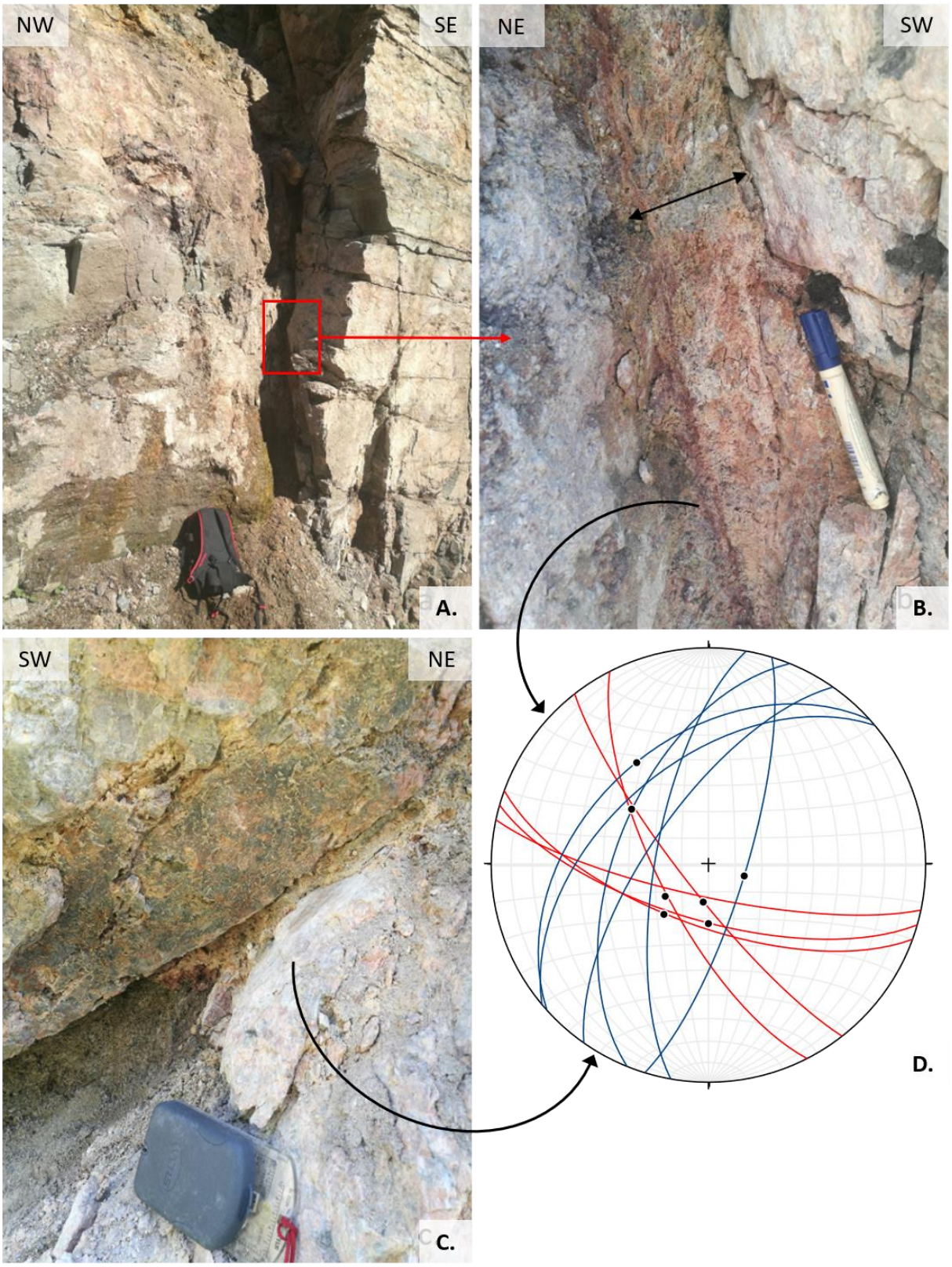

Figure 24. Fault architecture at locality 4. A). Fault planes with a lineation in a light-coloured mineralization of sub-set 4,0. B.) Brecciated/unconsolidated fault rock of sub-set 4,0. C.) Fault planes of sub-set 4,1. and plotted with red lines in D. and with blue lines in D. Lineations in a light mineralization are observed on the fault planes in B. (hanging wall on right side) and C. (footwall).

A thin section sample (515) was collected from locality 4 for further kinematic and mineralogic analysis to accompany the in-field interpretations. The thin section in Figure

25 is a cross section of a fault plane of sub-set 4,0. A calcitic mineralization is identified along the surface of the fault plane, corresponding well with the field observations. Further investigation of the boundary between the mineralized surface and the wall rock, reveals fractures occurring regularly out from the boundary at an angle of approximately 30° (Figure 25B). These fractures are interpreted as Riedel fractures and indicate a reverse kinematic. Along the boundary of fault plane mineralization and the wall rock, grain drag of a chloritic grain is also consistent with a reverse kinematic (Figure 25C). A reverse kinematic contradicts the in-field interpretations and is also a surprising result considering the steepness of the plane (c. 80°). Reverse movement is rarely accommodated in faults with a dip greater than 45°. Even in a situation of reactivation, reverse faulting rarely occurs along planes with a dip of 80° (Sibson & Howard Poulsen, 1988). The possibility that the sample is wrongly oriented or that this sample is not representative for the fault-plane in large, needs to be considered. Normal kinematics, as observed in the field, is applied for further use in the study.

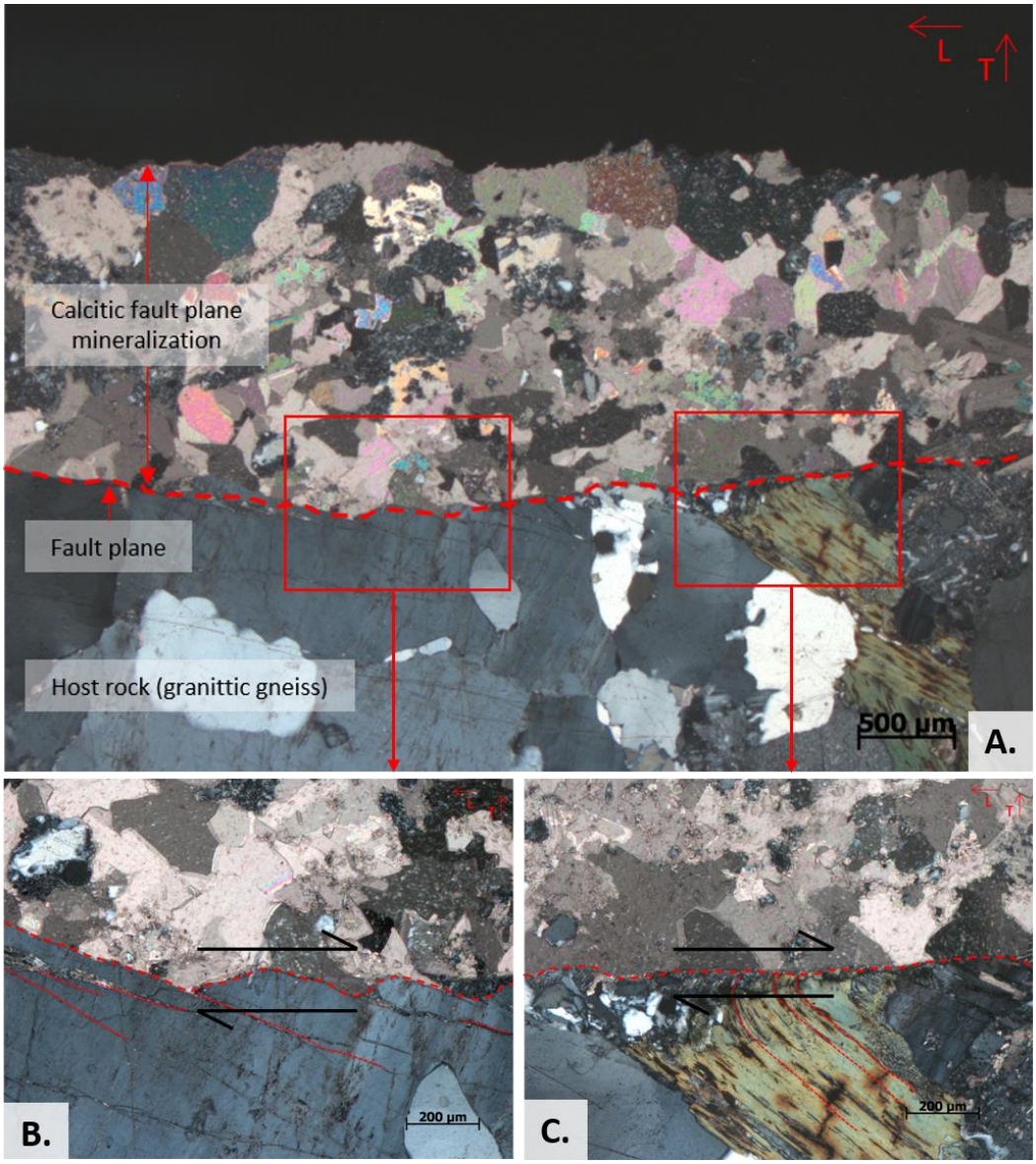

Figure 25. Thin section analysis of sample 515. A.) Overview of the micro-structures analysed. The (thick) dashed red line illustrates the boundary between the calcitic fault-plane mineralization and the wall rock. B.) Dextral grain-drag of a chloritic grain. C.) Riedel fractures of dextral character occurring at an angle from the boundary between the wall rock and the mineralized fault plane. Note that dextral kinematics in microscope view correspond to reverse in-situ kinematics. The orientation of the sample is given by red arrows indicating the direction of lineation (L) and top (T).

Electron microscope investigations of the fault plane surface representative of sub-set 4,0 show the well-developed slickenside surface of the fault plane (Figure 26). Based on analysis of the BSD image and corresponding elemental composition, quartz appears to dominate the fault plane mineralization. Contradictory to field and thin section observations, no calcite was identified in this specific sample, indicating local and isolated domains of calcite and quartz mineralization. Some small, light specs (on the BSD image) of a rare elemental assemblage may correspond to allanite.

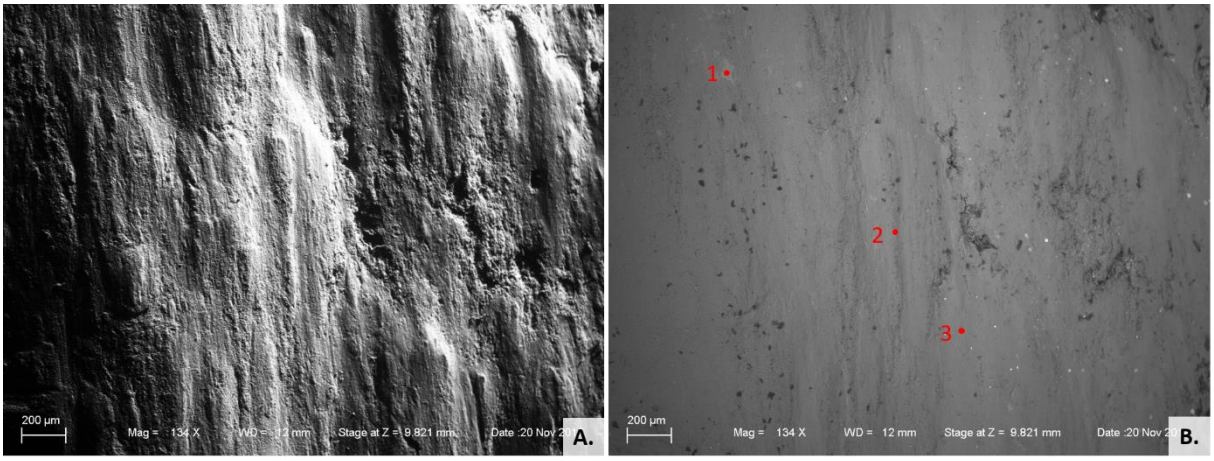

Figure 26. SEM images of Sample 502 showing the fault plane surface of sub-set 4,0. Both represent identical domains of the sample. A.) Secondary Electron (SE) imaging shows details of the well-developed fault plane lineation. B.) Backscatter Diffraction (BSD) imaging to investigated elemental composition. Points 1., 2., and 3. all indicate a quarzitic mineralization.

4.3.4 Locality 14

A roadcut on the west side of Fv. 109 exposes a c. 50 m long outcrop varying from leuco- to mesocratic and light pinkish grey to a darker grey rock (Figure 27). The rock exhibits a well-developed foliation and banding, making it highly anisotropic with varied structural features. Based on the observations, the rock is identified as a granitic or granodioritic gneiss of the Vråvatn complex.

Figure 27. Central part of outcrop at locality 14, displaying a banded and foliated granitic gneiss.

Sub-vertical, undulating fault planes with a NE–SW strike are the dominant structural feature at this locality (Figure 28B). These planes are characterised by their highly polished surfaces and dark green to black coatings (likely a very thin ultracataclastic zone). Two sets of slickenside lineations are identified on these fault planes (Figure 28, Figure 29A). The dominant set is observed in the dark cataclastic surface and comprise a strike- to oblique sense of slip (sub-set 14,0). In a few areas, steps in the slickensides indicate a dextral kinematic. Another, more subtle set of lineations (sub-set 14,1) is observed in a lighter chloritic green mineral phase. These lineations were not as prevalent throughout the fault planes, as they appear to be overprinted by the more dominant sub-set 14,0. The orientation of these lineations differ from those of sub-set 14,1 and indicate dip-slip movement. Although no kinematic indicators associated to the dip-slip lineations are identified, the sub-vertical character of the fault plane makes it reasonable to assume normal kinematics.

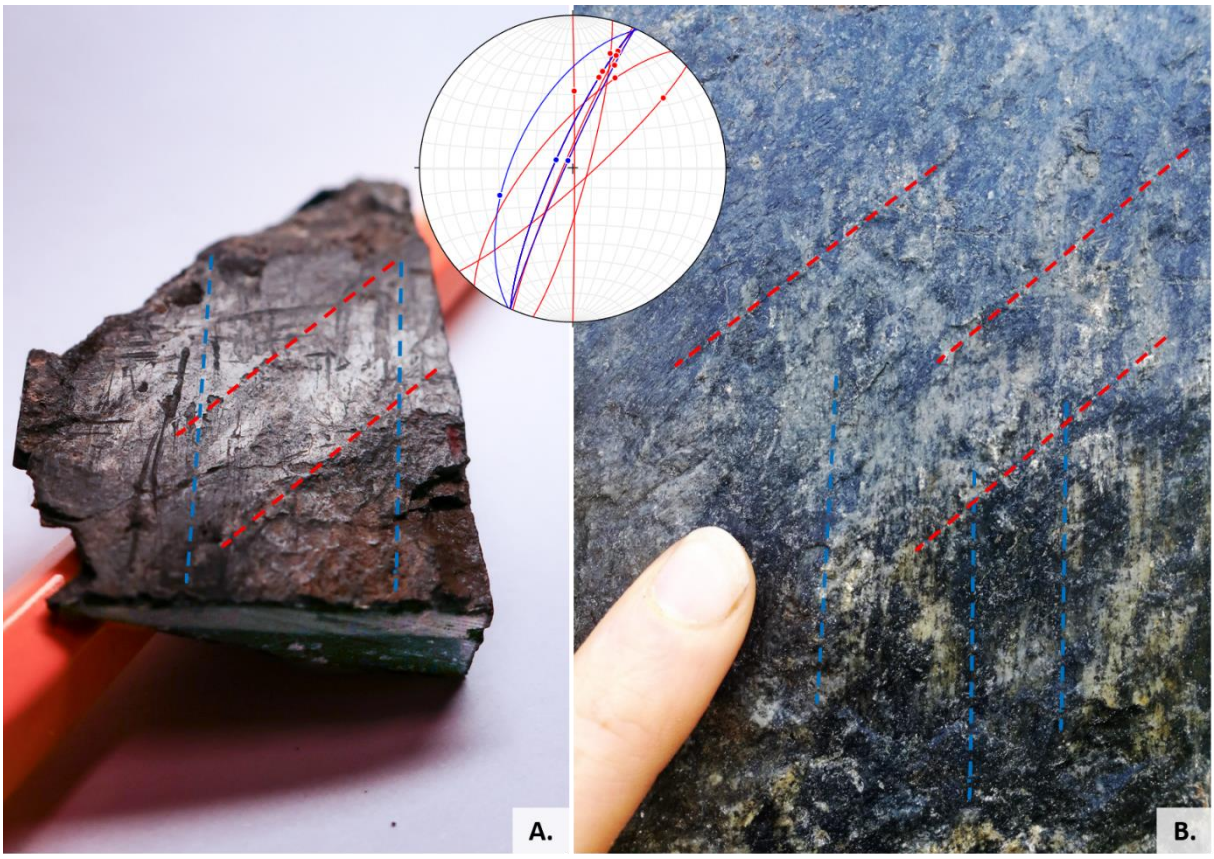

Figure 28. Fault plane surfaces with two sets of lineations at locality 14. A.) a sample (522) of the fault surface of the NE–SW striking fault plane. Sample 522 is also analysed by thin section microscopy (Figure 30) and SEM imaging (Figure 29). B.) Photo of the fault plane where sample 522 was acquired. Red dashed lines represent strike- to oblique-slip lineation of sub-set 14,0 and blue dashed lines represent dip-slip lineation of sub-set 14,1. Red great circles (stereonet) represent sub-set 14,0 and blue great circles (stereonet) represent sub-set 14,1.

The presence of two lineations are further investigated by SEM (Figure 29). The SE image shows a coarser set of lineations (blue dashed lines) crossed at an angle of a fainter, finer lineation (red dashed lines) (Figure 29A). As the sample was placed in the microscope, attention was paid to the orientation in terms of lineation-direction. It is therefore known that the coarser lineation corresponds to the light green lineation of sub-set 14,1 and the finer lineation corresponds to the polished, more prevalent lineation (according to field observations) of sub-set 14,0. Although it might be expected that sub-set 14,0 lineations should also be more prevalent in the SEM imaging, their polished character is not visualized as clearly by SEM imaging. Based on analysis of the BSD image (Figure 29B) and computed elemental composition from EDS-analysis, chloritic minerals appear to dominate the fault plane. In addition to the main constituents of chlorite; Mg, Al, Si, Fe, O, many of the analysed points contain a chaotic variety of other elements - indicative of cataclasite. Thus, it appears that the fault plane is mineralized with a combination of chlorite and cataclasite. However, due to the thin and often faint lineations, it is difficult to properly isolate and distinguish these two mineralizations.

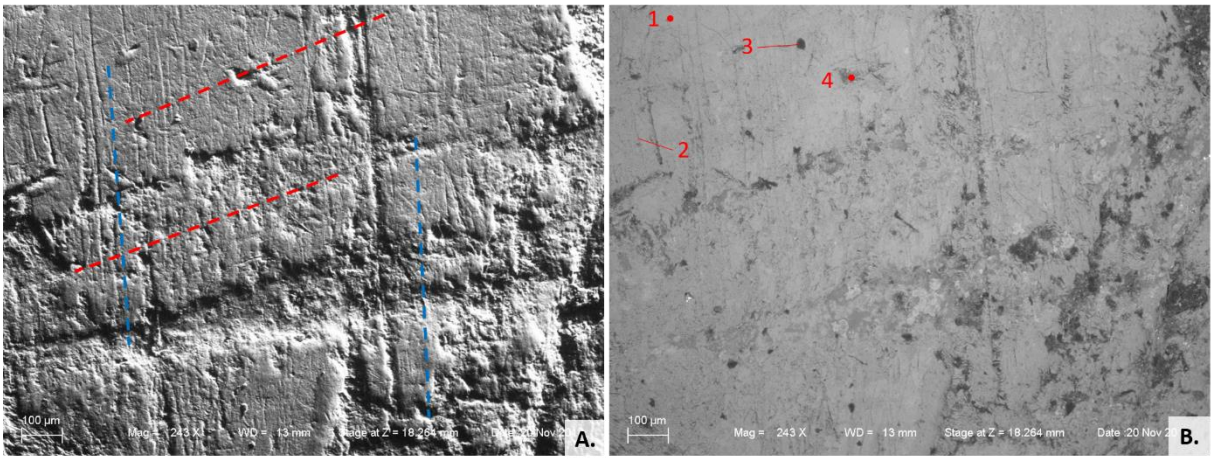

Figure 29. SEM images of Sample 522 showing the fault plane surface of with two sets of lineations (corresponding to Figure 28). Both images represent identical domains of the sample. A.) Secondary Electron (SE) imaging showing incredible details of the well-developed fault plane lineations, with sub-set 14,0 represented by the red dashed lines and sub-set 14,1 represented by the blue dashed lines. B.) Backscatter Diffraction (BSD) imaging shows points in which elemental composition was investigated and indicates a dominance of chloritic and cataclastic mineralization. 1., 2., 4.: chlorite, 3.: chlorite/cataclasite.

A thin section (522B) of the fault plane surface shows the complexity and chaotic nature of the rock fabric in these faults (Figure 30). Although it was not possible to determine any kinematics, mineralogic analysis demonstrates that chlorite and cataclasite are the prevalent mineral phases just below the fault surface, which correspond well with observations in the SEM imaging and field observations. A sharp boundary between a chloritic and cataclastic domain is interpreted to reflect two individual phases of deformation. This correlates well with the two distinct senses of slip indicated by sub-set 14,0 and 14,1 in the field.

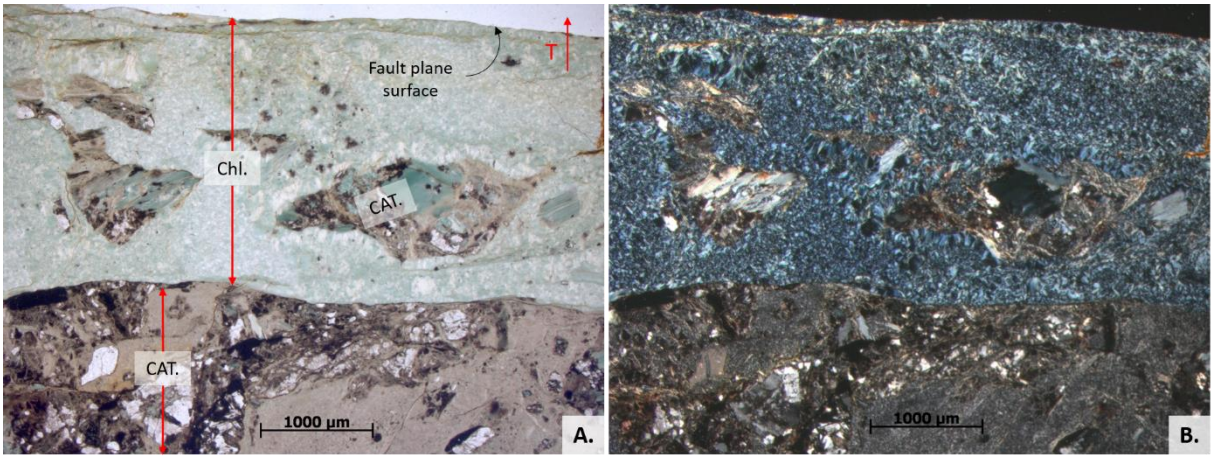

Figure 30. Thin section sample 522B imaged in plane polarized light (A.) and cross polarized light (B.). Both are taken from the same domain of the thin section, so labels in A. apply for B. as well. The images represent the domain just beneath the fault plane, showing a chloritic (Chl.) and a cataclastic (CAT.) domain, separated by a clear boundary. Fragments of cataclasite are included in the chloritic domain. T indicates top (up).

Another structure of significance at this locality is a c. 2 m wide cataclasite varying in character from procataclastic to ultracataclastic. Slickenside lineations are observed in the plane defining the margin of the cataclastic zone, comprising a similar orientation and character to those of sub-set 14,0. Measurements associated to the cataclasite are therefore included in sub-set 14,0 (plotted as red great circles in Figure 28). Thin section sample 515 was taken from the margin of the cataclastic zone for further kinematic

analysis. Figure 31A–C illustrate *releasing bends* in fault-parallel fractures that indicate a dextral kinematic. Figure 31D illustrates an example of grains that have been *fractured and displaced* in a dextral sense, also along fault-parallel fractures. Thin section observations of dextral kinematic corresponds well to the overall field observations of sub-set 14,0.

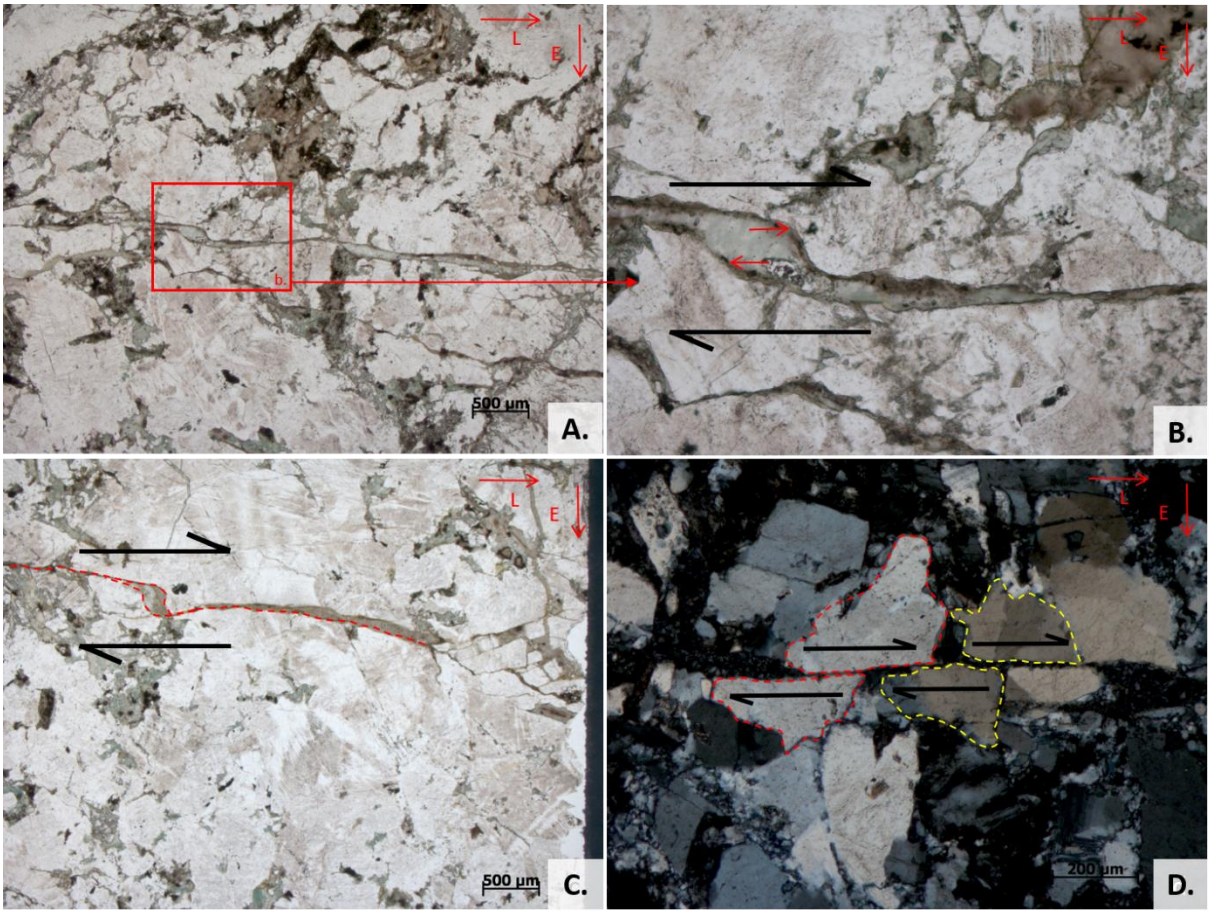

Figure 31. Micro-structures of thin section 515 taken from margin of cataclasite (sub-set 14,0). A.-C.) Releasing bends in fault-parallel fractures all indicate a dextral kinematic. D.) Fractured and displaced grains along a fault-parallel fracture – also indicating a dextral kinematic.

Several other steep planes, with rough surfaces and sporadic, light coloured mineralization are also identified (Figure 32). The orientation of these planes differs significantly from that of the fault planes (sub-sets 14,0 and 14,1) as shown by the dashed lines in Figure 28B. Near-syntaxial mineral growth indicates that these planes are fractures resulting from a tensile strain. One of the orientations measured in these fracture planes fits well into the system of strike-slip fault planes of sub-set 14,0, while the remaining fracture planes do not seem to fit into the other fault systems.

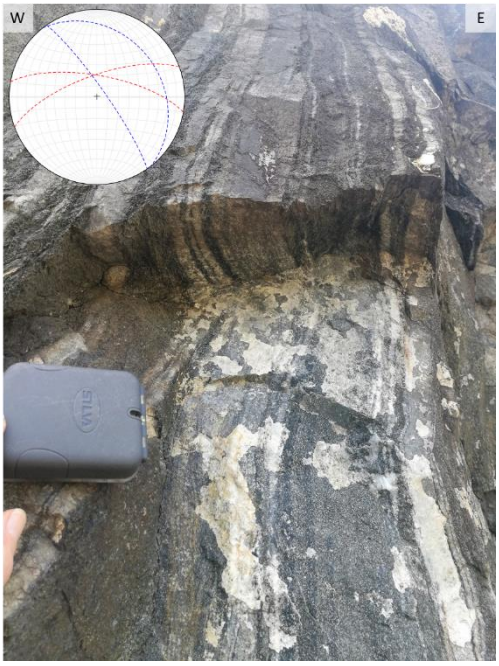

Figure 32. Fracture planes at locality 14 with a light sporadic mineralization. Two sets of fracture planes were measured and are represented by red and blue dashed lines in the stereonet.

4.3.5 Locality 17

Locality 17 (Figure 14), a roadcut on the east side of Fv. 109, displays rocks with similar character of locality 14, and is also determined as a granitic gneiss of the Vråvatn complex. This locality also exhibits a variety of structural features.

A distinct fault zone with a brecciated/weathered and partly eroded fault core of 50–100 cm runs though the roadcut, creating a cave-like structure separating the hanging wall from the foot wall (Figure 33A–B). The margins (fault plane) of the fault core are undulating, making it difficult to make a representative measurement. Generally, the plane has a moderate dip towards east, as illustrated by the orange line in Figure 34. No lineations or other structures for kinematic indication are identified. Within the fault zone, a great diversity of mineralizations and rock fragments are observed (Figure 33C). Massive crystals of pure calcite (5–10 cm), green, thin, needle-shaped mineral, quartz crystals and fragments of granitic gneiss (up to 10 cm) are all observed within a fine grained greenish-grey matrix. Substantial quartz crystallisation is observed on the fault plane of the weathered zone (Figure 33D). The crystal growth appears to be unconstrained and near perpendicular to the fault plane, indicating of a period of tensile strain at a shallow crustal depth.

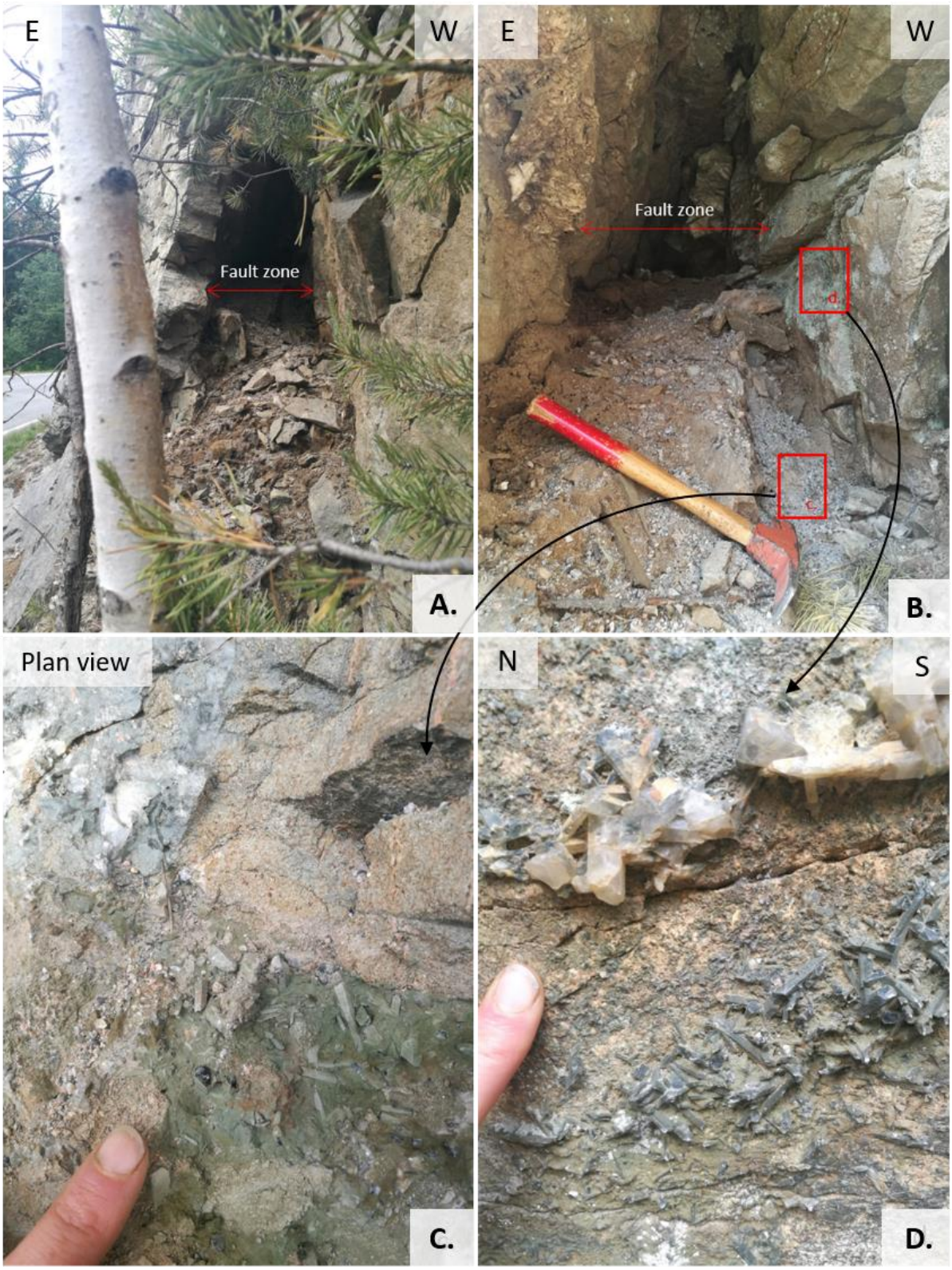

Figure 33. Fault at locality 17. A.-B.) Weathered/brecciated fault core of 50-100 cm giving a cave-like structure. Photo B. is taken inside the "cave", and photo A. is taken from a distance. C.) Assemblage of variable mineralogy, grains and clasts within the brecciated fault core. D.) Mineral growth on the fault plane surface defining the margin of the fault core.

Along both sides of the fault in Figure 33, planes striking NW–SE with a steep dip and lineations indicating oblique fault-slip are observed (sub-set 17,1, blue great circles in Figure 34). The fault surfaces vary from a light-coloured mineralization to tectonic striations and grooves. Vague kinematic indications representing dextral-normal-oblique movement are observed in one of the planes. A 10 cm thick cataclastic zone comprising a similar orientation as the fault planes of sub-set 17,1 is also observed. The plane defining the margin of the cataclastic zone is a highly polished surface with lineations indicating oblique-slip movement corresponding to the rest of sub-set 17,1.

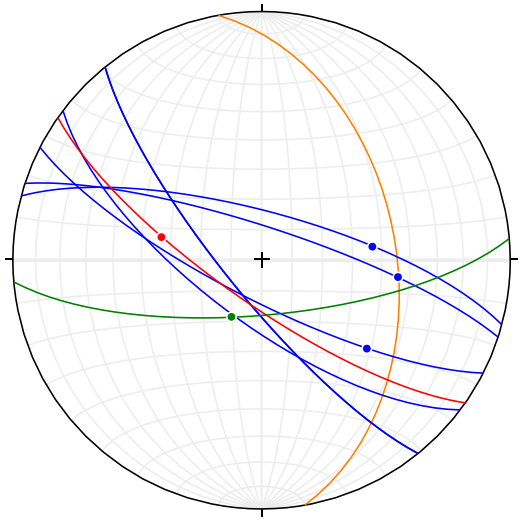

Figure 34. Structural features of locality 17 projected in a stereonet. Fault planes and associated slip-lines of sub-set 17,1 are represented by blue great circles and points. Weathered fault zone is represented in yellow. Red and green great circles represent faults not shown in Figure 33

Thin section sample 514 taken from the cataclastic zone is considered representative for structures included in sub-set 17,1. A highly heterogenous fabric is observed, varying from fine-grained ultracataclastic domains along major fracture zones, to protocataclastic domains where grains of the granitic gneiss protolith is preserved (Figure 35). Riedel fractures and displacement of fractured grains are identified (Figure 35). Both structures indicate a dextral kinematic throughout the sample, and thus confirm the somewhat vague kinematics from field observations.

Thin section sample 523, taken from another fault plane surface, also represents sub-set 17,1. Relative to sample 514, sample 523 is generally less deformed and is characterized by the granitic gneiss protolith. Strain appears to have been accommodated along fault-parallel fractures. Along these fractures grain size reduction is substantial, as illustrated in Figure 36G–H. Other microstructures giving evidence of deformation are; Riedel fractures (Figure 36A,D,E), fractured and displaced grains (Figure 36B–C,I) and releasing bends (Figure 36F). Nearly all these deformational microstructures indicate a dextral kinematic, which corresponds well to observations in thin section 514 and to in-field interpretations. Contrastingly, one domain of the thin section (Figure 36I) contains structures (fractured grain displacement and releasing bends) that are indicative of a sinistral kinematic. However, since the dextral features are of clear dominance, an overall dextral kinematic is determined as representative for sub-set 17,1. Nevertheless, it is possible that these sinistral indicators represent an earlier deformational phase which was later overprinted by a deformation characterized by dextral kinematic.

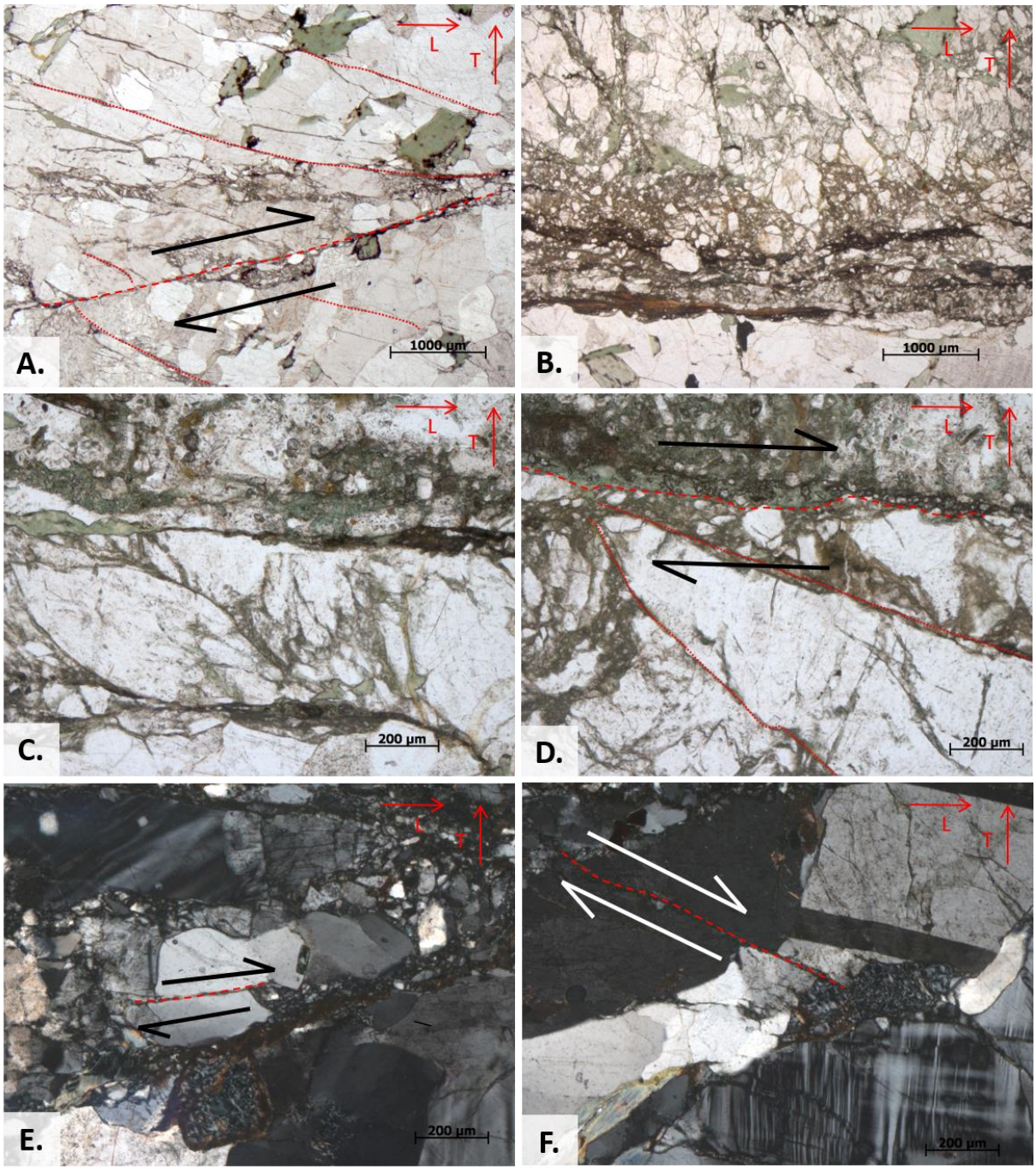

Figure 35. Thin section 514 taken from plane defining the margin of cataclastic zone (sub-set 17,1). A highly heterogenous fabric is observed, varying from ultracataclastic, fine-grained domains along major fracture zones to protocataclastic domains where grains of the granitic gneiss protolith is preserved. A.-D.) Riedel fractures associated to fault-parallel fractures indicating dextral kinematics. E.-F.) Fractured and displaced grains along fault-parallel fractures in. also indicating dextral kinematic.

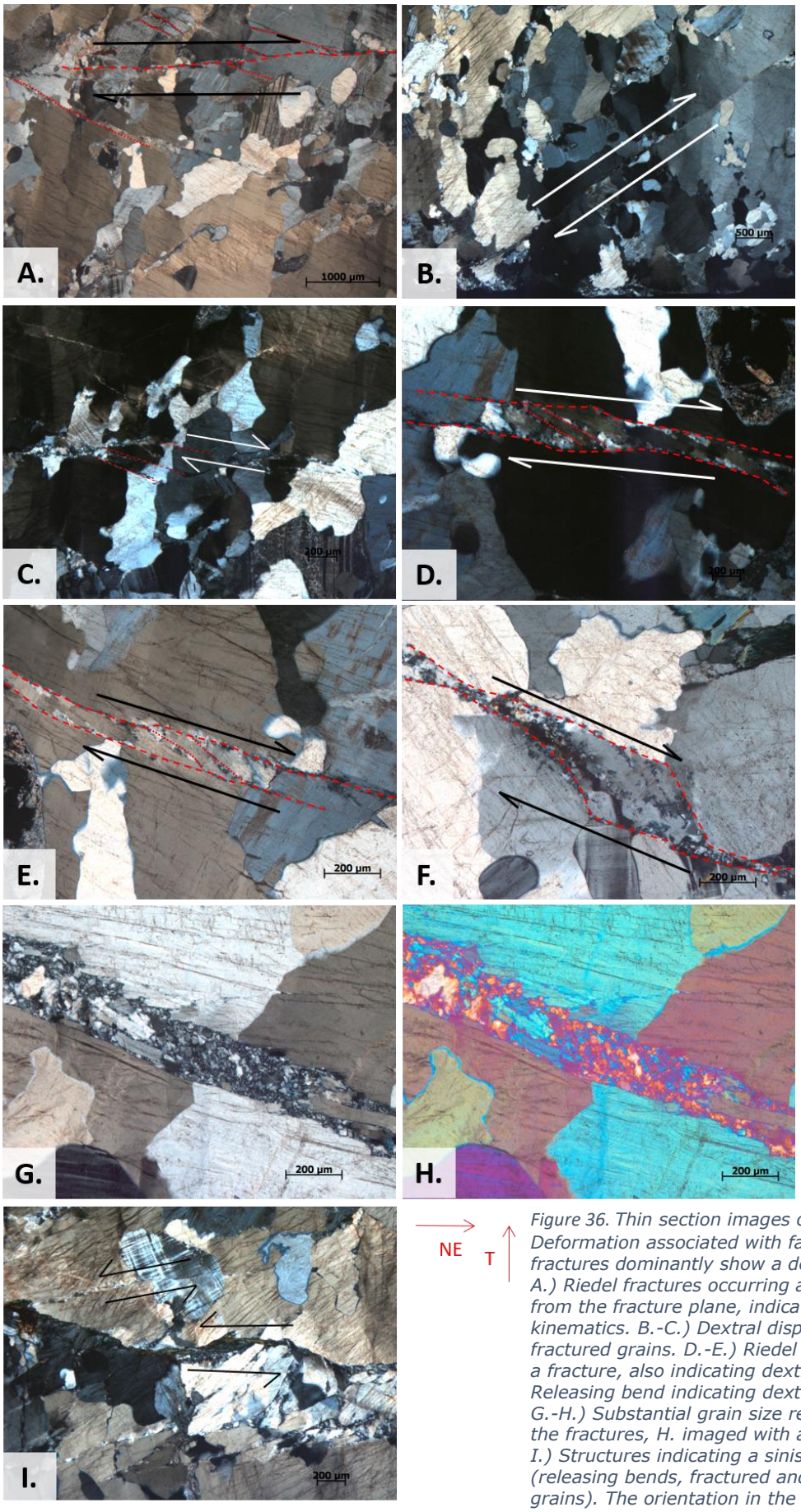

Figure 36. Thin section images of sample 523. Deformation associated with fault parallel fractures dominantly show a dextral kinematic. A.) Riedel fractures occurring at an angle out from the fracture plane, indicating dextral kinematics. B.-C.) Dextral displacement of fractured grains. D.-E.) Riedel fractures within a fracture, also indicating dextral kinematic. F.) Releasing bend indicating dextral kinematic. G.-H.) Substantial grain size reduction along the fractures, H. imaged with a gypsum plate. I.) Structures indicating a sinistral kinematic (releasing bends, fractured and displaced grains). The orientation in the bottom right corner applies to all images.

4.3.6 Locality 62

At locality 62, located slightly south of locality 1, another amphibolitic outcrop is studied. The rock is highly fractured and has a well-developed foliation. The fracture- and fault-planes generally follow the foliation and are sub-vertical with a NE–SW strike, as illustrated with red lines and black dashed lines in Figure 37. This relationship indicates that the foliation has provided planes of weakness to accommodate stress within the rock mass, thus promoting reactivation rather than new fracturing. Generally, the fault-plane surfaces are highly polished with a thin coating, likely of cataclastic or chloritic composition. A well developed, flat-lying slickenside lineation is observed in nearly all fault plane surfaces (Figure 37). Steps in the slickenside lineations are observed regularly and indicate a dextral strike-slip kinematic. In certain places, a lighter mineral appears to be deposited on the lee-side of the steps, also corresponding well to a dextral kinematic.

Thin section sample 537 (Figure 38) from this locality allows for further investigations of mineralization and kinematics. Grain drag along fracture surfaces indicate a dextral kinematic (Figure 38A-B), corresponding to the field observations. Figure 38C illustrates a fractured grain in a dextral kinematic environment (Figure 38D).

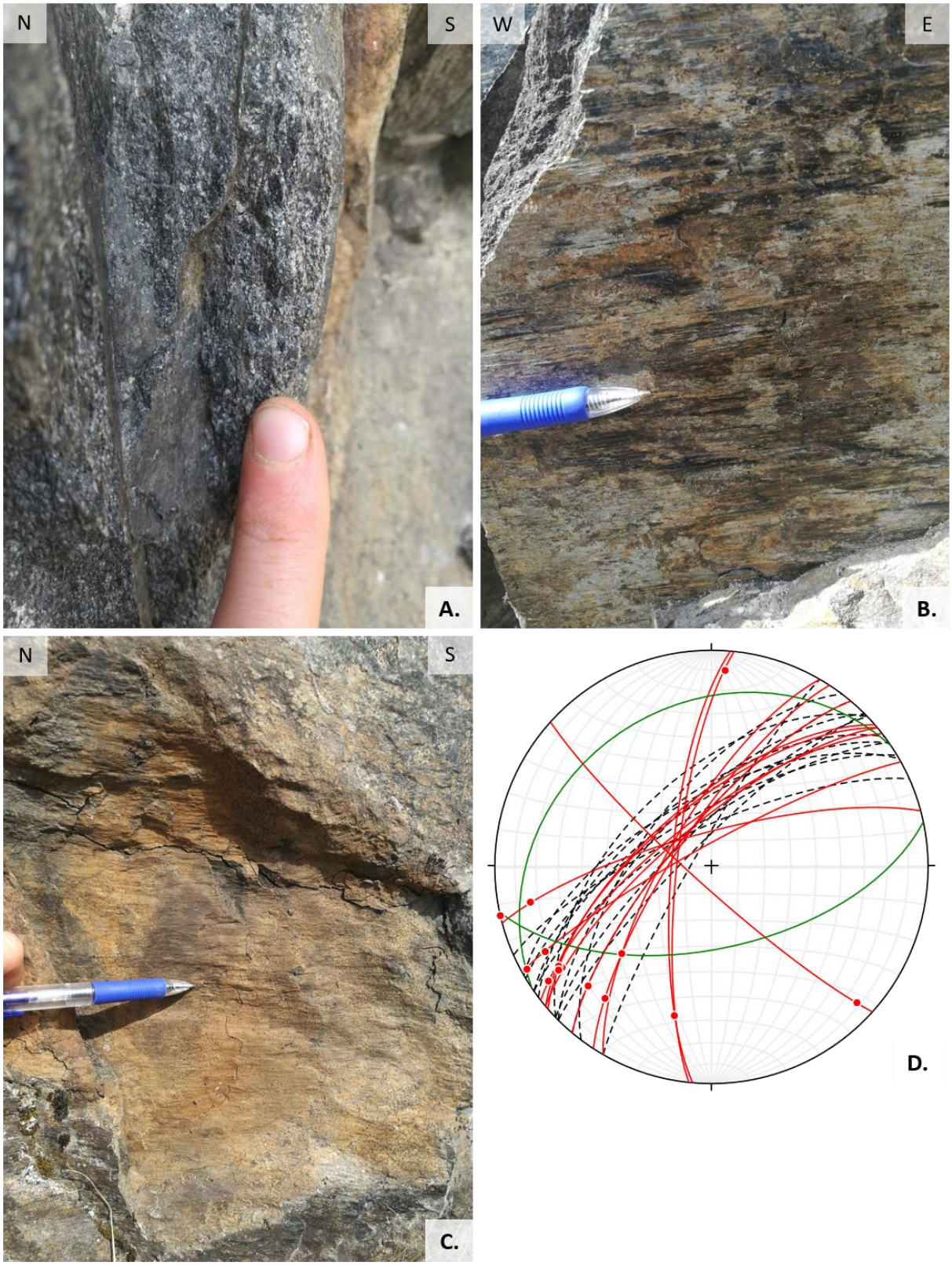

Figure 37. Structural features at locality 62. A.) Thin (few mm) fine-grained coating on the fault plane, likely cataclastic. B.-C.) Flat-lying slickenside on polished fault plane surfaces. C.) Straited surface revealed behind a similarly striated lens. All structures in A., B. and C. are represented by the red great circles and points in D. The fault planes occur parallel to the foliation (black dashed great circles in D.). The green great circles represent measurements that are not represented in photos A., B. and C.

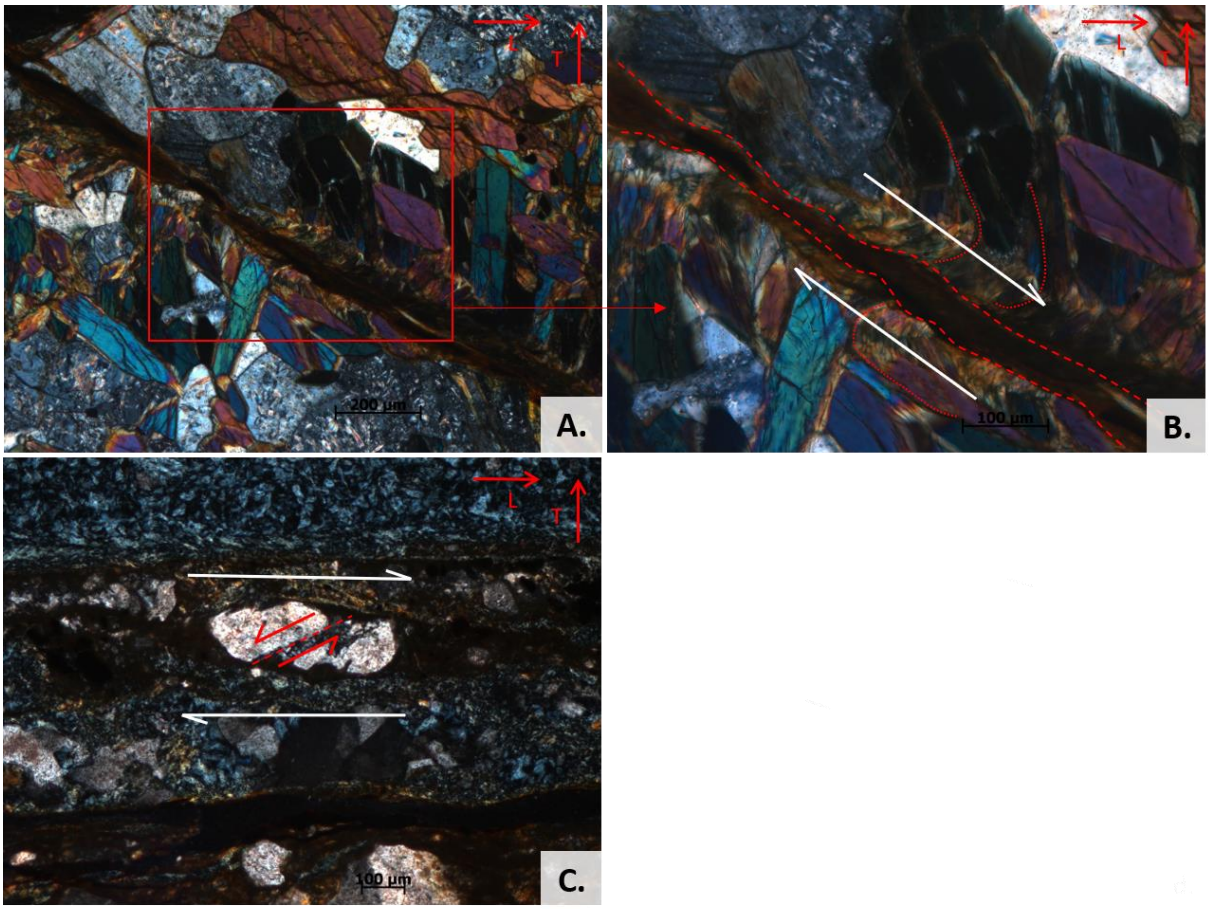

Figure 38. Thin section 537 exhibits a fabric varying from fine-grained ultra-cataclasite along fractures that have accommodated displacement, to a proto-cataclasite where the amphibolitic protolith is preserved. A.-B.) Grain-drag along a fracture indicating a dextral kinematic. C.) A fractured grain "suspended" in a cataclastic "flow" indicating dextral kinematics.

4.4 Paleo-stress analysis

Structural measurements from fourteen key localities, of which six are described in the section 4.3, form the basis for conducting a paleo-stress analysis of the study area. From these measurements, a total of 26 internally homogenous sub-sets were identified, each with a corresponding stress tensor. These are summarized in Appendix 1. The sub-sets were mainly distinguished based on their fault plane orientation and associated slip-line orientation and kinematic. From these sub-sets some common structural trends are identified. The faults group into two major strike-orientations; NE–SW, and NW–SE (Figure 18A–B). Despite some fault dip variation, most of the fault planes are steep to sub-vertical. The slip-lines vary from dip-slip, through oblique-slip, to strike-slip. In cases where kinematics are identified in the field, nearly all dip-slip lineations indicate normal kinematics, except for some measurements at localities 59 (sub-set 59,2) and 57 (sub-set 57,1) in the amphibolites (Appendix 1). Kinematic indicators observed in conjunction with strike-slip lineations are dominantly indicative of dextral movement. A few sinistral kinematic indicators are observed, but these are generally associated with fault planes oriented at a high angle to those with dextral kinematic (f. ex sub-set 62,0, Appendix 1). These two sets of strike-slip faults are interpreted as conjugate sets.

Using the orientation and kinematics of the faults, the sub-sets can be grouped into three fault population sets; *Set 1*: NE–SW striking normal faults, *Set 2*: NE–SW striking dextral strike-slip faults (and conjugate NW–SE sinistral faults), and *Set 3*: NW–SE striking

normal-dextral oblique-slip faults. Faults expressing slightly oblique kinematics are also included in Set 1 and 2, given that associated stress tensors are compatible with the overall stress regime of the set. Fault planes striking NW–SE generally exhibit a normal-dextral oblique slip (Set 3), except a few fault planes with sinistral strike-slip movement included as conjugates in Set 2. Table 1 gives an overview of the three fault population sets. These three fault populations include nearly all sub-sets from the key localities selected as a representation for the entire studied area. Eight sub-sets were, however, excluded in the final grouping of fault populations as they did not fit into any of the three defined groups. These are represented by a grey cell-background in Appendix 1. Stress tensors derived from a large base of structural measurements are considered more valid than those derived from few measurements.

Other fault plane characteristics such as fault plane mineralization and character are consistent within each of the three grouped fault populations. This is elaborated further in this section.

4.4.1 Set 1

A *NW–SE extensional stress regime* was determined through a paleo-stress inversion of the fault slip-data of the Set 1 fault population (Table 1). Several steep, NE–SW striking tensile joints also contribute in determining this stress regime. The direction of extension varies between N–S and WNW–ESE, and is denoted by a mean σ_3 orientation of 09/327.

Structural features in this group are observed in all three main lithologies of the studied area. When comparing the sub-sets of Set 1, it becomes clear that the stress field computed from the granites (Appendix 1) corresponds almost perfectly to the stress regime of the whole fault population of Set 1 (Table 1), whereas the stress fields calculated from localities in the amphibolites and the granitic gneisses (Appendix 1) deviate more. The stress field computed from the amphibolitic sub-sets generally comprise a N–S direction of extension, while the granitic gneiss sub-sets give a WNW–ESE extension direction. Differences in mechanical rock properties surely contribute to a certain variation in how the rock mass is deformed in response to a given tectonic stress field, including the orientation of brittle structures. While the granite is massive and mechanically isotropic, the other rocks are more anisotropic. Existing planes of weakness, such as foliation, likely influence how and where the strain is accommodated within the rock mass. Fault planes may therefore be generated at un-optimal orientations to the present stress field. Consequently, some lineations on the fault planes of the amphibolites and the granitic gneisses express a certain degree of obliquity, although they were generated in an extensional stress regime.

Most fault planes in this set have a light to dark green chloritic mineralization with slickensides providing slip-line data. Some of the lineations are measured on fault planes with a tectonically grooved or striated surface. Generally, the fault plane surfaces belonging to this fault plane population exhibit a rough and unpolished surface. A different mineralization is associated to the plane surfaced of the tensile joints in Set 1. These surfaces accommodate a sporadic light mineralization with an apparent syntaxial growth - as is characteristic of tensile joints.

4.4.2 Set 2

Inverting the structural data of Set 2 results in a paleo-stress field with a sub-vertical σ_2, sub-horizontal σ_1 and σ_3, and a resulting stress ratio, R, of 0,45 (Table 1). The

corresponding inverted stress ratio, R', is 1,55 and indicates that the features of Set 2 were generated in a *transpressive stress regime*. An E–W shortening component with a mean σ_1 orientation of 06/086 generated dextral kinematics along the NE–SW fault planes and sinistral kinematics along the NW–SE fault planes.

Structures from all three main lithologies of the area are represented in this set. However, only a few are found in the Tørdal granite (sub-set 35,0, Appendix 1), whereof all have sinistral kinematics and strike NW–SE. A few faults of this orientation are also registered in the amphibolites and the granitic gneisses, but are significantly less prominent compared to the dominating trend of NE–SW striking fault planes. The strong correlation in orientation of the striated fault planes and the foliation of the amphibolites (Figure 37), is a clear indication that, in the amphibolites, strain was being accommodated along these (pre-existing) planes of weakness. Although the fault planes in the amphibolites appear to be strongly influenced by the foliation, the coinciding stress tensor orientation of the fault planes in the granitic gneisses confirm that the reconstructed stress field from the amphibolite sub-sets is representative for the studied area.

Polished fault planes with a chloritic mineralization or thin cataclastic zone are characteristic for the faults of Set 2. The coating on the fault planes range from a light green to dark green and brown colour. On the mineralized or cataclastic surfaces, slickensides are the dominant lineation type and kinematic indicator providing slip-line data used in the paleo-stress inversion.

4.4.3 Set 3

By paleo-stress inversion of the normal-oblique slip, NW–SE striking faults of Set 3, another extensional stress regime is reconstructed (Table 1). The extension is oriented in a NE–SW direction, with a mean σ_3 orientation of 05/027. A moderately plunging σ_1 (66/127) causes a somewhat high stress ratio of 0,57 and creates a deformational setting where oblique slip occurs. This reconstructed stress field is of non-Andersonian character, in which none of the principal stress axes have a vertical orientation. Non-Andersonian fault architecture can occur in areas where the bedrock is highly fractured, providing a series of pre-exisiting planes of weakness. The deformation pattern will then not only be responsive to the associated tectonic stress field, but also to these pre-existing planes of weakness.

Granitic gneisses and amphibolites are represented in the fault population of Set 3. The fault planes in the amphibolites (in Set 3) generally strike E–W, a slight deviation from the faults in the granitic gneisses and the general orientation of Set 3 structures. The kinematics vary from normal-dextral oblique-slip to a near perfect normal dip-slip at one of the granitic gneiss localities. If the fault population of Set 3 is a reactivation of pre-existing faults or fractures, a certain variation in both the orientation of the fault planes and the kinematic sense accommodated in the faults is to be expected. Although no structures of Set 3 were observed in the granites, the possibility that these structures also exist there should not be excluded.

While the faults of Set 1 and 2 generally have a chloritic mineralization or cataclastic coating on plane surfaces, most of the fault planes in Set 3 comprise a light-coloured surface mineralization, most often calcite. Slickensides on the mineralized surfaces provide slip-line data with kinematics where proper indicators are observed.

Set 1	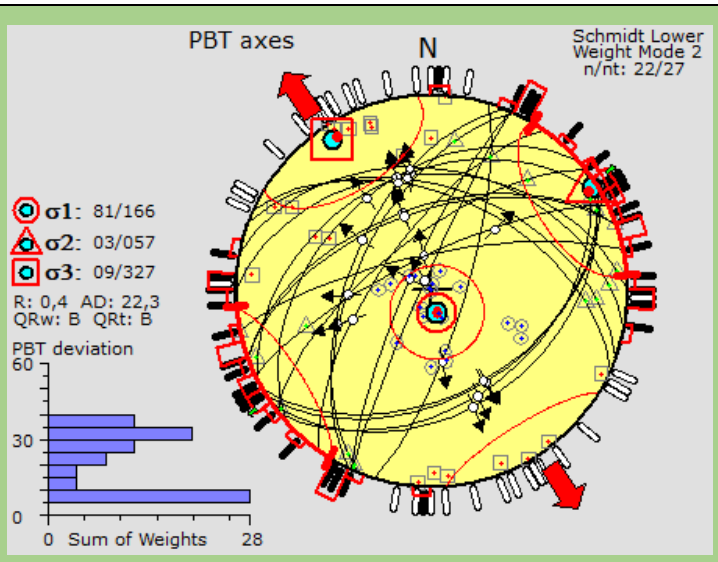	R=R'=0,4 NW–SE extension Angular deviation: 22,3°
Set 2	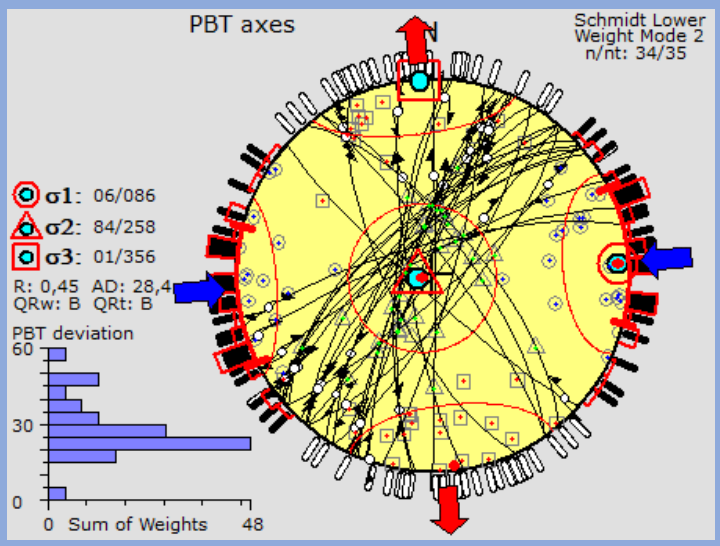	R=0,45 R'=1,55 E–W transpression Angular deviation: 28,4°
Set 3	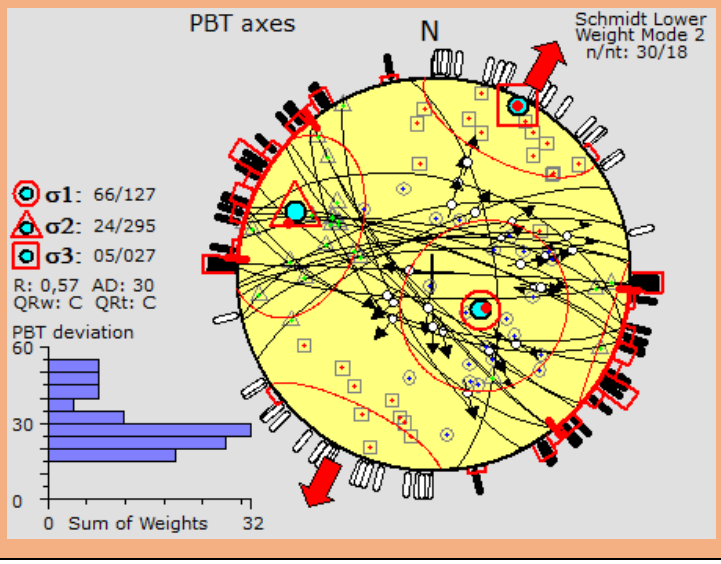	R=R'=0,57 NE–SW extension Angular deviation: 30°

Table 1. Reconstructed paleo-stress regimes of three sets of fault populations based on sub-sets in Appendix 1. Stress tensors are reconstructed in the Win-Tensor program (Delvaux & Sperner, 2003).

4.5 Magnetic modelling

Through the lineament study (Hilde Gunleiksrud, 2017), major topographic- and magnetic lineaments were generally found to coincide well, which is likely a result of the lower magnetic susceptibility within the brittle structure, relative to the undeformed surrounding host rock. 2D forward magnetic modelling is carried out to better understand if the reduced magnetization within the brittle structures is related to deep weathering, hydrothermal alteration, or a combination of the two. The linear anomaly in the northwest region of the studied area, coinciding with the *Fisarbakken lineament*, is chosen for further investigation due to its significant anomalous response and sufficient quality of outcrops that allowed for general observations, structural measurements and sampling for petrophysical analysis (Figure 39).

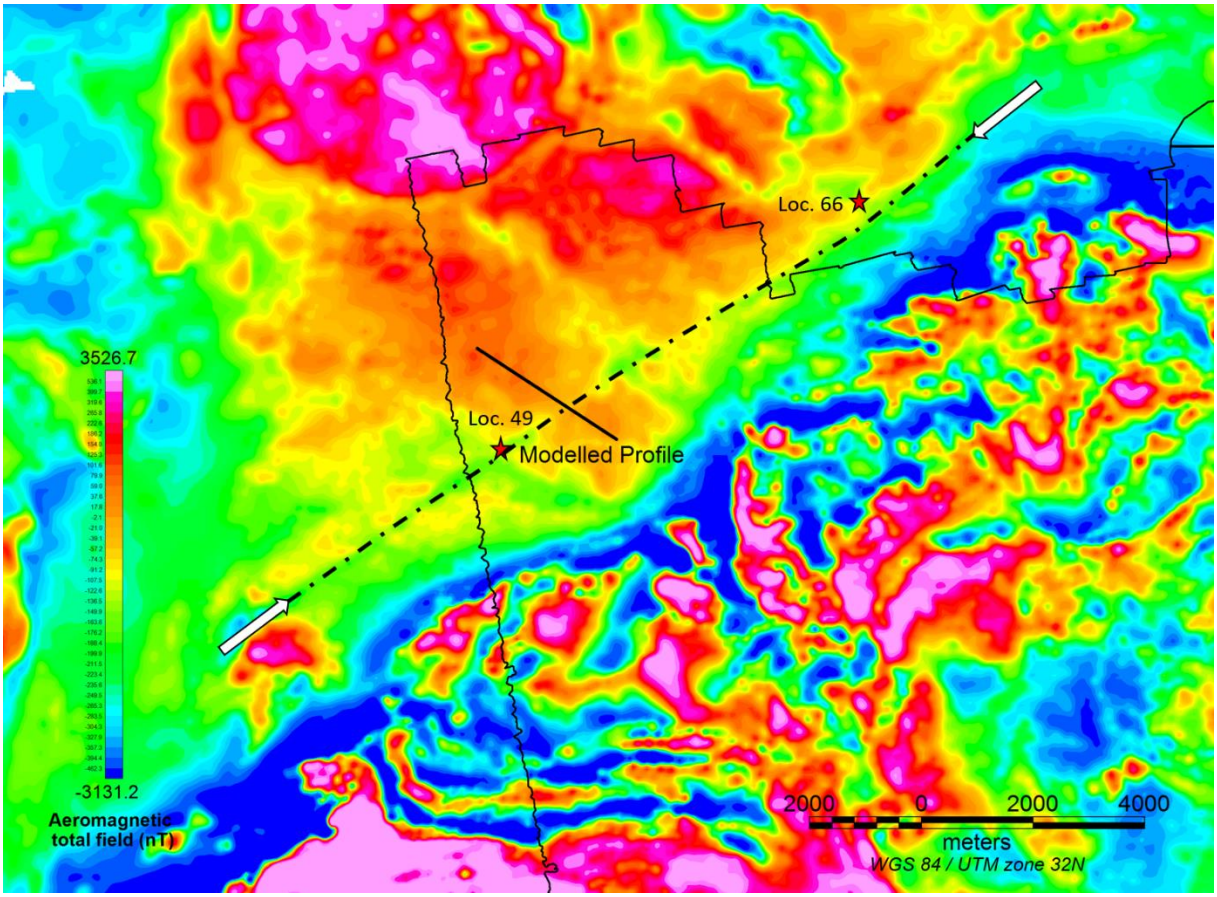

Figure 39. Aeromagnetic map showing the modelled profile crossing the Fisarbakken lineament. The arrows point out the magnetic anomaly associated to the Fisarbakken lineament. The modelled profile across the lineament is represented by the black line. Red stars locate localities 49 and 66. Dashed line traces the trough of the anomaly. The measured magnetic response along this line is shown in Figure 40.

4.5.1 The 'Fisarbakken lineament'

The 17 km long *Fisarbakken* lineament (Figure 39) is one of the most well-defined magnetic lineaments in the study-area, and it coincides with an equally well-defined topographic depression. Figure 40 shows the magnetic response along the trough of the negative anomaly, and follows the Fisarbakken lineament from SW to NE. This profile is constructed in GM-SYS to give an idea of the magnetic response along the lineament and is not used directly for modelling purposes. The mean response is -175 nT with significant variations along the profile. Variations in the magnetic properties of the rocks along the flanks of the lineament are likely a significant contribution to this effect. Nevertheless, the magnetic response along the centre of the anomaly is significantly

lower than that of the bedrock bordering the Fisarbakken lineament, which reaches +50 nT in certain areas (Figure 39).

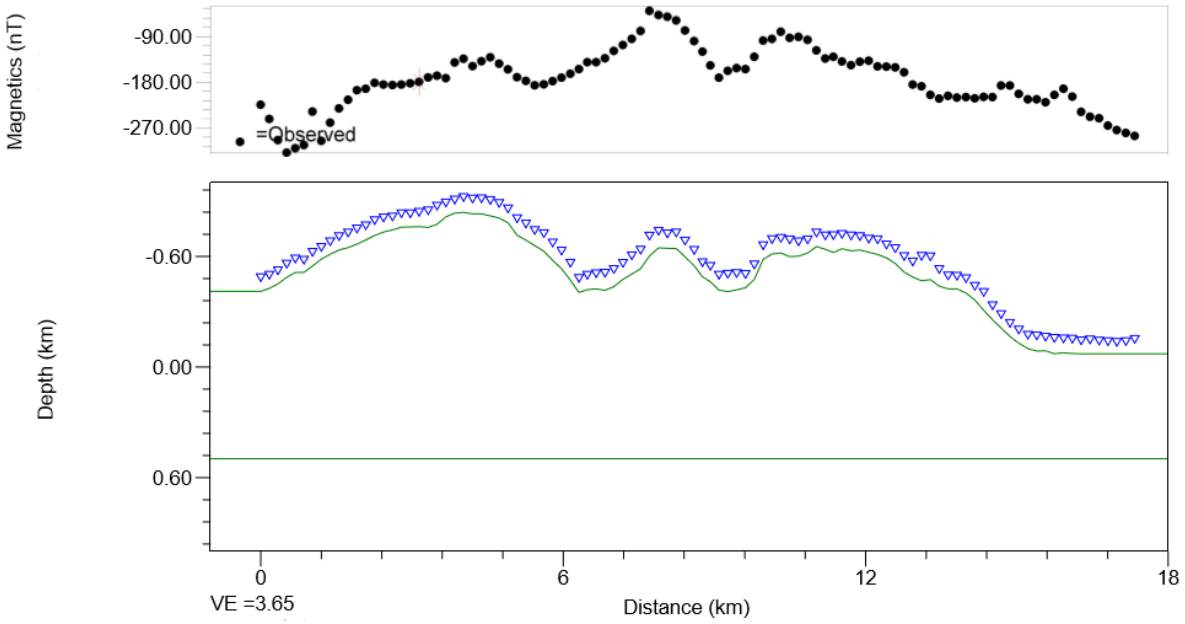

Figure 40. The magnetic response measured along the Fisarbakken lineament from SW to NE. The profile is traced by following the trough of anomalous magnetic response. The topographic surface is illustrated by the green line (with negative values representing altitude in km above sea level), the blue triangles represent the height of the magnetometer, and the black dots denote the measured magnetic response. VE: vertical exaggeration.

To construct a 2D depth model explaining possible origins of the magnetic anomaly along the Fisarbakken lineament, some structural, petrophysical, and geographical constraints are needed. The following section uses structural field data, observations and petrophysical field samples combined with theory to build a structural, geometrical and petrophysical framework for the model.

4.5.1.1 Structural and geometrical framework

In the northwest corner of the study area, the road Rv. 38 crosses the low anomaly associated with the Fisarbakken lineament (Figure 39). A roadcut of highly fractured granitic gneiss crops out at this locality. The road crosses the anomaly at a high angle and granitic gneiss is present on both the north and the south side of the anomaly. A variable fracture density is observed throughout the outcrop, but a general increase in fracture density occurs towards the centre of the lineament. In highly fractured domains, the distance between the fractures is only a few centimetres, whereas in more massive domains this distance can be as large as a few metres. Generally, two sets of fractures (J1 and J2) are registered and measured (Figure 41). These two sets comprise strike orientations which are nearly perpendicular to one another and both consist of sub-vertical fractures. The total width of the highly fractured and faulted zone extends across the magnetic anomaly and is approximated to 180–250 m. Note that this distance includes an overgrown area near the centre of the anomaly. This approximation thereby assumes the presence of fractures and/or faults below the overburden.

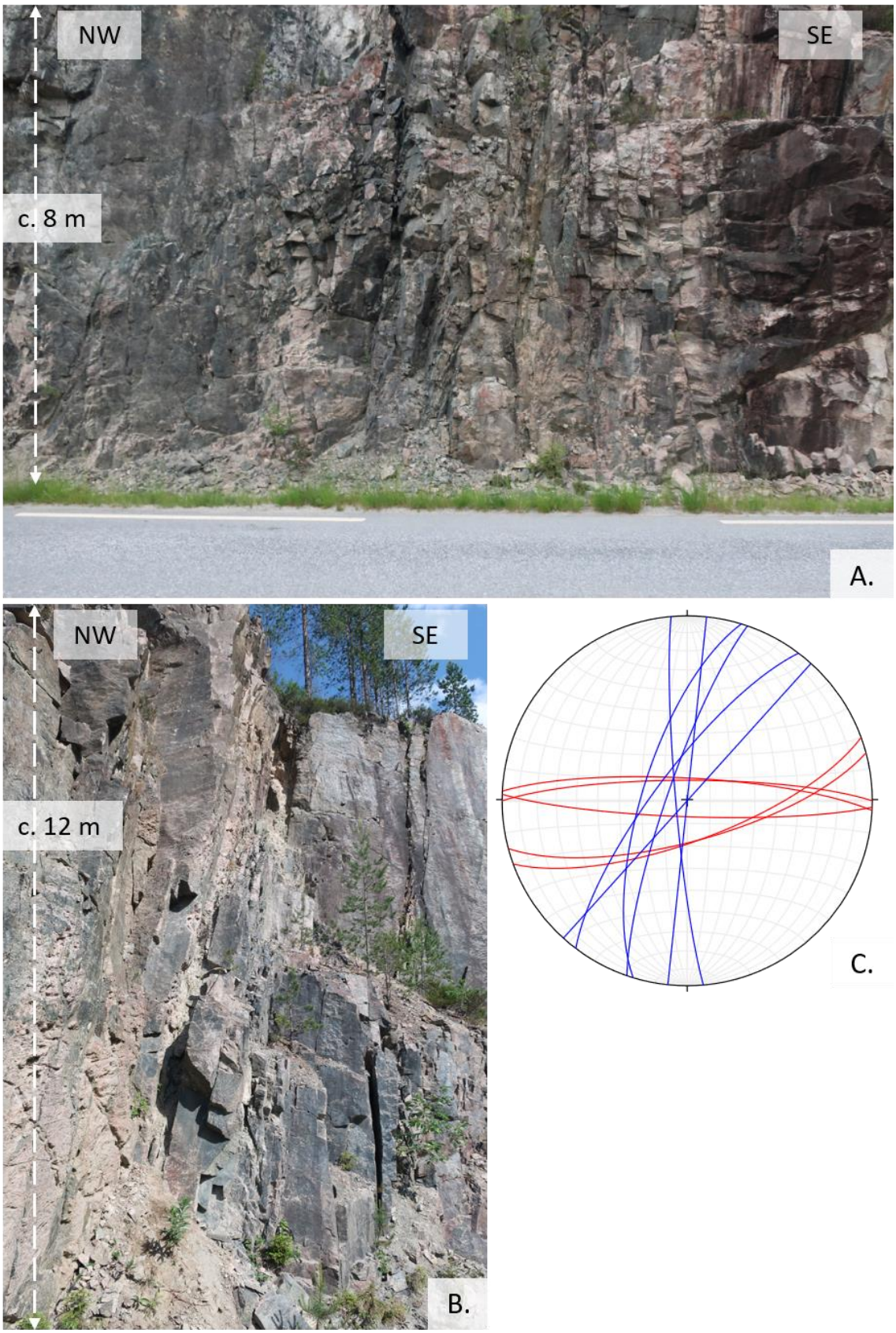

Figure 41. A.-B.) Highly fractured outcrop of granitic gneiss at locality 49. The vertical height of the outcrop varies between appr 2 and 15 m, the part of the outcrop in A. is c. 8m and in B. it is c. 12m. C.) Stereonet showing two sets of fractures that were observed and measured; J1 (red) and J2 (blue).

Unfortunately, in the centre of the topographic lineament, no rocks crop out. Approximately 40 m south of the centre of the topographic lineament, however, a fault (hereafter referred to as *Fault A*) with a weathered core of at least 1 m is observed (Figure 42). Fault A is situated close to the trough of the anomalous response and is thus assumed representative for structural features associated to the anomaly (locality 49 in Figure 14, Figure 39). The weathered core is defined by a steeply dipping fault plane striking NE–SW, an orientation which corresponds well to the Fisarbakken lineament. Two representative fault plane measurements with associated lineations are shown in the stereonet in Figure 42, and indicate extensional to oblique faulting. Lineations are observed both in a dark green and a light-coloured fault plane mineralization. Paleo-stress inversion determines that fault A is included in Set 1 (see sub-set 49,0 Appendix 1, Table 1) and is proposed to originate from a NW–SE extensional regime. In addition to Set 1 faulting, faults of Set 2 and 3 were also registered at locality 49 (see sub-sets 49,3 and 49,4 in Appendix 1, Table 1). Lineations observed in fault planes of Set 2 and 3, were found exclusively in a light-coloured mineralization.

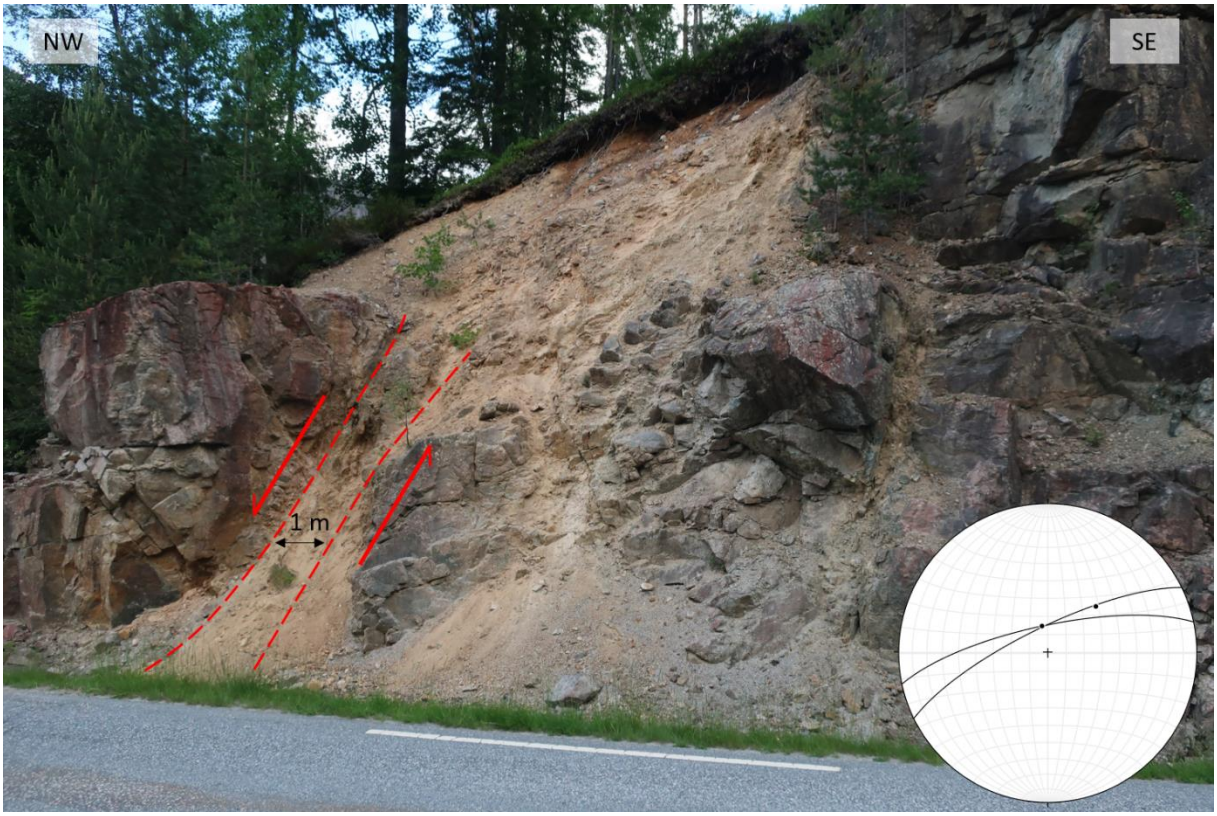

Figure 42. Photo of Fault A at locality 49. The dashed red lines illustrate the weathered fault core. Sample 528 taken from centre of fault core. Two representative fault plane and associated lineations are plotted in the stereonet.

4.5.1.2 Petrophysical framework

Samples acquired in the field for petrophysical analysis are used as references in the 2D modelling and are given in Table 2. These samples are acquired at localities 49 and 66 which are shown in relation to the Fisarbakken lineament in Figure 39. Sample 528 is collected from the weathered fault core of Fault A (Table 2, Figure 43) and has a susceptibility of c. 0.001 SI. This is a considerably lower susceptibility than that of pristine, un-weathered bedrock in the surroundings (Table 2, Figure 43), and is assumed representative for susceptibility values of deep-weathering material in the model.

The susceptibility value for hydrothermally altered material is represented by samples 530 and 539 (Figure 43). Sample 530 is a cataclastic rock (Figure 43, Figure 44, Table 2) acquired from the fractured zone at locality 49, appr. 10 m south of Fault A. Sample 530 has a very low susceptibility of c. 0.0005 SI (Figure 43, Table 2). Thin section analysis of Sample 530 (Figure 44) identifies a cataclastic fabric varying from a fine grained ultracataclasite to a fragmented protocataclasite. Feldspar fragments of the protolith are frequently altered by sericitization, thus indicating hydrothermal alteration of the rock. The observation of chlorite within the cataclasite is another indication of the presence of fluids at the time of deformation. Sample 539, also with a low susceptibility of 0.0005 SI (Figure 43, Table 2), is acquired from the middle of a deep topographic lineament further east along the Fisarbakken lineament (locality 66 in Figure 39). This sample is a cohesive granitic gneiss with pink and dark green minerals appearing to be altered through major chloritization (Figure 43). Altogether an approximated susceptibility of 0.0005 SI is applied to the hydrothermally altered profiles in the models.

Sample nr	Loc.	Lithology	UTM X (m)	UTM Y (m)	Volume (cm^3)	Density (g/cm^3)	Pore volume (cm^3)	Porosity (%)	Susceptibility (10^{-6} SI)	Notes	Model application
528	49	GRAG	135055,2	6585550,6	60,94	2,41	2,99	4.91	1039	Weathered rock from fault core of Fault A.	Deep weathering in anomaly
530	49	GRAG	135055,2	6585550,6	95,73	2,60	0,33	0.34	473	Cataclastic rock from central part of fracture zone.	Hydrothermal alteration in anomaly
529	49	GRAG	135055,2	6585550,6	344,47	2,64	0,84	0.24	14553	Pristine rock, 10 m SE of anomaly.	Pristine rock outside of anomaly
531	49	GRAG	135022,3	6585653,7	167,75	2,64	0,53	0.02	6700	Pristine rock, NW side of anomaly.	Pristine rock outside of anomaly
539	66	GRAG	142374,1	6589240,2	156,19	2,57	2,82	1.81	462	Cohesive rock, middle of topographic lineament. Close to magnetic anomaly.	Hydrothermal alteration in anomaly

Table 2. Petrophysical values of field samples relevant for the modelling of the Fisarbakken lineament. Samples are from localities 49 and 66.

An average susceptibility of pristine rock from the north (sample 531) and south side (sample 529) of the anomaly at locality 49 (Table 2, Figure 39) is used as a reference for the pristine granitic gneiss in the model. The magnetization of the granitic gneiss is directly related to the concentrations of magnetite, which in the pristine samples vary as a function of the primary distribution of magnetite in the granitic protolith. These variations are illustrated in the scatter plot of Figure 43. Due to these variations, the magnetic response from a bedrock of granitic gneiss fluctuates significantly. To accommodate the fluctuations, bodies of pristine granitic gneiss with varying susceptibilities (based on Figure 43) are included in the model (see Model 2 in section 4.5.3).

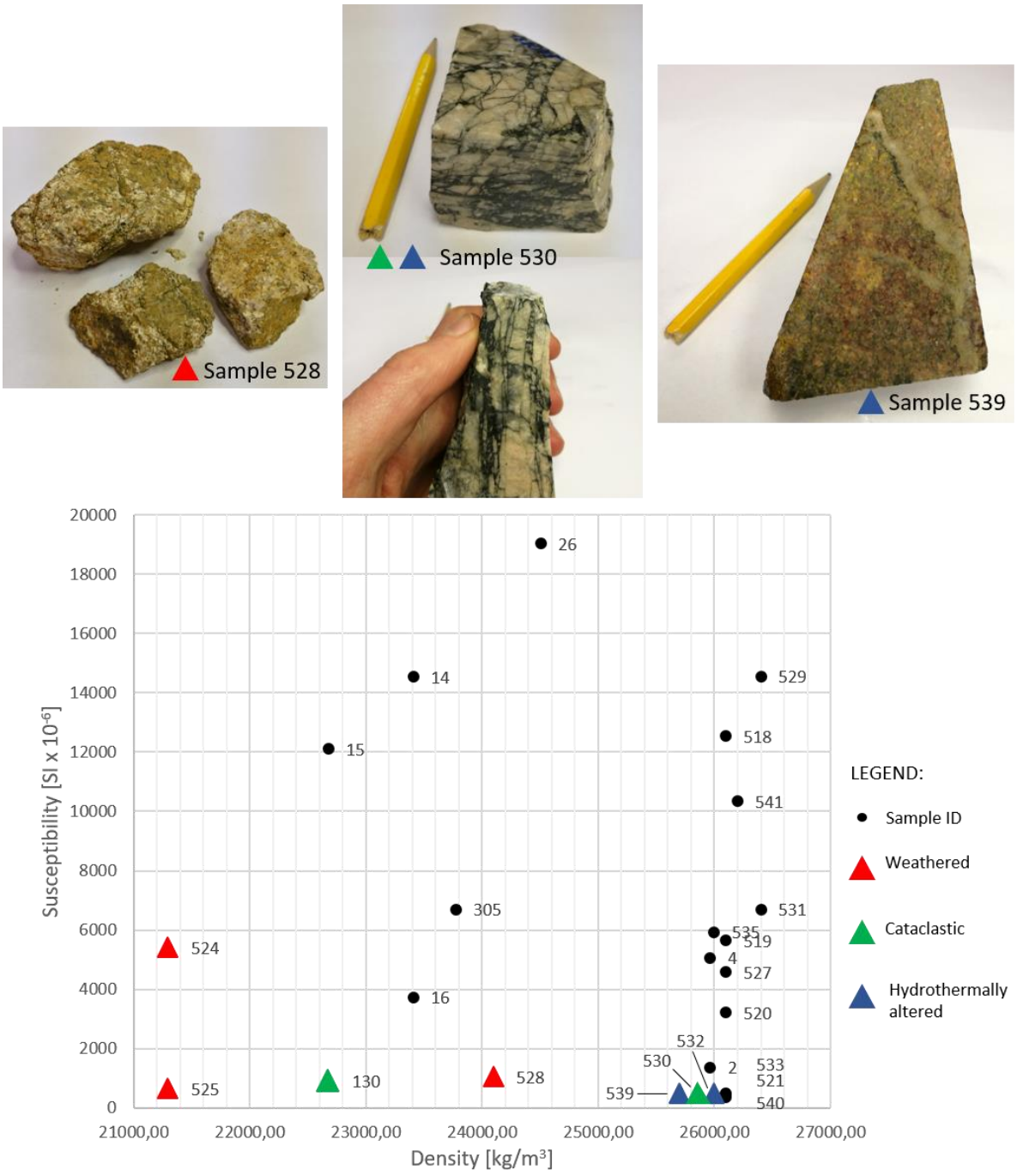

Figure 43. Relationship between susceptibility and density in samples of granitic gneiss from Drangedal and Nome, collected by me (sample numbers in the 500s) and BITE team members. The samples plot with susceptibilities ranging from 400 to 20 000 SI x 10^{-6} and densities ranging from 22 000 to 27 000 kg/m^3. This is a considerable variation in susceptibility, with some lower range likely resulting from deep weathering and hydrothermally alteration. Samples in which these processes have (likely) been significant are indicated with red, green and blue triangles. The cataclastic rocks, represented by green triangles are likely also affected by hydrothermal alteration. Samples 528, 530, and 539 used for the modelling, are pictured above the plot.

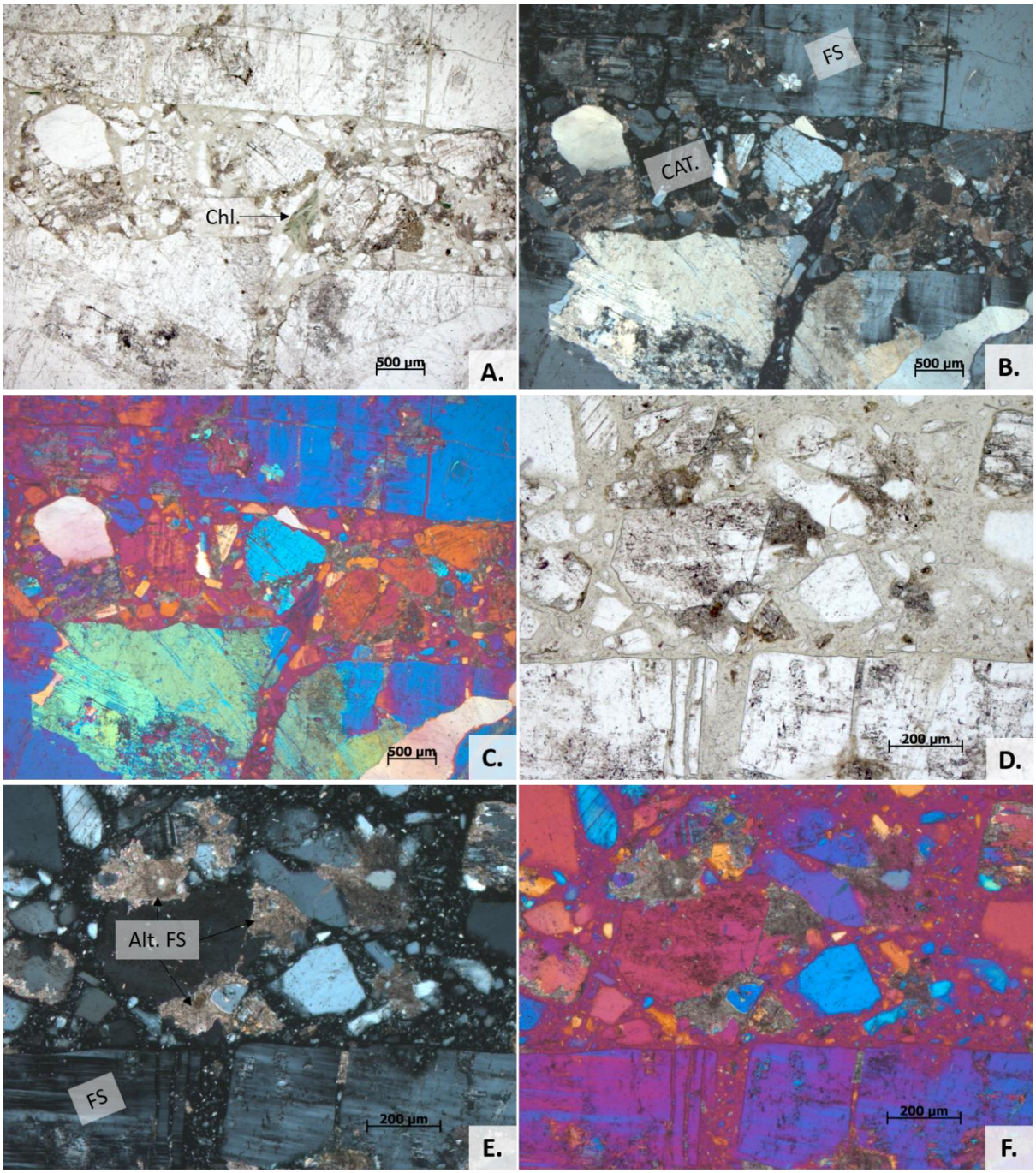

Figure 44. Thin section sample 530. A.-C.) Representing the same domain of the thin section analysed with plane polarized light (A), cross polarized light (B) and gypsum plate (C). D.-F.) Representing another domain of the thin section analysed with plane polarized light (D), cross polarized light (E) and gypsum plate (F). In general, a cataclastic (CAT.) domain (varying from fine grained ultracataclastic to fragmented protocataclastic) dominates together with feldspar (FS) grains (protolith). Many feldspar fragments within the cataclastic zone show signs of alteration (Alt. FS), due to sericitization. Chlorite (Chl.) is observed within the cataclasite.

5.4.1.3 Summary of framework for 2D magnetic modelling

The Fisarbakken lineament is interpreted as a major fault zone. This interpretation is based on; 1) the lineament's pronounced signature, both magnetically and topographically, 2) the lineament's NE–SW strike – which is a common fault orientation within the studied area, and 3) the increase in fracture density towards the lineament, and 4) the representativeness of Fault A in terms of orientation and character. Fault A is not of sufficient magnitude alone to account for the magnetic anomaly of the Fisarbakken

lineament. However, a series of similar faults with a reduced susceptibility, have the potential to account for this response within the approximated fault zone of 180–250 m. Through this structural, geometrical and petrophysical analysis, the following framework for the Fisarbakken lineament is suggested;

- Lineament length: 17 km
- Fault zone width: 180–250 m
- NW–SE extension (based on paleo-stress analysis of Fault A)
- Sub-vertical fault, dipping steeply towards NW (assuming Fault A as a proxy for the Fisarbakken lineament)
- Background susceptibility of pristine granitic gneiss: 0.012 SI with local variations between 0.004 and 0.01 SI
- Susceptibility of deep weathered fault rock: 0.001 SI
- Susceptibility of hydrothermally altered fault rock: 0.0005 SI

4.5.3 Models

A geophysical modelling such as this involves a forward modelling process, in which a geological/petrophysical sub-surface model is constructed to mimic an observed geophysical field – in this case; aeromagnetic data. Due to the ambiguity of potential field data, an infinite number of models can theoretically fit the observed magnetic data. However, using structural, geometrical and petrophysical constraints as a framework, the uncertainty can be reduced, and eight possible models are constructed across the Fisarbakken lineament to test possible scenarios. Figure 39 shows the location of the profile across the anomaly. The modelling is performed in GM-SYS (Geosoft Inc., 2015) and the results are displayed in Figure 45 through Figure 55. The upper part of the figures show the observed magnetic response (black dotted curve), the calculated magnetic response (blue curve) and the root-mean-square (RMS) model error (red curve) across the modelled profile from southwest (left) to northwest (right). Note that the symbology is somewhat different in Model 1, which investigates the topographic effect (Figure 45). The 2D depth-model is shown in the lower part of the figures. These models include *measuring stations* (magnetometer height derived from flight height) displayed with blue triangles, the *surface topography* displayed by the green line and *subsurface properties* modelled below the topographic surface. The measuring stations and surface topography remain constant throughout all models, whereas the subsurface properties vary while aiming to minimize the error between the calculated and observed response.

Model 1 (Figure 45) investigates the effect of topography relative to flight height. A model is constructed with a homogenous magnetic body, the original topography as a surface and a background susceptibility of 0.012 SI. To minimize edge effects, GM-SYS models have a 'default' lateral extent of 60 000 km (infinite, for all practical purposes). The vertical extent is defined by the user and is set to c. 1700 m. Consequently, the only magnetic variation is due to the topographic surface which introduces a noticeable relative variation in the thickness of the magnetic body and varying magnetic volume. The variation in thickness of the magnetic body has an impact on the calculated response, which varies depending on flight altitude and whether the magnetic field is observed at a constant barometric height or at constant altitude over the topographic surface (drape). However, the calculated response of such a model is exclusively a result of varying model thickness and observation height, which allows us to test and quantify inferred erroneous magnetic anomalies due to imperfect drape flight. Model 1 compares the *calculated* magnetic response using the *actual magnetometer height* (black dotted

line) to the response using a *constructed constant magnetometer height* of 55 m above the topographic surface (solid blue line). The latter does not contain any topographic effect since the amount of air between the measuring station and the topographic surface remains constant. Therefore, areas where the dotted curve deviates from the solid curve indicates the presence of a topographic effect. The two curves generally coincide very well (Figure 45). Minor deviations of about 5 nT are observed at points (see 1 km and 1.2 km on horizontal model axis) corresponding to a topographic low and high where it was likely difficult for the helicopter to maintain a constant flight height above the topography. Generally, the topographic effect is minimal. It can therefore be confirmed that the measured magnetic anomaly across the Fisarbakken lineament results (almost) entirely from variations in subsurface susceptibilities.

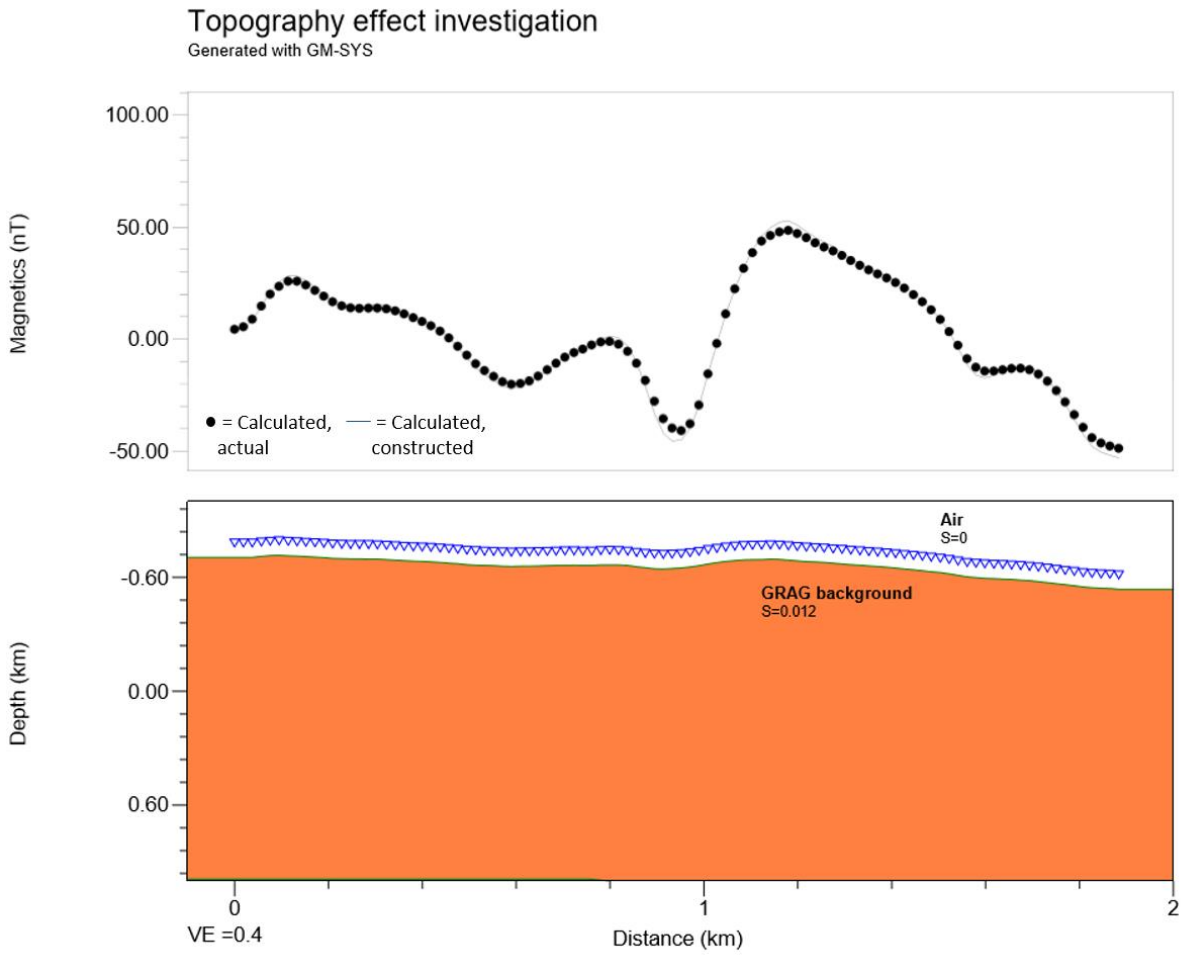

Figure 45. Model 1 to investigate the topographic effect. Homogenous subsurface with susceptibility (S) = 0.012 SI. Black dotted curve: calculated response using actual magnetometer height data. Solid blue curve: calculated response using a constructed constant magnetometer height of 55 m (above topographic surface). Topographic effect is illustrated by deviation of the two curves. Profile runs from northwest (left) to southeast (right). VE: vertical exaggeration, GRAG: granitic gneiss.

The aim of the modelling is to investigate the effect of various fault-zone geometries and properties in producing an anomalous response. Therefore, the modelled area outside of the fault-zone, as shown in *Model 2* (Figure 46), is kept constant throughout the following models. Model 2 gives a framework for the construction of models 3 to 8. Model 2 assumes that all variations in magnetic response (except the Fisarbakken lineament

anomaly) are due to susceptibility variations in the granitic gneiss. Bodies with susceptibilities varying between 0.004 SI and 0.01 SI are introduced to mimic the observed response outside of the fault zone as accurately as possible. These susceptibility values are based on the range of values for pristine (un-weathered) granitic gneiss observed throughout the study area (Figure 43). The resulting model has a calculated response that differs from the observed *only* across the fault-zone. With this as a framework, various fault-zone geometries and properties can be modelled, and their effects be compared.

The shape of anomalous magnetic responses may indicate the dip or geometrical shape of the bodies of contrasting susceptibilities in the subsurface. For instance, as observed in the measured response across the Fisarbakken lineament (Figure 45), the trough has a steeper slope on the right (southern flank) than on the left (northern flank). Assuming a fault or a fault zone as the source of the anomaly, such shapes of magnetic response typically indicate a fault dip toward the side with a gentler slope. This implies that the faults associated to the Fisarbakken lineament should have a general northwards dip. This inference corresponds well to the structural framework described by Fault A and other NE–SW striking faults, generally steeply dipping towards north. Accordingly, the faults introduced in the models have a steep (c. 80°) dip towards north.

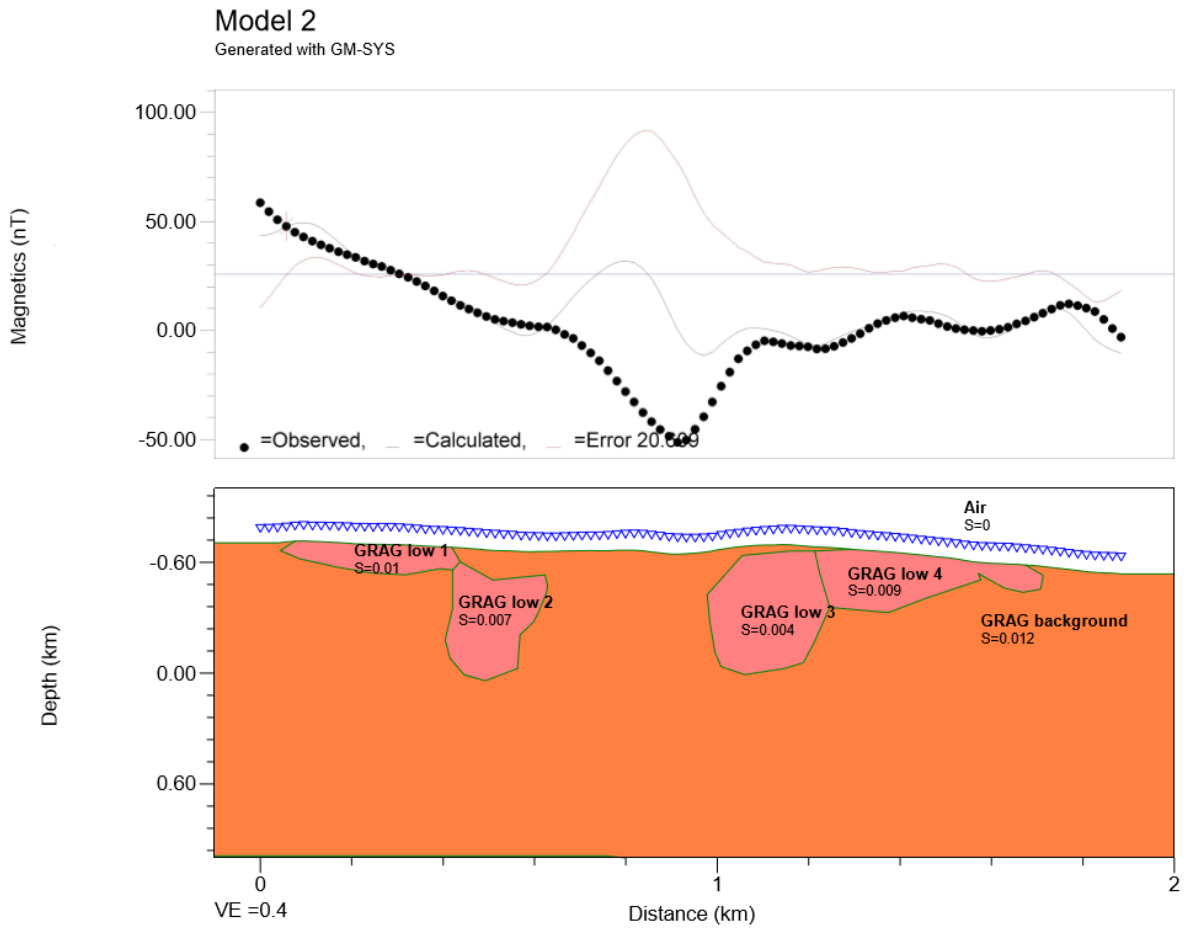

Figure 46. Model 2. Shows areas outside the fault zone with bodies of varying susceptibility (S) to accommodate the varying magnetisation in the granitic gneiss. Susceptibility of the bodies vary from 0.004 to 0.01. Background susceptibility in the granitic gneiss is 0.012 and is based on an average value obtained from field samples. No fault zone is modelled, Model 2 gives a framework for models 3 to 8.

Models 3, 4a, and 4b (Figure 47, Figure 48, Figure 50) investigate scenarios with *deep weathering* as the mechanism for reduced susceptibility and anomalous magnetic response. Based on sample 528, susceptibility values of 0.001 SI are implemented for the weathered zones in models 3 and 4a. This sample was acquired from the surface and has likely been affected by current surface weathering processes in addition to effects of the conceived deep weathering. Thus, the susceptibility of 0.001 SI is an approximation of the susceptibility of in-situ saprolite/deep weathered rock in the deeper parts of the profile. As a sensitivity test, weathered rock of higher susceptibility (0.003 SI) is introduced in Model 4b (Figure 50), to investigate the effect of different susceptibilities on the vertical extent of weathered material in the fault zones.

Two different fault-zone geometries are presented in models 3 and 4a. Model 3 (Figure 47) presents a scenario in which a single fault accounts for the magnetic anomaly associated with the Fisarbakken lineament, whereas Model 4a (Figure 48, Figure 49) presents a scenario of a fault zone consisting of a series of faults across a fault zone of c. 240 m. The width of this zone corresponds well to the 180–250 m wide fracture zone inferred by outcrop observations at locality 49. Although the two models are based on the same principle of deep weathering, the variation in fault zone geometries has a significant impact on the calculated magnetic response. The calculated responses from both Model 3 and 4 correspond very well to the southern (right) "shoulder" of the anomaly. On the northern (left) "shoulder", however, the response from Model 4a corresponds much better than that of Model 3. Model 3 produces a magnetic response with a trough that is much narrower than that of the measured anomalous response. This effect is also reflected in the total error quantified in GM-SYS (Figure 47, Figure 48); 14 nT in Model 3 and 7 nT in Model 4a. Both in terms of the modelled magnetic response *and* the geologic outcrop observations, the fault zone geometry of Model 4a is more probable than that of Model 3. The sensitivity test in Model 4b (Figure 50) is therefore based on this fault zone geometry.

The modelled weathering-profiles in Model 3 and 4a extend to a depth of c. 250 m. This depth is determined by the point at which the minima of the calculated response coincide with the minima on the measured response. Below this depth, the fault is assumed to be unaffected by deep weathering or any other susceptibility-reducing mechanisms, and a susceptibility of 0.012 is utilized. As a sensitivity test, Model 4b introduces a susceptibility of 0.003 SI to the weathered material which results in a greater weathering depth of c. 700 m (Figure 50).

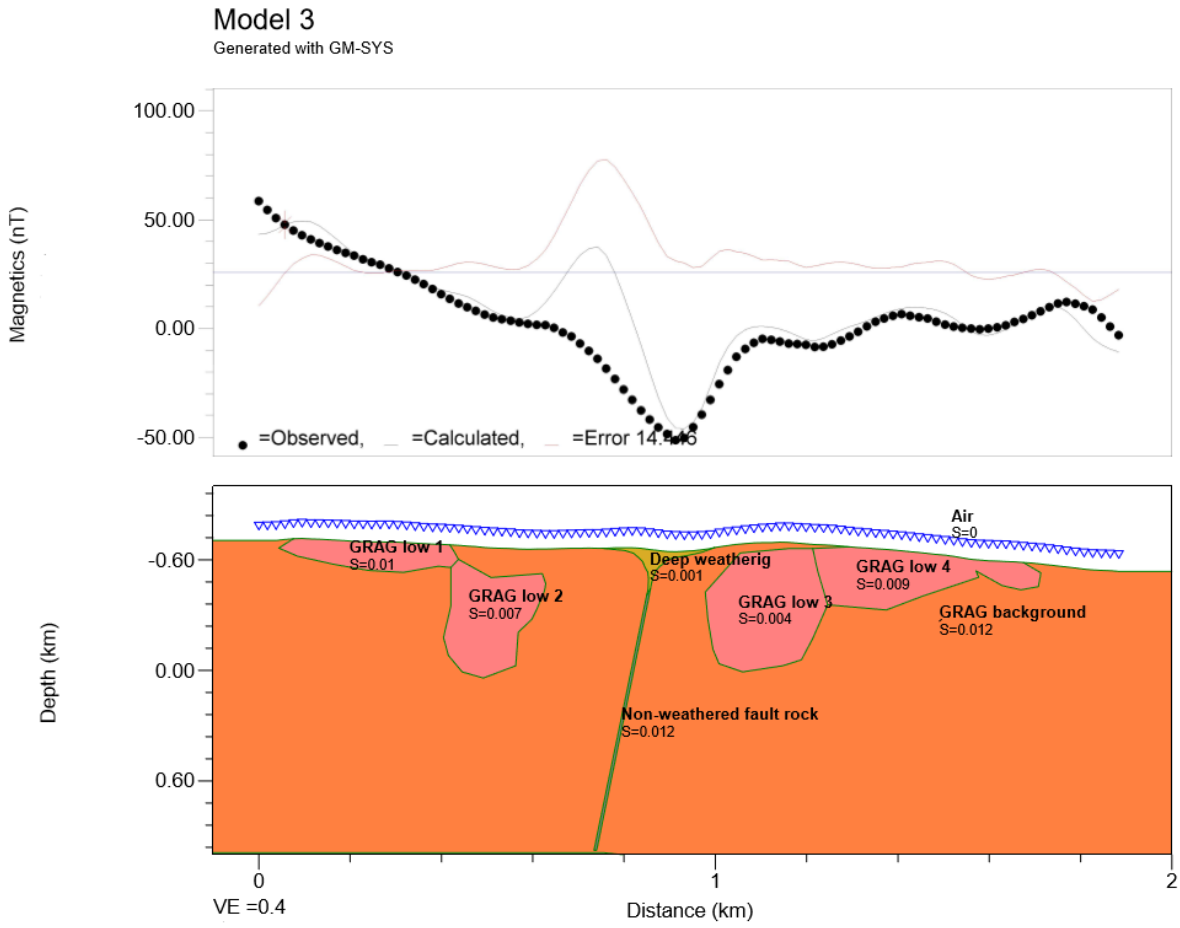

Figure 47. Model 3. Single fault with deep weathering down to a depth c. 250 m below the surface. Below this the fault is assumed to be sealed and no weathering to have occurred. The width of the weathering at the surface is c. 200 m and gradually narrows down to a depth of c. 250 m.

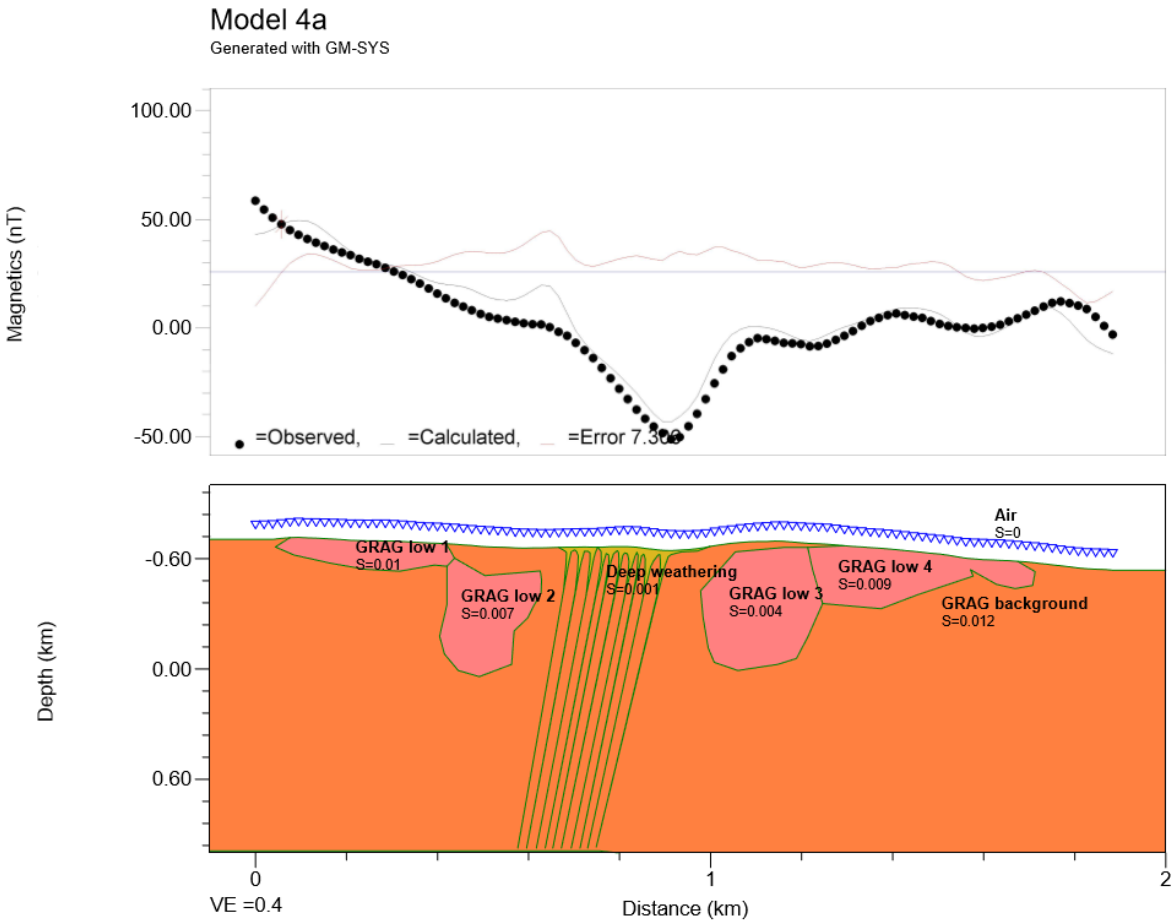

Figure 48. Model 4a. A series of faults affected by deep weathering are introduced across the c. 240 m fault zone/fracture zone. Below this the fault is assumed to be sealed and no weathering to have occurred. Alteration zones have a wedge-shaped geometry - wide close to the surface, gradually narrowing and stopping at c. 250 m below the surface.

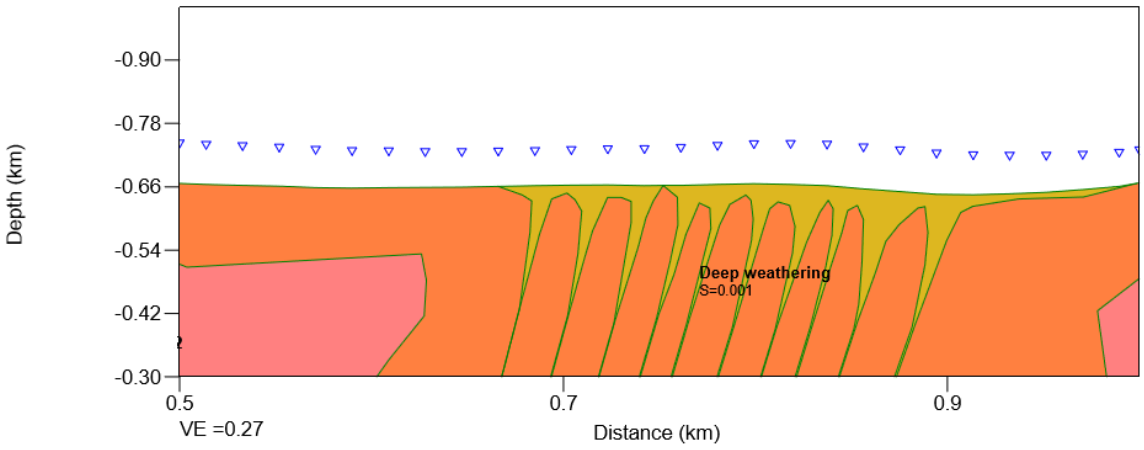

Figure 49. Detailed illustration of the deep weathering profiles along the faults in Model 4a (Figure 48).

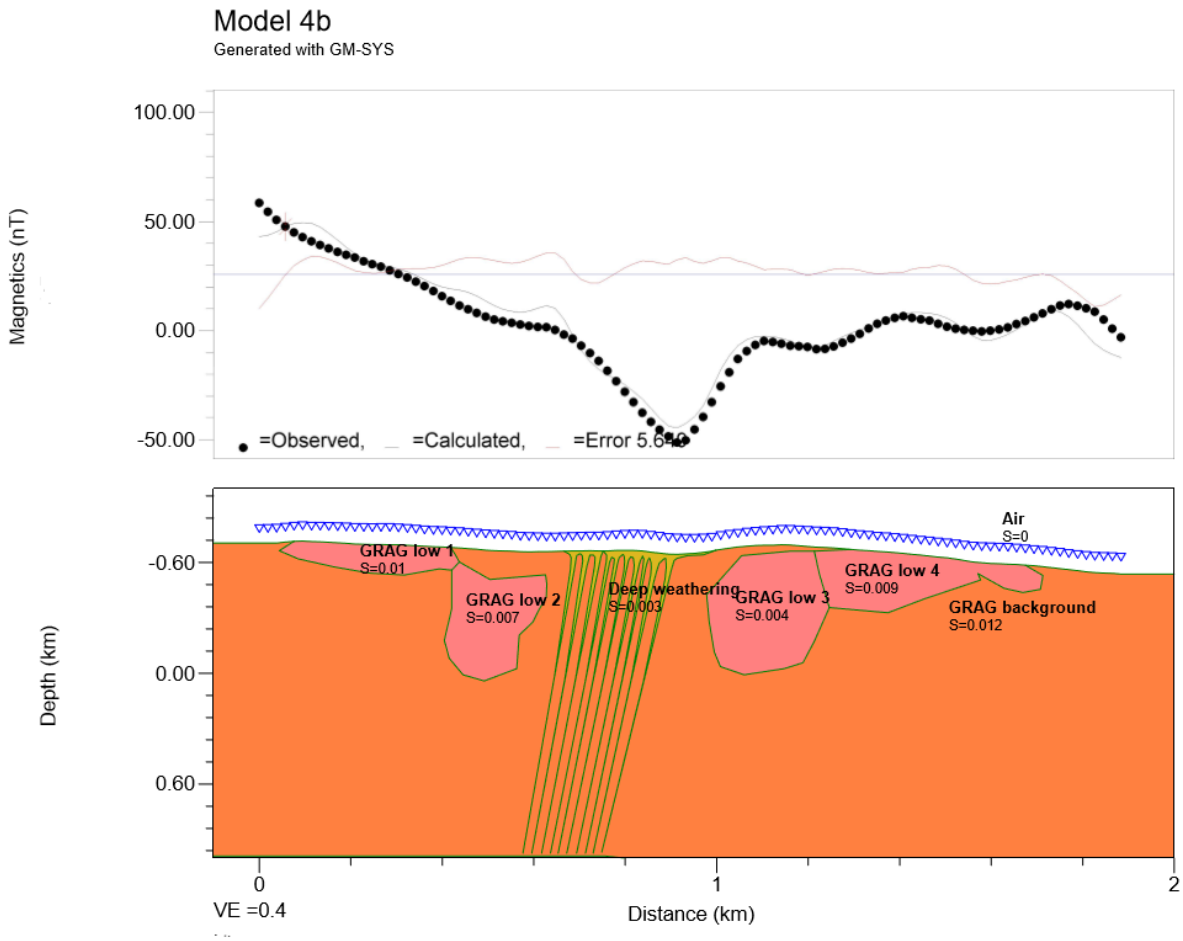

Figure 50. Model 4b - for sensitivity analysis. Susceptibility of deep weathering material increased to 0.003 SI. Similar fault zone geometry to Model 4a (Figure 48) is used, but vertical extent is adjusted to accommodate for increased susceptibility. Depth of weathering is c. 700 m below the surface.

Models 5 and 6 (Figure 51 and Figure 52) investigate scenarios in which *hydrothermal alteration* is the mechanism for reducing the susceptibility and the magnetic response across the Fisarbakken lineament. Based on the assumption that the effect of hydrothermal alteration is greater at deeper levels in the crust, both models incorporate alteration zones with wedge-shaped profiles that narrow towards the surface. In these models, the hydrothermal alteration extends to the current topographic surface. Note, however, that the alteration zones are very narrow at shallow depths, and therefore do not contribute much to the overall reduction in magnetization across the fault zone. Erosion and exhumation also need to be considered in these scenarios. Assuming an exhumation between 750 m and 1750 m (discussed further in section 5.4.1), the hydrothermal alteration, as conceptualized in these models, would occur at (paleo) crustal depths below 750–1750 m.

Model 5 (Figure 51) assumes a scenario in which the anomalous response of the Fisarbakken lineament originates from a single, continuous fault. The calculated response has a large error, and only follows the southern "shoulder" for the upper part of the trough. Despite the wide alteration zone at the base of the profile (c. 100 m), the volume of low susceptibility rock in shallower parts of the profile is simply not enough to mimic the measured magnetic anomaly. Model 6 (Figure 52) is a fault zone scenario affected by hydrothermal alteration. Compared to Model 5, the shape of the calculated response from Model 6 is more representative of the shape of the measured anomaly response. The

minimum of the calculated response is, however, higher than that of the measured, causing a total error of 11 nT. Conclusively, hydrothermal alteration with narrow profiles at shallow crustal levels, regardless of fault architecture, are not very effective in creating a response resembling that of the measured response over the Fisarbakken lineament.

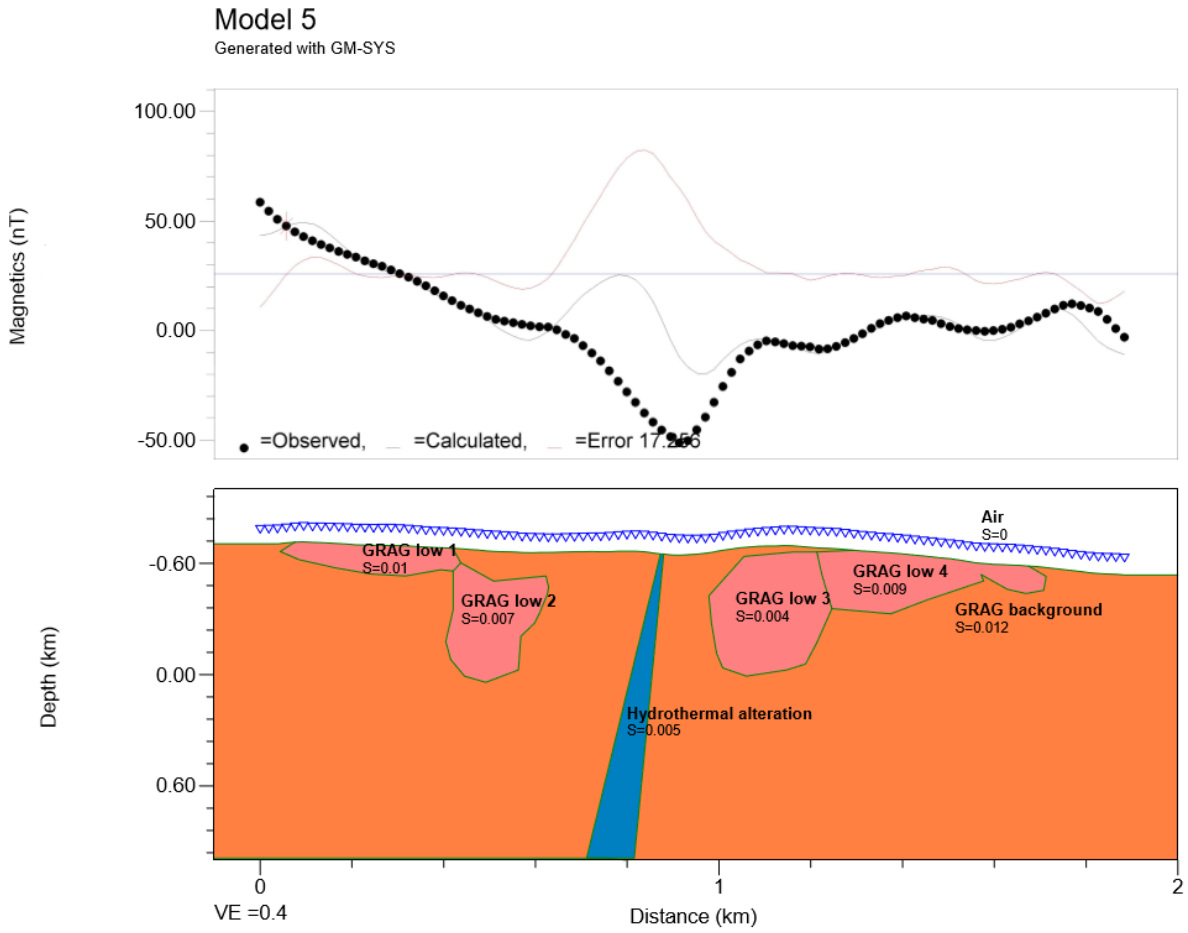

Figure 51. Model 5. Assumes a situation where a single fault affected by hydrothermal alteration has created the anomaly. The model investigates the width that is necessary in the wedge-shape to mimic the response as accurately as possible.

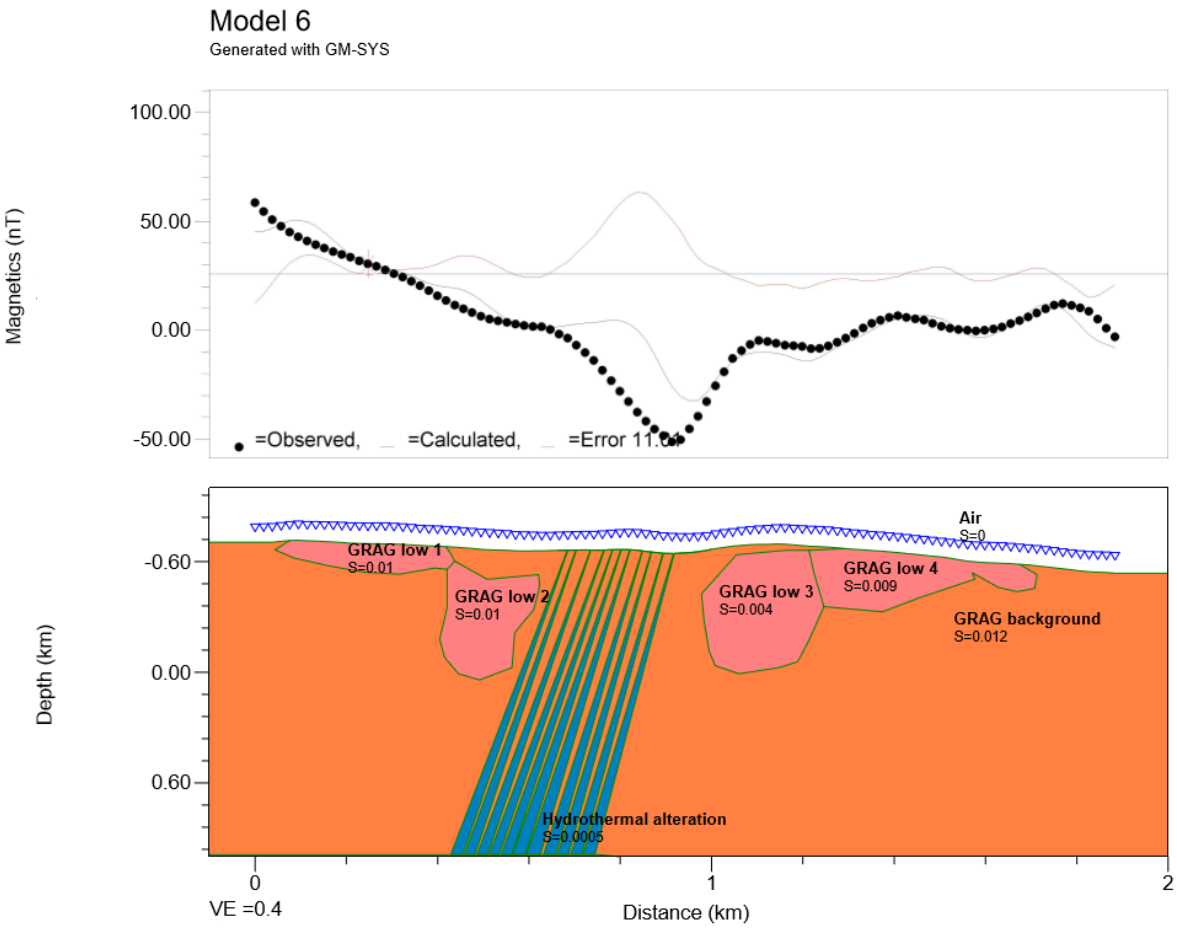

Figure 52. Model 6. A series of faults affected by hydrothermal alteration are introduced across the c. 240 m fault zone/fracture zone. Alteration zones have a wedge-shaped geometry (wide at depth, narrowing towards the surface).

Models 7 and 8 (Figure 53 and Figure 55) present faults with a constant width regardless of the depth. This fault geometry is representative of a combination of hydrothermal alteration and deep weathering. Assuming that these two mechanisms produce near opposite geometries, the hydrothermal alteration will be significant at great depths, while the deep weathering will be significant at shallower depths. Theoretically, this could create a zone of reduced susceptibility of (more or less) constant width as illustrated in Figure 54. Model 7 (Figure 53) assumes a scenario with a single fault whereas Model 8 (Figure 55) assumes a scenario with a fault zone extending 180 m across the Fisarbakken lineament. Again, the fault-zone scenario (Model 8) produces a calculated response that mimics the observed response much better than the singe-fault scenario (Model 7).

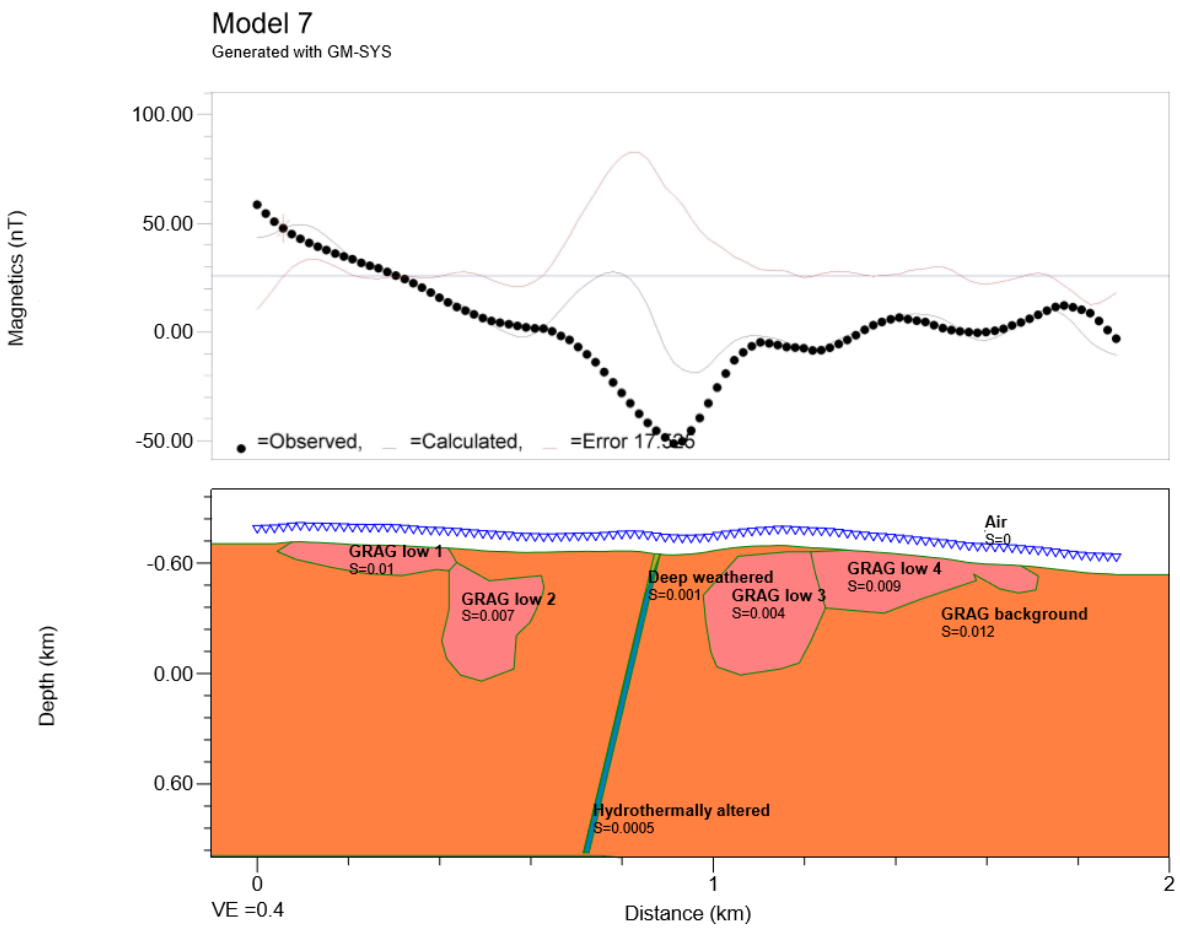

Figure 53. Model 7. Assuming a single fault with a constant width of reduced susceptibility either due to hydrothermal alteration or deep weathering or a combination. The two susceptibility reduction processes have opposite geometries, so a combination causes (more or less) a constant width.

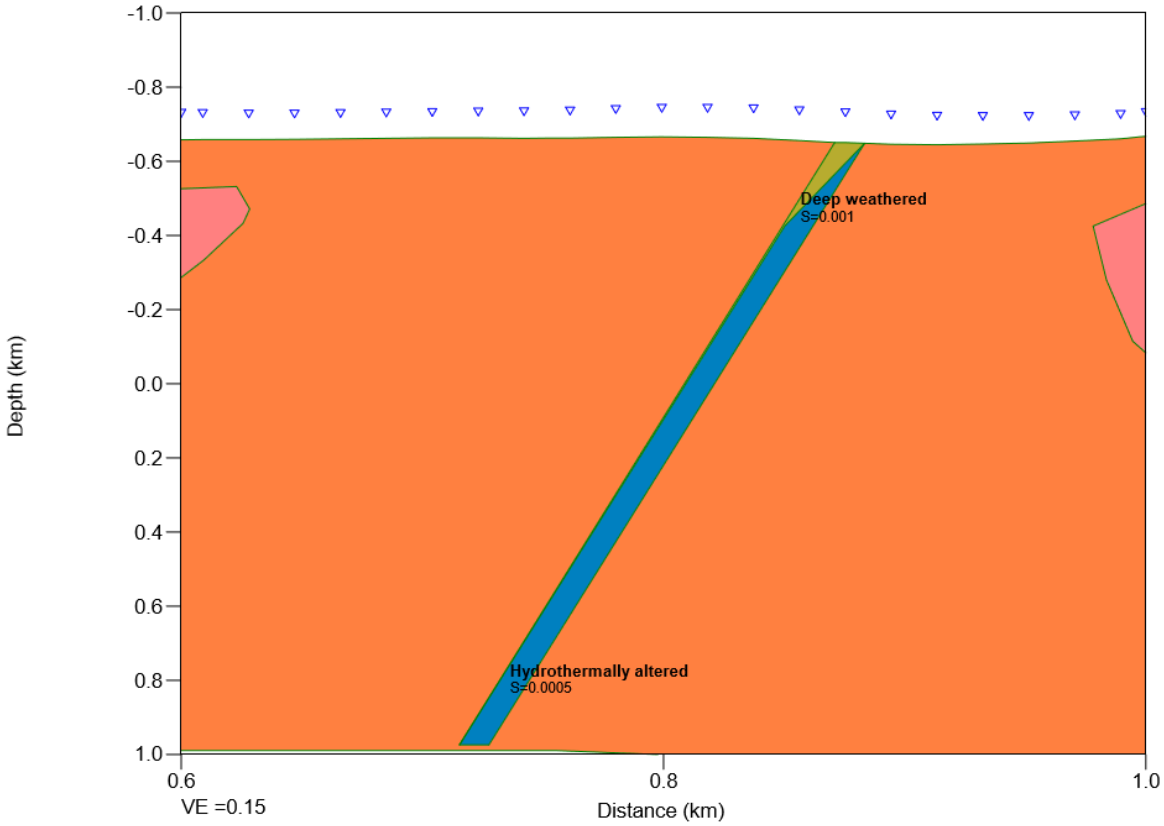

Figure 54. The detailed illustration of the weathered and altered fault in Model 7 (Figure 53), which is also applicable for Model 8 (Figure 55). Provides a conceptualization of combining geometries of deep weathering and hydrothermal alteration to give one zone of reduced susceptibility that has a constant width. The deep weathering extends c. 250 m below the surface.

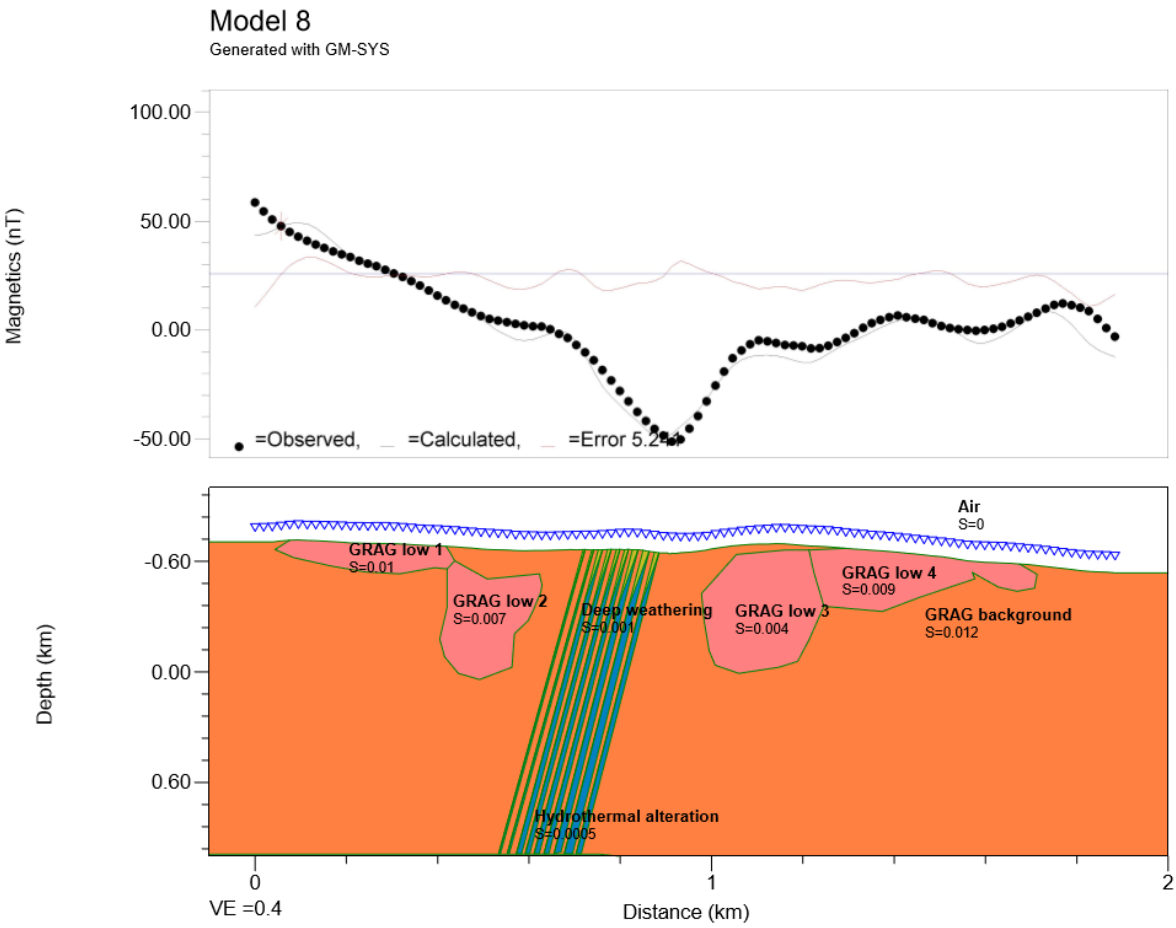

Figure 55. Model 8. A series of faults across a 180 m fault zone with a constant width and affected by a combination of hydrothermal alteration and deep weathering. The two susceptibility reduction processes have opposite geometries, so a combination causes (more or less) a constant width. This model gives the best fit of the calculated to the measured response.

5. DISCUSSION

5.1 Comparison of lineament trends and fault trends

A combined analysis of the results from the lineament study based on remote sensing covering the entire study area *and* the results of detailed field-data from selected areas of interest, provides an extensive, yet detailed structural representation of the bedrock in Drangedal and Nome.

Through the lineament study (Hilde Gunleiksrud, 2017), three dominant *lineament populations* were identified: (1) NE–SW, (2) NNW–SSE, and (3) NW–SE. These populations were represented in both the topographic and magnetic datasets. Analysis of fault planes measured in the field led to the identification of three *fault populations*: (1) NE–SW striking normal faults, (2) NE–SW striking dextral strike-slip faults, and (3) NW–SE striking oblique normal faults. Figure 56 provides a comparison of the strike-orientations of topographic and magnetic lineaments identified through remote sensing (Figure 56A–C) and fault plane strike-orientations identified and measured in field (Figure 56D). A greater variation in orientation is observed for the field measurements relative to the remote sensing measurements. This is likely a result mainly from: a) statistically fewer measurements, and b) small-scale variations in orientation (such as undulation of planes, presence of secondary fractures etc.). These variations are detected at the outcrop-scale but not at the remote-sensing scale. Overall, the two main NW–SE and NE–SW striking populations can be recognised in both studies.

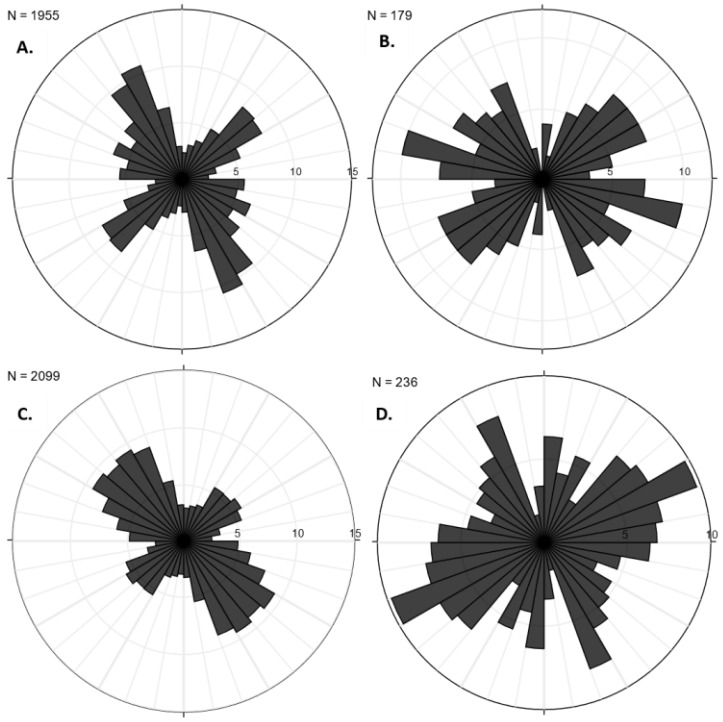

Figure 56. Rose diagrams constructed based on lineament and fault strikes identified in the study area of Drangedal and Nome. A.) Topographic lineaments identified at the 1:50 000 scale with a hillshade illumination from 315°, B.) Magnetic lineaments identified at the 1:250 000 scale, C.) Topographic lineaments identified at the 1:10 000 scale with a hillshade illumination from 315°, D.) Fault planes measured in field. A. and B. are acquired from the entire study region of Drangedal and Nome, C. and D. are collected around roads Rv38, Fv109 and Fv302, in the central region of Drangedal and Nome (Figure 9 and Figure 14).

For a more precise investigation of the correspondence between remote sensing and field data, the structural measurements are compared to the 1:10 000-scale lineament interpretation. These two datasets are acquired from the same geographical area (Figure 14), so a comparative analysis provides a good indication of how the results from field data and remote sensing data correspond. The stereo nets in Figure 56C and Figure 56D provides a comparison of the two datasets. Two prominent peaks can be identified in both rose diagrams – one of NW–SE strike and one of NE–SW strike – generally indicating a good correspondence. This correspondence indicates that; a) the remote sensing is effective in identifying brittle features, and b) the field data provides a

representative description of the general trends in the area covered by the 1:10 000 lineament interpretation (Figure 14). Accordingly, the system of 257 fault measurements (from field work) can be related to the larger system of 2099 lineaments, thereby strengthening the statistical basis and validity of the field results. Coinciding trends in the 1:10 000 (Figure 56C) and the 1:50 000 lineament interpretations (Figure 56A) imply a similarity of structural trends in the mapped area (Figure 14) to the entire study area of Drangedal and Nome. It is therefore reasonable to assume that results based on the structural field data are representative for the entire area of Drangedal and Nome.

The magnitude of peaks in the rose diagrams give an apparent indication of how frequent certain strike orientations occur relative to one another within the studied area. However, care must be taken when determining frequencies based on these peaks. Figure 56D shows the relative frequencies within the measured field data, which is *not necessarily* analogous to the relative frequencies of *all* structures within the entire study area. The field data portrays a higher frequency of faults exhibiting a NE–SW strike than a NW–SE strike (Figure 56D). This relationship contradicts results from the lineament study, in which the frequency of NW–SE lineaments dominates (Figure 56A,C). During field work, a higher frequency of faults and fractures were observed in the granitic gneiss and amphibolitic rocks than in the granitic rocks. As a result, more time was spent taking measurements at outcrops of amphibolites and granitic gneiss, likely causing an overrepresentation of these measurements. Moreover, outcrops of the granitic gneiss and amphibolite were more frequent within the mapped area than outcrops of granite (Figure 14). With these premises, it is hardly a surprise that the NE–SW-striking faults of the amphibolites and granitic gneisses dominate the field data. The 1:250 000 and 1:50 000 lineament interpretations cover the entire Drangedal and Nome municipalities (Figure 11), thus encompassing lineament trends throughout the entire area. It therefore seems likely that the results from the lineament study should represent the relative frequencies of the faults and lineaments more accurately. However, lineaments which appear to be split into shorter segments, will be identified as individual, shorter lineaments and therefore be overrepresented in frequency relative to long and continuous lineaments. This effect may also create a false representation of frequencies in the dataset. By applying a length-normalization to the lineament data, this effect can be avoided. Being aware of the circumstances under which the data is collected and the associated implications, is crucial when analysing the data. Nevertheless, care should generally be taken when using both field data and remote sensing data to assess the relative frequencies of lineament- and fault-populations.

Remote sensing results are limited in the sense that they only represent the expression of the structures in the surface of the bedrock and lack fault-slip data necessary to further classify the faults. Thus, allocating lineament populations to paleo-tectonic regimes is a challenge and requires supplements of field data. Field data obtained after the completion of the lineament study provides the necessary data to further constrain the brittle structures and reconstruct a more precise model for the brittle evolution of the bedrock in Drangedal and Nome. A proposed deformational history is presented and discussed further in section 5.3.3.

5.2 Paleo-stress analysis

A reconstruction of paleo stress-regimes by an inversion of fault-slip data is a great tool in unravelling the evolution of bedrock fracture patterns. The method applied in the analysis should be adapted in terms of the aims of the analysis and the available data in a study. However, the choice of method can have significant implications on the results

of the paleo-stress inversion. Therefore, it is important to carefully consider the methodology and be aware of its implications on the final results.

In this study, the paleo-stress analysis is based on fourteen key localities. Although the key localities are carefully selected to not obliterate significant structural trends, it is important to review the final results in terms of the entire field database.

The following sections describe the role of *structural data, fault plane mineralization* of the fault sets and *angular deviation* in the paleo-stress analysis.

5.2.1 Structural data

In this study, the orientation and kinematics of the fault data are used as constraints in defining the sub-sets included in the paleo-stress analysis. Other constraining data can also be used in defining the sub-sets, for instance fault plane mineralization (further described in 5.2.2), or in some cases lithological or geographical domain. Sorting the data in terms or lithological or geographical domain may be meaningful in situations where a certain domain contains specific structural features which vary distinctly from the surrounding domains. In this study, however, many structural trends occur repeatedly in all three main lithologies. Also, structural features of varying tectonic origin co-exist within the lithological domains. A sorting based on lithological domain is therefore not regarded as relevant.

The constraining data need to be capable of separating the fault-slip datums into geologically meaningful sub-sets. Which data is best suited for this varies from study to study. The quantity and quality of available data in a study is of great significance when constraining and sorting the fault data. The constraining data should ideally be represented in the majority of the recorded faults and should be of a sufficient quality in order to produce valid results. The field-work for this study focused on identifying and recording structural features like fault plane orientation, lineations and kinematic indicators. Thin section analysis also focused on identifying microstructures that would confirm or contradict the field measurements – especially the kinematics measured in field, which were often uncertain. A total of 258 fault measurements, many of which are described in detail with for instance sense of slip and kinematic indicators, provides a large structural dataset of good quality. These structural observations are regarded as a good constraint for sorting the data.

A comparison of fault strike of the key localities (used in the paleo-stress inversion) and the strike of all faults of the field database is provided by the rose diagrams in Figure 18. NE–SW and NW–SE-striking faults dominate in the two rose diagrams, thereby implying a proper representation of the entire field database in the key localities.

5.2.2 Fault plane mineralization

Analysis and identification of fault plane mineralization and character is conducted in field and by microscopy (optic and SEM). Table 3 summarizes and compares various observations regarding mineralization and surface character associated to each fault population set. Recall that the fault population sets are based only on fourteen localities. To relate these mineralization data to the entire study area, the right column of Table 3 provides rose diagrams of fault strike (based on the entire field database) sorted in terms of mineralization. For instance, since fault planes of Set 2 are characterized by a cataclastic and chloritic mineralization, rose diagrams of faults (of the entire dataset) with cataclastic and chloritic mineralization are introduced as a comparison.

	Win-Tensor plot	Observed fault plane mineralization/ character		Fault plane orientation sorted by surface mineralization/ character – from ENTIRE field database
		Field	*Microscopy*	
Set 1	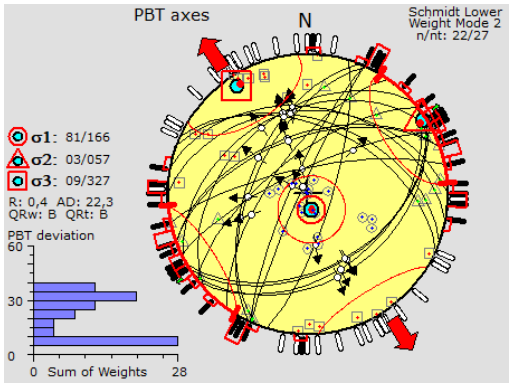	- Chloritic (light to dark green) - Grooved (small-scale corrugation) - Light coloured mineralization on tensile joints	*SEM:* - Chlorite - Cataclasite - (Zircons) - (Apatite) *Thin section (optic):* - Chlorite - Cataclasite	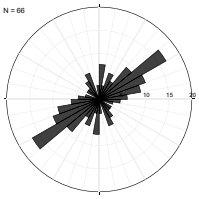 Chloritic 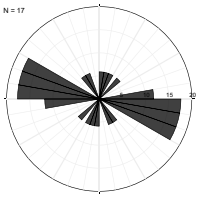 Grooved
Set 2	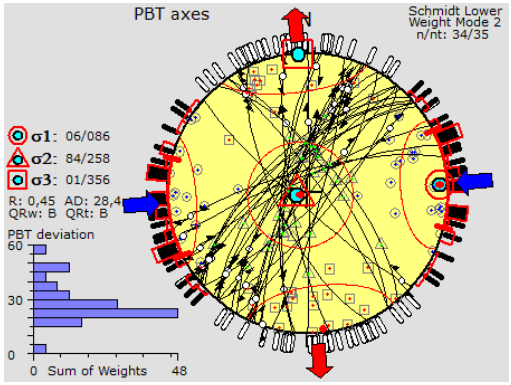	- Cataclastic (thin zone), highly polished - Chloritic (light green to dark green)	*SEM:* - Chlorite - Cataclasite - Amphibole - Pyroxene - (Zircons) - (Apatite) *Thin section (optic):* - Chlorite - Cataclasite	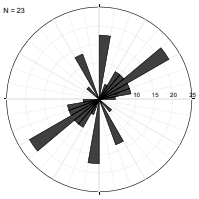 Cataclastic 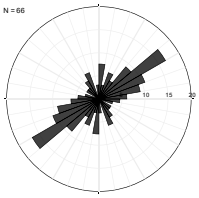 Chloritic
Set 3	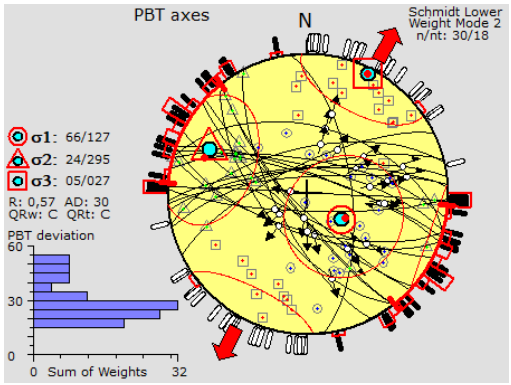	- Light coloured (interpreted as quartz and calcite) mineralization - Calcite identified with acid	*SEM:* - Quartz - Allanite *Thin section (optic):* - Calcite - Quartz	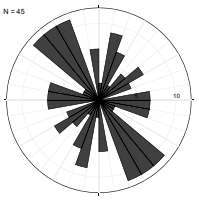 Light coloured minerals

Table 3. Mineralization associated with the three fault sets, given by field observations and microscopy observations. Fault planes from entire field database are differentiated with respect to fault plane mineralization/character and are related to the sets by corresponding mineralization/character.

The rose diagram for chloritic mineralization (Table 3) gives a very prominent NE–SW fault orientation, corresponding to the overall NE–SW orientation of Set 1 faulting. Observations of grooved fault planes are associated to WNW–ESE fault planes, as illustrated by rose diagram in Table 3. This orientation can be associated to a minor

WNW–ESE-trend of Set 1. Grooved structures were in fact observed at some localities (e.g. Locality 2, sub-set 2,0 in Appendix 1), again suggesting a good correspondence between Set 1 and the entire field database. Although these correspondences are expected (after all, the measurements from Set 1 are included in the rose diagram), this confirms that fault plane mineralization trends in the entire field observation database are properly represented in the Set 1. Similar correspondence is confirmed upon comparing Set 2 to the rose diagrams for cataclastic and chloritic fault planes. In fact, the rose diagram for cataclastic fault planes gives a striking resemblance to fault strikes of Set 2. As expected, the overall NE–SW fault strike of Set 2 is well resembled by a prominent peak in the rose diagram. Additionally, well defined peaks of N–S and NNW–SSE strike are also represented in the rose diagram – corresponding very well to internal strike variations of Set 2. The rose diagram of fault planes with a light-coloured mineralization (based on entire field database) displays some variation in strike, but a definitive peak corresponds to the NW–SE strike of faults of Set 3. Again, this correspondence is an indication that the general trends of calcitic and quartzitic fault plane mineralization within the studied area are properly represented in Set 3.

Generally, the fault strike of each set (left column of Table 3) corresponds well to fault strike of the rose diagrams (right column of Table 3). This indicates a proper representation of the fault plane mineralization trends of the entire field database by the three fault sets. Thus, no significant trends (in terms of mineralization) are left out in the paleo-stress regimes reconstructed by inversion of the three fault sets.

Set 1 and 2 contain fault planes of similar mineralogical character. This may not be a surprise considering the correspondence of fault strike. In some cases, as observed at locality 14, the two sets even share a common fault plane accommodating the two sets of slip-lines. The two sets of slip-lines are observed in mineralizations of chlorite and cataclasite. Analysis of thin sections and SEM images confirm these field observations (Figure 29 and Figure 30). Localities where Set 1 faulting is displayed independently from Set 2 provide observations that aid in differentiating the fault plane character of the two sets. Grooves, or small-scale corrugation structures appear on certain fault planes of Set 1. These structures are not observed on fault planes of Set 2. On the contrary, fault planes of Set 2 are generally highly polished. Conclusively, Set 1 fault planes are commonly associated with chlorite mineralization and grooved surfaces, whereas Set 2 faulting is associated with polished cataclasite and some chlorite mineralization. Field observations of Set 3 faults indicate a dominance of light-coloured mineralization. Application of acid to the fault plane identified some areas of calcitic mineralization. An indication of the relative hardness of the mineral, done by scraping with the back of a hammer, assisted in differentiating between calcite and quartz. Analysis of thin sections confirm a calcitic fault plane coating on top of a quartzitic domain (Figure 25). SEM images confirm field observations of quartz mineralization (Figure 26).

Fault plane mineralization can be used as a constraint to sort the fault-slip data prior to conducting a paleo-stress inversion. This requires a characteristic variation of mineralization, that can properly differentiate the data and relate fault sets to individual deformational phases. In this study, the mineralization of Set 1 and 2 is similar, and is generally dominated by chlorite and cataclasite, whereas the Set 3 mineralization is dominated by calcite and quartz. Thus, sorting the data by fault plane mineralization *may* distinguish NE–SW striking faults (Set 1 and 2) from NW–SE striking faults (Set 3), but would likely not properly distinguish Set 1 and 2. This would create heterogenous sets in

terms of fault-slip, and the paleo-stress reconstruction would create a system of geologically meaningless stress regimes.

Mineralogical analysis performed by microscopy analysis (optical and SEM) gives a more precise identification of the mineralization relative to the field-based observations. However, the number of samples collected for microscopy analysis is too low to create a statistically representative base for the entire fault dataset. Constraining the data based on fault plane mineralization may in this study therefore introduce uncertainties associated with; a) incorrect mineral characterisation and b) poor statistical basis. Furthermore, the most common mineral phase observed on the fault planes was chlorite. Authigenic growth of chlorite is associated to a wide range of pressure and temperature conditions (De Caritat et al., 1993), implying fault planes with a chloritic mineralization are not necessarily limited to one deformational setting. This is another reason why the paleo-stress analysis in this study was not based on fault plane mineralization. Although fault plane mineralization was not used as a direct constraint in the paleo-stress analysis, mineralization can assist in constraining features where the structural measurements are ambiguous. For instance; Set 2 and 3 are generally associated with different mineralizations. Therefore, distinguishing the (few) NW–SE striking fault planes of Set 2 from those of Set 3 (Table 1) based on fault plane mineralization, could be of use if kinematic indicators are absent or obscure.

5.2.1 Angular deviation of stress fields

The paleo-stress analysis supports three main stress regimes influencing the brittle deformation of the bedrock in Drangedal and Nome; (1) NW–SE extension, (2) E–W transpression, and (3) NE–SW extension. Altogether, these stress regimes are based on a heterogenous fault-slip dataset, in which each fault-slip datum is (theoretically) associated to a unique stress tensor. These fault-slip datums and associated stress-tensors are further combined in near homogenous datasets, that are assumed to be co-genic. Stress-tensor data can be combined in numerous ways, creating an ambiguous problem when reconstructing the paleo-stress regimes. Within the three suggested stress regimes, the angular deviation of the data did not exceed 30°. During the inversion process, a definite limit for the deviation was not enforced. Instead, the various combinations of data were assessed qualitatively from a kinematic and orientational point of view with the angular deviation serving as additional guidance. However, if a definite limit for the deviation was enforced - either constraining or liberalising the data combinations - this could have significant implications on the final stress regimes, potentially resulting in a different interpretation of the brittle evolution. For instance, enforcing a stricter limit would likely lead to a higher number of paleo-stress regimes, which essentially indicates a more complex brittle evolution. Such a complex evolution may be challenging to defend in a regional-tectonic perspective, but may still be valid. With the approach used in this study, a total of eight sub-sets were 'rejected' from the final paleo-stress inversion, due to a significant deviation from the other data. Enforcing a stricter approach may lead to the rejection of more data from the inversion - potentially disregarding important deformational trends.

5.3 Tectonic evolution

To model the brittle evolution of the bedrock in Drangedal and Nome, the results from the structural analysis, lineament study and paleo-stress analysis are combined and integrated into a synthesis with the regional-tectonic evolution of southern Norway. Based on the structural data, three *fault sets* are determined: Set 1 with NE–SW striking normal faults, Set 2 with NE–SW striking normal-dextral oblique to strike-slip faults, and

Set 3 with NW–SE normal to oblique-slip faults. Through paleo-stress reconstruction of these sets, the following *paleo-stress regimes* were determined: NW–SE extension (Set 1), E–W transpression (Set 2), and NE–SW extension (Set 3).

5.3.1 Fault Set 1, 2 and 3 in a regional-tectonic context

This section discusses the three stress regimes and associated fault sets in terms of their significance in a regional-tectonic context.

5.3.1.1 Set 1

A population of *NE–SW striking normal faults* originating from a *NW–SE extensional regime* make up Set 1 (Table 1). Faults of Set 1 are observed throughout the entire study area and are present in all three lithologies. Despite some variation in strike orientation, the slip direction generally relates well to a NW–SE extension (Table 1). However, some deviation does occur and results in the extensional axis varying from WNW–ESE to N–S. For the most part, deviations in the stress field tensors seem associated to variations in lithologies and their mechanical rock properties. Using slip-datums of mechanically isotropic rock masses (like the granite) to generate paleo-stress fields, may be more accurate than using highly anisotropic and foliated rock masses (like the amphibolites and granitic gneisses). In this case, the orientation of the extensional direction based on the granitic structures and the direction based on the entire fault population of Set 1 coincide nearly perfectly. This strengthens the confidence of the determined orientation of the stress regime generating the fault populations of Set 1. Some of the deviation in stress tensor orientation may arise from a rotation of the stress field associated to a certain deformational period.

On a regional scale, southern Norway has been influenced by numerous periods of rifting and orogenic collapse resulting in NW–SE extension of the crust. The tectonic influence of these periods in the studied area of Drangedal and Nome is discussed in terms of their timing and spatial extent.

At c. 850 Ma the collapse of the overthickened Sveconorwegian orogenic belt initiated a NW–SE regional extension. On the southwestern coast, the NE–SW striking Hunnedalen Dike Swarm intrudes the Precambrian bedrock. The dikes are dated to an igneous event occurring at 850 +/- 59 Ma (Walderhaug et al., 1999), marking the early phase of extension associated to the *Sveconorwegian collapse*. Signs of Sveconorwegian extension are also found closer to Drangedal and Nome. The NE–SW striking Porsgrunn-Kristiansand (P-K) fault zone is located in the very south of the study area and defines the boundary between the Telemarkia and Bamble lithotectonic units (Figure 4). Analysis of gneiss mylonitization by Smalley et. al. (1983) indicates that this zone was active as a sinistral shear zone around 1250 Ma, before being reactivated as a brittle extensional fault at c. 900 Ma (Mulch et al., 2005). This reactivation is likely associated to the Sveconorwegian orogeny and collapse. Similar cases of reactivation of pre-existing shear zones are observed on a regional scale and are related to exhumation and subsequent extension of the Sveconorwegian belt (Piper, 2009).

A mylonite zone in the northern part of the Drangedal area was discovered in 2017 through the BITE project fieldwork by NGU. On the bedrock map in Figure 4, this shear zone (the so-called Nisser shear zone) is located just north of the supracrustals of the Nissedal Complex. This mylonite zone exhibits a similar NE–SW orientation as the P-K fault zone. Due to corresponding orientation and geographic proximity of the two zones, it is reasonable to assume a common origin. Brittle, extensional faults striking NE–SW

have also been observed cutting the Nisser shear zone (Torgersen, pers. comm., 2018), and is likely also in part associated to the Sveconorwegian collapse.

Due to the geographic proximity of the P-K fault zone and the mylonite zone in Drangedal, it is reasonable to assume that post-Sveconorwegian NW–SE extension was influential in the study area and may have caused the faulting in Set 1. The post-Sveconorwegian faulting of the Nisser and P-K zones was, however, a *reactivation* of pre-existing planes of weakness. Field observations show no indications that the faulting in Set 1 occurred as a reactivation - but it cannot be ruled out, as overprinting may eradicate pre-existing signs of slip. Other rock properties, such as foliation, may also act as planes of weakness and can accommodate slip at lower stress-levels than could be expected of mechanically isotropic rocks. Nevertheless, the Sveconorwegian NW–SE extensional regime corresponds perfectly to the NW–SE extensional regime derived from paleo-stress analysis of Set 1. It thus seems probable that Sveconorwegian collapse had a certain influence in the faulting of Set 1.

The Rolvsnes granodiorite exposed at the Bømlo Islands in Sunnhordaland also possesses a series of NE–SW striking extensional faults (Scheiber et al., 2015). These faults are associated to a Devonian NW–SE extension imposed upon the region by the collapse of the Caledonian orogeny, starting at around 400 Ma (Gabrielsen et al., 2010; Scheiber et al., 2015; Valle et al., 2002). The Bømlo Islands are situated more than 200 km north-west of the current study area, much closer to the present-day Caledonides, whereas Drangedal and Nome is located near the margin of the Caledonian front (Figure 5). Consequently, the Devonian extension is assumed to have had a lesser effect in the studied area relative to Bømlo. Nevertheless, it is still possible that the tectonic stress from the distant Caledonian collapse was sufficient to trigger a reactivation of the (assumed) pre-existing NE–SW faults of Set 1. In fact, a Devonian reactivation of the P-K fault zone, close to the study area, can be inferred from bedrock geology maps. Figure 3 and Figure 4 show Silurian lithologies being cross-cut and displaced by the Porsgrunn-Kristiansand fault zone, constraining the apparent reactivation to post-Silurian time (e.g Devonian). This apparent reactivation does not directly imply that NE–SW faults of Set 1 were also reactivated in response to the Caledonian collapse, but presents the possibility – this despite any direct field evidence of a Devonian reactivation in the study area.

A regional extension with periods of localized and extensive rifting began in the early Carboniferous and prevailed until the Cretaceous, creating major rift structures like the Oslo Rift and the Viking Graben in the North Sea (Gabrielsen et al., 2017). The Oslo- and Skagerak Graben systems are part of the *Oslo Rift* and originate from a dominating E–W extension in late Cretaceous until early Triassic (Heeremans & Faleide, 2004). Due to the proximity of both the Oslo- and Skagerak Graben to Drangedal and Nome, it is likely that Carboniferous and Permian extension is relevant also in the brittle deformation of the studied area. In fact, Carboniferous and Permian tectonic activity is associated to the reactivation of several significant Precambrian fault zones, including the P-K fault zone (Neumann et al., 1991) located close to Drangedal. A reactivation of the NE–SW P-K fault zone suggests that a reactivation of (assumed) pre-existing NE–SW faults of Set 1 may also have occurred in association to the Oslo Rift. The parallel orientation of the Set 1 faults to the Skagerak Graben also supports a possible reactivation of Set 1 faults in Carboniferous to Permian time. Note, however, that no direct evidence of reactivation in this time is represented in the field data.

During fieldwork conducted in 2017, the NGU BITE-team sampled a fault gouge from a NE–SW striking fault representative of Set 1 and 2 in terms of fault orientation. An absence of kinematic indicators on the fault planes, leaves the sense of slip unconstrained. K-Ar of illite/muscovite dating of the fault gouge provided an age of c. 220 Ma (Torgersen, pers. comm., 2018). This indicates faulting (possibly by reactivation) in Set 1 occurring in late Triassic. Although the rifting of the Oslo area ceased in early Triassic (Larsen et al., 2008), a regional extension continued into the Cretaceous (Gabrielsen et al., 2017), creating features like the Viking Graben in the North Sea. The rifting of the Viking Graben is associated with two main extensional phases; one of Permian-Triassic age and one of Jurassic age (Færseth et al., 1997). The first rifting phase is poorly constrained, both in the North Sea and elsewhere (Heeremans & Faleide, 2004). Most workers argue that the rifting ceased in early Triassic (Voorde et al., 2000), before a NW–SE extension dominated in the Jurassic (Færseth et al., 1997). A few workers, however, have suggested that an extensional phase prevailed in the late Triassic (Odling, 1992; Voorde et al., 2000). Odling et al. (1992) suggests a rifting phase of significance to the Viking Graben occurring at 220–225 Ma, corresponding well to the dated gouge (c. 220 Ma) from the BITE project. The direction of extension associated to late Triassic rifting is poorly described. Based on the general rotation of the regional stress field from E–W extension in the Carboniferous-Jurassic to NW–SE extension in the Jurassic-Cretaceous, it may be assumed that late Triassic extension was oriented within this sector (perhaps closer to NW–SE extension, due to the relative proximity in time to the Jurassic). Considering an assumed WNW–ESE to NW–SE extension in the late Triassic *and* field-based evidence for faulting in NE–SW faults at c. 220 Ma, it seems likely that Set 1 faulting is associated with this regional tectonic event - perhaps as a reactivation. In the case of a WNW–ESE to NW–SE extension, the NE–SW faults were reactivated at (sub-)optimal orientation to create dip-slip faulting. Note, however, that the tectonic stress regime in late Triassic is poorly constrained. As a result, other stress field orientations may have caused reactivation at an un-optimal orientation.

5.3.1.2 Set 2

Set 2 is dominated by *NE–SW striking faults* with *dextral-oblique slip*, along with some conjugate NW–SE striking sinistral faults, altogether constraining an *E–W transpressive* regime (Table 1). This set is recognised in all three lithologies, but significantly less so in the granites. Coinciding foliation and fault plane orientation indicate that, especially in the amphibolites, the faulting in Set 2 was strongly influenced by pre-existing planes of weakness.

Southern Norway has been subject to one *major* tectonic regime characterised by E–W compression; the *Caledonian orogeny*. The Caledonian orogeny was active between c. 505 and 400 Ma (Bingen & Solli, 2009) and is generally associated with NW–SE compression. However, it has been suggested based on thrust ramp orientations in southern Norway, that the compressional axis rotated from an eastern-, through south-eastern-, to a southern orientation throughout the orogeny (Hossack & Cooper, 1986; Morley, 1983). The E–W compression is suggested to correspond to an early thrusting phase (Hossack & Cooper, 1986), namely around 450 Ma. Relating this phase of Caledonian compression to the current study gives the faulting in Set 2 an assumed age of c. 450 Ma. The maximum reach of the Caledonian front is interpreted to have been close to the study area of Drangedal and Nome (Figure 5). The distal position to the main paleo-orogenic activity, suggests that the Caledonian compression may not have been of major tectonic influence in Drangedal and Nome. Likely, the impact was not capable of generating new faults and fractures, which is why Set 2 is almost exclusively developed

as reactivation of pre-existing foliation planes in the amphibolites. This assumption is also supported by the overall lack of N–S to NE–SW striking reverse faults. At locality 59, one NE–SW striking fault with clear reverse dip-slip indicators was observed (sub-set 59,3 in Appendix 1). If associated to Caledonian compression, the fault observed at locality 59 is likely of a slightly younger origin than Set 2, when the stress field had rotated from an E–W compression to a NW–SE compression. However, this fault alone does not provide a statistical base strong enough to confirm Caledonian nucleation of new faults. Caledonian reactivation of pre-existing planes of weakness, such as fractures and faults, is more probable and has stronger support in the structural data.

The *Listafjorden-Drangedal Fault* is a NE–SW striking fault zone characterized by a strong topographic lineament and in parts by a faint aeromagnetic lineament (Gabrielsen et al., 2017). The lineament can be traced for 170 km from Fedafjorden in the western part towards Drangedal in the eastern part (Gabrielsen et al., 2002; Gabrielsen et al., 2017). Based on cross-cutting relations observed in topographic data and lithological displacement on bedrock maps (Figure 57) (Falkum, 1982), Gabrielsen (2017) suggests a dextral sense of displacement in the western segment of the Listafjorden-Drangedal Fault. These observations by Gabrielsen (2017) provide large scale structural indications that dextral slip along NE–SW striking features has occurred in southern Norway. Although no time of faulting is suggested, the general lack of E–W compressional dextral features in southern Norway makes it reasonable to relate the faulting of the Listafjorden-Drangedal Fault to Set 2 in this study.

The coinciding strike orientation of Set 1 and 2, makes it reasonable to consider any post-Caledonian reactivations of Set 1 as possible reactivations of Set 2 as well. As discussed for Set 1, NE–SW faults *may* have been reactivated in an extensional regime associated to the Caledonian collapse and were *likely* reactivated in a late Triassic regional extension (c. 220 Ma based on dated fault gouge). See section 5.3.1.1 for more details on these potential reactivations.

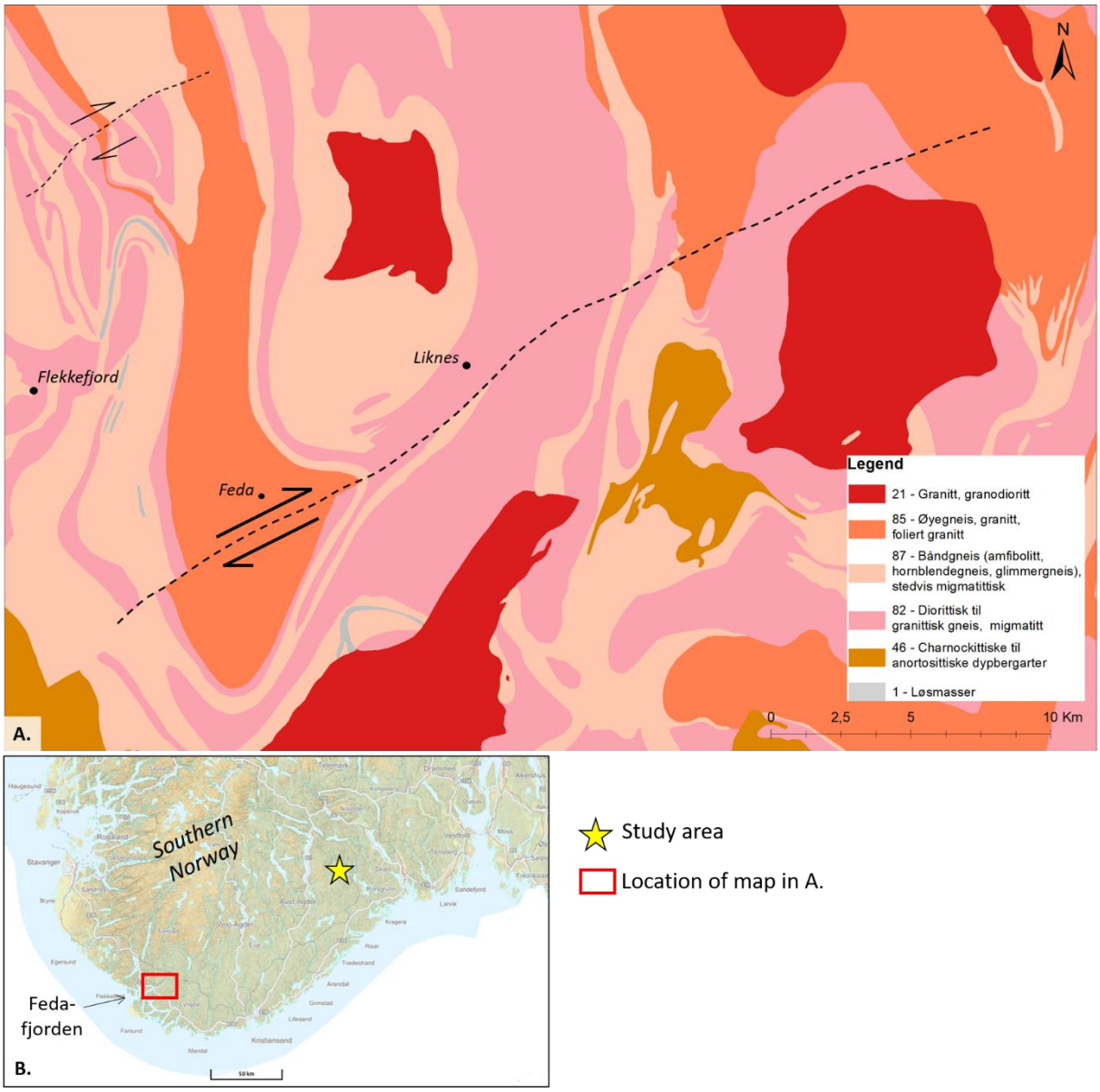

Figure 57. A.) Bedrock map of the western segment of the NE–SW striking Listafjorden-Drangedal fault. Offset of the lithologies indicate a dextral offset sense of faulting. B.) Geographic location of the bedrock map in A, modified from (Kartverket, 2018).

5.3.1.3 Set 3

A fault population of dominantly NW–SE striking faults make up Set 3 (Table 1). The faulting is characterized by normal to dextral-oblique slip caused by an overall NE–SW extensional regime of non-Andersonian conditions. Some deviation occurs within strike-orientation and slip-direction. If assuming Set 3 to be a reactivation of a pre-existing fault- and/or fracture-system, this deviation can be explained by a variation in orientation of the faults or fractures that were reactivated.

A NE–SW extensional regime of regional tectonic significance is the rifting between Laurentia and Baltica associated to the break-up of the supercontinent Rodinia. This rifting began in the late Proterozoic, around 610 Ma, and initiated a series of magmatic intrusions, such as the basaltic Egersund dike swarm situated in the westernmost part of the Telemarkia lithotectonic unit (Bingen et al., 1998). The Egersund dike swarm is dated to 616 +/- 3 Ma and exhibits a WNW–ESE orientation (Bingen et al., 1998). Since the

dikes have not been deformed after intrusion, their orientation is significant and indicates a NNE–SSW extensional regime triggering their emplacement (Bingen et al., 1998). A milder extension continued after the initial rifting between Baltica and Laurentia, but with greater influence further east towards central Baltica (Bingen et al., 1998; Meert et al., 1998). Carbonatic complexes such as the Fen complex were accommodated in this period of mild extension. The Fen complex intruded the Sveconorwegian gneisses at c. 580 Ma (Bingen et al., 1998; Meert et al., 1998), and is located in the Telemarkia lithotectonic unit, in the northeastern part of the study area (Figure 3 and Figure 4). Due to this proximity, it can be assumed with a fair amount of certainty that the extensional regime in which the Fen complex originated, was also of influence in Drangedal and Nome. Whether this mild extension associated to the emplacement of the Fen complex caused the faulting of Set 3, or if this faulting is rather a result of the earlier NNE–SSW extension in which the Egersund dikes were created, is uncertain.

Further west, in Sunnhordaland, a population of NNW–SSE striking lineaments have been investigated (Valle et al., 2002). Their exact origin is unclear, but it has been suggested that they might be related to a period of ENE–WSW extension in the Late Permian to Early Jurassic (Valle et al., 2002). Evidence suggesting such an extensional regime is observed on the western margin of the North Sea towards Great Britain, related to the rifting of the Viking Graben (Valle et al., 2002). Extension and rifting further east in southern Norway (like the Oslo Rift) is also recorded within the same time period, but terminated somewhat earlier (early Triassic). It is therefore not unlikely that the late Permian to early Triassic NE–SW extension also affected the Drangedal area and may have caused a reactivation of Set 3 faults.

Regardless of which regional extension caused the faulting of Set 3, the (dominantly) oblique slip is likely a reactivation of a pre-existing fracture system. Thus, NW–SE fracture systems with origins pre-dating the breakup of Rodina are investigated. Gabrielsen et al. (2002) describes a population of lineaments of a NW–SE orientation that are of regional significance and nearly evenly distributed throughout Norway, except for within the Oslo rift-zone and the Møre-Trøndelag Fault Complex. The lineaments of this population represent extensive fractures in the Fennoscandian Shield and are suggested to have a Pre-Svecofennian origin associated to the Gothian orogeny (R.H. Gabrielsen et al., 2002). These fractures pre-date an assumed late Proterozoic (rifting of Rodinia) origin of Set 3, and can accordingly be suggested as a suitable system of pre-existing planes of weakness that may have been reactivated in response to a NE–SW extension sometime between 610 and 580 Ma.

5.3.2 Temporal relationships

Both Set 1 and 2 are dominated by NE–SW striking faults, however, the two sets are associated to different deformational regimes. Thus, a simultaneous origin is not possible. Using field observations, a temporal relationship is suggested. Fault planes in Set 2 resemble a selection of the steep, NE–SW striking fault planes in Set 1. In fact, at locality 14, slip-lines representative of both Set 1 and 2 are observed on the same fault plane (Figure 28 and Figure 29). The two sets of lineation occur throughout the fault planes of locality 14, with the dextral-oblique slip-lines of Set 2 appearing to overprint the normal slip-lines of Set 1. Assuming this relationship to apply in general for Set 1 and 2, infers an earlier Set 1 faulting than that of Set 2. Such a temporal relationship may indicate that faulting in Set 1 *generated* the faults, whereas the faulting in Set 2 was a *reactivation* of the pre-existing fault planes of Set 1. Note, however, that not all fault planes observed in Set 2 are indicative of reactivation, and only certain fault planes in

Set 1 are overprinted by Set 2 faulting. It is indeed possible that faulting in Set 2 also generated new faults or exploited *other* pre-existing planes of weakness, in addition to the reactivation of certain faults of Set 1. Nevertheless, faulting in Set 2 is interpreted to post-date faulting in Set 1, with Set 2 representing a reactivation of steep NE–SW fault planes of Set 1.

Both field data and remote sensing data can be effective in discovering cross-cutting relationships between fault populations. Unfortunately, the field data does not provide any clear indications of cross-cutting relationships between fault populations. Through the lineament study (Hilde Gunleiksrud, 2017) signs of cross-cutting relationships were observed in both the magnetic data and the topographic data. In the magnetic data, lineaments with a NE–SW strike appeared to cross-cut those of a NW–SE strike (Figure 58A). Relating this observation to the structural data, implies a cross-cutting of Set 3 by Set 1 and 2. Concluding a temporal relationship based on the apparent cross-cutting of magnetic data is, however, problematic due to the data's sensitivity to subsurface properties. A fault or other magnetic contrast deep vertical extent will produce a stronger anomaly than one with a shallower extent, resulting in an apparent cross-cutting of the shallow fault by the deep fault. Cross-cutting relationships are also observed in the topographic lineaments – these provide more valid relationships to use in unravelling temporal relationships. Generally, NE–SW striking lineaments appear to cross-cut NW–SE striking lineaments (Figure 58B–C). Again, relating these observations to the structural data, implies a cross-cutting of Set 3 by NE–SW faults of Set 1 and 2. This cross-cutting relationship(s) infers that NE–SW striking faults of Set 1 and/or Set 2 post-date faulting in Set 3.

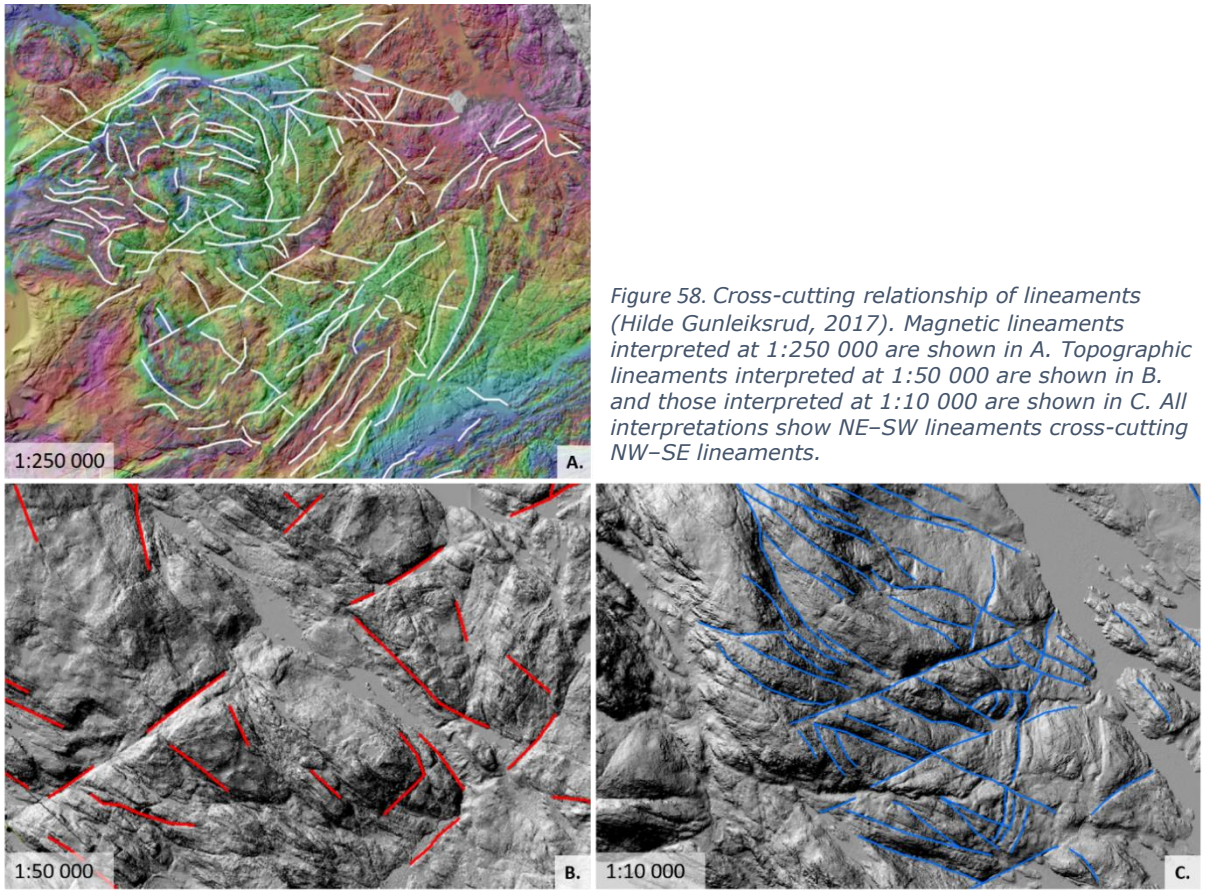

Figure 58. Cross-cutting relationship of lineaments (Hilde Gunleiksrud, 2017). Magnetic lineaments interpreted at 1:250 000 are shown in A. Topographic lineaments interpreted at 1:50 000 are shown in B. and those interpreted at 1:10 000 are shown in C. All interpretations show NE–SW lineaments cross-cutting NW–SE lineaments.

5.3.3 Proposed brittle structural evolution of the Drangedal-Nome area

Based on the known tectonic events that have affected southern Norway and on the inter-set relationships given from overprinting of fault plane lineations and cross-cutting of lineaments, the following temporal relationship between the three sets is inferred; *Set 1 pre-dates Set 2* and *Set 3 pre-dates Set 1 and/or Set 2*. The temporal relationship between Set 1 and 3 is not directly evident based on field data and remote sensing data, and therefore needs to be related to a regional tectonic setting in order to be solved.

In section 5.3.1, the three fault sets are related to regional tectonic events based on their reconstructed paleo-stress regimes. The origin of Set 1 can be associated to: a) the Sveconorwegian collapse at c. 850 Ma *or* b) the Caledonian collapse at c. 400 Ma. The only tectonic event of regional significance that can be related to the transpressive faulting in Set 2, is an early stage of the Caledonian orogeny at c. 450 Ma. Since Set 2 is interpreted to post-date Set 1 as a reactivation, Set 1 must have been present at the initiation of the Caledonian orogeny. Based on this relation, an origin of Set 1 associated to the Caledonian collapse less likely. Conclusively, Sveconorwegian collapse is confirmed as the *most viable* origin of Set 1 faulting, in agreement with the top-to-the SE extensional movements along the P-K shear zone (Mulch et al., 2005). Nevertheless, from a tectonic point of view, a reactivation of both Set 1 and 2 associated to the Caledonian collapse is *possible*. Faults of Set 1 and 2 dominantly strike NE–SW which is at an optimal orientation of the NW–SE extension of the Caledonian collapse. However, no direct evidence of a reactivation at this time was observed in the field data. Another result of temporal significance for NE–SW striking faults of Set 1 and 2, is the fault gouge from the NE–SW striking fault located in the northern part of the study area. The gouge is dated to c. 220 Ma, which relates to a late Triassic extension. It remains unknown if a reactivation of NE–SW faults occurred in both Set 1 and Set 2.

The faulting in Set 3 may be associated to: a) the rifting of Rodina (early to late) at c. 615 Ma to c. 518 Ma and/or b) an extensional regime in late Permian to early Triassic and is *most likely* a reactivation of a pre-existing ancient fracture system of Pre-Sveconorwegian (Gothian) origin. Both these regional tectonic events pre-date the late Triassic reactivation of NE–SW faults of Set 1 and 2, and are therefore viable in terms the temporal constraint applied by cross-cutting relationships. The extensional period associated to the rifting of Rodinia, and the igneous intrusions such as the Egersund dikes and the Fen complex, is considered more likely in causing the faulting of Set 3. This conclusion is based on the proximity of the Fen complex to the studied area, as well as the well-constrained NW–SE extension which corresponds well to the reconstructed paleo-stress regime of Set 3. A reactivation of Set 3 resulting from a later Permian to early Jurassic extension still remains possible from a regional tectonic point of view – but is not supported by any direct field evidence.

Based on the results from this study, the *most viable* tectonic evolution of Drangedal and Nome is presented in *5 stages* (Figure 59). *Stage 0* includes an ancient fractured bedrock of pre-Sveconorwegian (Gothian) origin. This stage is not kinematically represented in the field data, but likely provided necessary pre-existing NW–SE striking planes of weakness for later Set 3 faulting. *Stage 1* consists of Set 1 faulting associated with the Sveconorwegian collapse around 850 Ma. *Stage 2* consists of Set 3 faulting associated with rifting of Rodinia (early to late stage) between 615 Ma and 518 Ma, likely as a reactivation of the fractured bedrock described in Stage 0. *Stage 3* consists of Set 2 faulting, interpreted as a reactivation of pre-existing NE–SW faults of Set 1, associated with the early stage of Caledonian compression around 450 Ma. This stage is interpreted

to cause an overprinting of Set 1 slip-lines by Set 2 slip-lines. Finally *Stage 4* consists of a reactivation of NE–SW faults of Set 1 and/or 2 occurring at c. 220 Ma (based on dated fault gouge) and is associated to Late Triassic regional extension. Stage 4 may extend back to the Permian, during the opening of the Oslo and Skagerrak rifts. A schematic representation of this evolution is given in Figure 59.

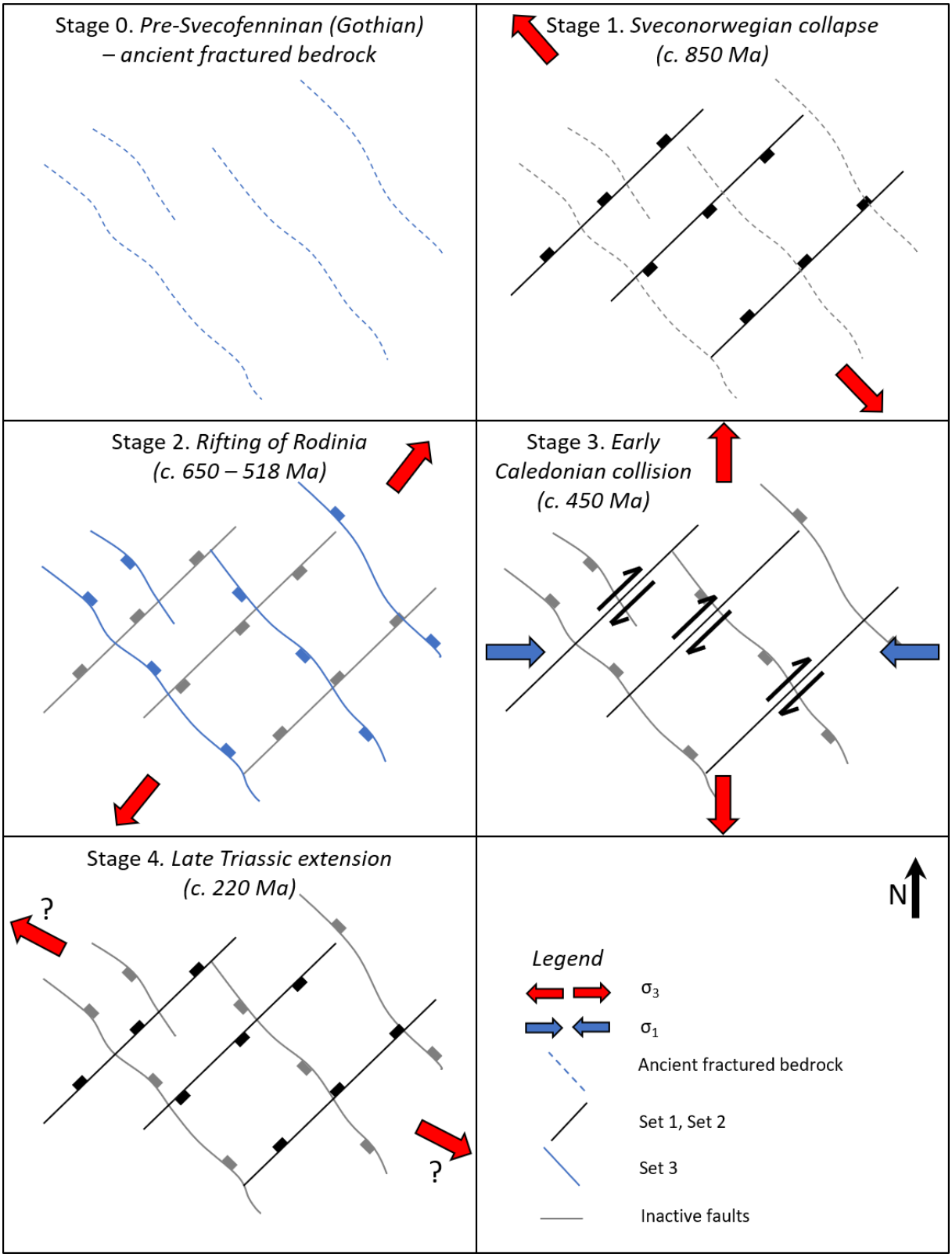

Figure 59. Proposed tectonic evolution of the brittle bedrock features of the studied area in Drangedal and Nome; Set 1, 2 and 3.

5.3.4 Comparison with proposed evolution of lineament study

In the lineament study (Hilde Gunleiksrud, 2017), the three *lineament populations* were integrated into a regional tectonic setting*,* also aiming to describe the brittle evolution of Drangedal and Nome*.* The general trends of the proposed evolution were similar to the proposed evolution in the current study. *Pre-Sveconorwegian (Gothian) deformation*, *Sveconorwegian collapse*, *rifting of Rodinia*, *Caledonian collapse* and *Carboniferous to Triassic extension* are all proposed to be of tectonic significance (to varying degree) in both the lineament study and the current study. Caledonian compression associated to the dextral-oblique slip of the NE–SW faults of Set 2 is, however, not included as an influential regional-tectonic event in the lineament study. This provides an example of shortcomings related to using solely remote sensing in reconstructing brittle deformational evolution. Structural field data is essential in identifying fault kinematics to reconstruct paleo-stress regimes and ultimately relate these to regional-tectonic events. Nevertheless, a general similarity between results of the current study and the lineament study shows the value and relevance of doing a lineament study based on remote sensing as a preparation for an in-depth study including structural field data.

5.3.5 Comparison of studies

Scheiber and Viola (2018) conducted a multiscalar study of the brittle faults and fractures of the Bømlo islands based on remote sensing and field structural data. By paleo-stress inversion, mineralogical characterization and radiometric K-Ar dating, Scheiber and Viola (2018) present a time-constrained tectonic model of the local and regional brittle evolution. The methodological approach by Scheiber and Viola (2018) is similar to the one applied in this thesis, providing a good basis for comparison. In terms of geographic relations, both studies are located in southern Norway, making it relevant and interesting to compare the results obtained in this thesis to those of Scheiber and Viola (2018). The bedrock in the current study area is of Proterozoic origin, whereas the rocks exposed on the Bømlo islands are of a Caledonian origin. In comparing the results of the two studies, pre-Caledonian deformation (Stage 1, 2 and 3 in the current study) is therefore not relevant.

Scheiber and Viola (2018) propose that Caledonian NNW–SSE transpression and Scandian ESE–WNW compression generated the earliest stages of brittle faulting and fracturing of the Bømlo islands. These faults were dominantly ESE–WSW-striking dextral strike-slip faults, NW–SE-striking strike slip-faults and ENE–WSW-striking thrust faults (Scheiber & Viola, 2018). In this thesis, Set 2 faults are suggested to have a Caledonian origin at c. 450 Ma (Figure 59). Set 2 includes NE–SW-striking dextral strike-slip faults and some NW–SE-striking sinistral strike-slip faults (Table 1), which do not resemble any of the Caledonian faults of the Bømlo islands as proposed by Scheiber and Viola (2018). However, Set 2 faults of the current study are interpreted as a reactivation of pre-existing faults (Set 1), and may therefore exhibit a non-optimal orientation in terms of the Caledonian compression. The Bømlo faults of Caledonian and Scandian origin vary in orientation, but likely provide a more optimal representation of the tectonic stress regime at this time.

A NW–SE extension resulting from the Caledonian collapse generated variably oriented faults in the Bømlo islands (Scheiber & Viola, 2018). In the current study, a Caledonian influence is discussed in association to a potential reactivation of Set 1 and 2 faults. However, due to lack of direct field evidence of such a reactivation, the Caledonian collapse is not included in the final proposed tectonic evolution (Figure 59). Due to the distal location of Drangedal and Nome to the main orogenic activity of the Caledonides

(Figure 5), the Caledonian orogeny and collapse were likely of greater influence in Bømlo than in the current study area.

Scheiber and Viola (2018) propose that the NW–SE- to NE–SW-striking normal faults of Bømlo result from rifting phases of Permian to Middle Triassic. A reactivation of these faults and faults of Caledonian origin is interpreted to have occurred from Late Triassic to Early Jurassic and is associated to an extensive formation of incohesive fault gouge (Scheiber & Viola, 2018). This corresponds well to a Late Triassic reactivation of NE–SW faults (Set 1 and/or 2, Figure 59) in the current study, which is also characterised by formation of incohesive fault gouge.

Generally, the results of the two studies present a deformational evolution of similar character from the early phase of the Caledonian collision until the late rifting phase of the Mesozoic. Since the bedrock in Drangedal and Nome is of older origin, the faults studied in the current study are characterized by a greater degree of reactivation and do not necessarily optimally oriented in terms of the tectonic stress fields. Therefore, the faults in the current study and those of the Bømlo islands cannot be directly related in terms of spatial orientation although they can be related temporally (post-Caledonian).

5.4 Magnetic modelling

5.4.1 Model responses

Eight 2D models (Figure 45 to Figure 55) along a transect across the anomaly associated to the Fisarbakken lineament anomaly are constructed to test which magnetic response of various fault concepts corresponds best to the observed magnetic field. The success of the models is determined by how well the calculated response-curve coincides with that of the observed and is quantified by the *model error.* Table 4 lists the various models from lowest to highest error. The success of the models is also determined qualitatively by how well the shape of the calculated field represents the observed one.

Model	***Fault geometry***	***Susceptibility-reducing mechanism***	***RMS Model error (nT)***
8	fault zone	deep weathering + hydrothermal alteration	5.0
4a	fault zone	deep weathering	7.3
6	fault zone	hydrothermal alteration	11.0
3	single fault	deep weathering	14.4
5	single fault	hydrothermal alteration	17.2
7	single fault	deep weathering + hydrothermal alteration	17.5
2 (Reference)	no fault	--	20.6

Table 4. Overview of the various models sorted by their error-value, from lowest to highest. The errors are given by the deviation of the calculated response from the observed response. The fault geometry and susceptibility-reducing mechanism are also given, to illustrate the general trends of the models.

All models with *fault zones* consistently produce calculated responses which resemble the observed response better than the models with a *single fault*. This is demonstrated in Table 4, in which all the models constructed with a fault zone are associated to lower error than the models constructed with a single fault.

Upon comparing the three models containing fault zones (Figure 48, Figure 52 and Figure 55, Table 4), the models in which deep weathering is a susceptibility-reducing mechanism (Model 4a and 8) produce significantly better responses than Model 6, in which hydrothermal alteration is the only susceptibility reducing mechanism. Due to the assumption that the effect of hydrothermal alteration is greatest at depth and reduces towards the surface, the profiles of reduced susceptibilities are wide at great crustal depths and become narrow towards the surface (Figure 60C). Accordingly, shallow crustal depths in Model 6 contains insignificant volumes of magnetic contrast relative to models 8 and 4a (Figure 60). Since the magnetic response is most sensitive to magnetic contrasts at shallow depth, the volume of shallow low-susceptibility rocks in Model 6 is simply not sufficient to produce a response that mimics the observed anomaly response.

Of all eight models, Model 8 (Figure 55) and 4a (Figure 48) appear to be the most successful models. These models produce calculated magnetic responses that resemble the observed magnetic response well, with small errors of 5 and 7 nT. As a reference, an error of 21 nT is associated to Model 2, in which no fault is incorporated. Model 8 combines hydrothermal alteration and deep weathering as susceptibility reducing

mechanism, whereas Model 4a only incorporates deep weathering as a susceptibility reducing mechanism.

Model 4a (Figure 48) has a model error that is only slightly larger than Model 8 (Figure 55, Table 4). In fact, the calculated responses for the two models are so similar, that solely in terms model error, Model 4a and 8 nearly represent the observed anomaly response equally well. However, assuming that field observations and petrophysical samples from outcrops of localities 49 and 66 are correct and representative for the Fisarbakken lineament, both deep weathering and hydrothermal alteration exist in conjunction with one another. These observations support the feasibility of the combined presence and effect of hydrothermal alteration *and* deep weathering in the fault zone. Conclusively, Model 8 is regarded as the most viable model to explain the anomalous signature of the Fisarbakken Lineament.

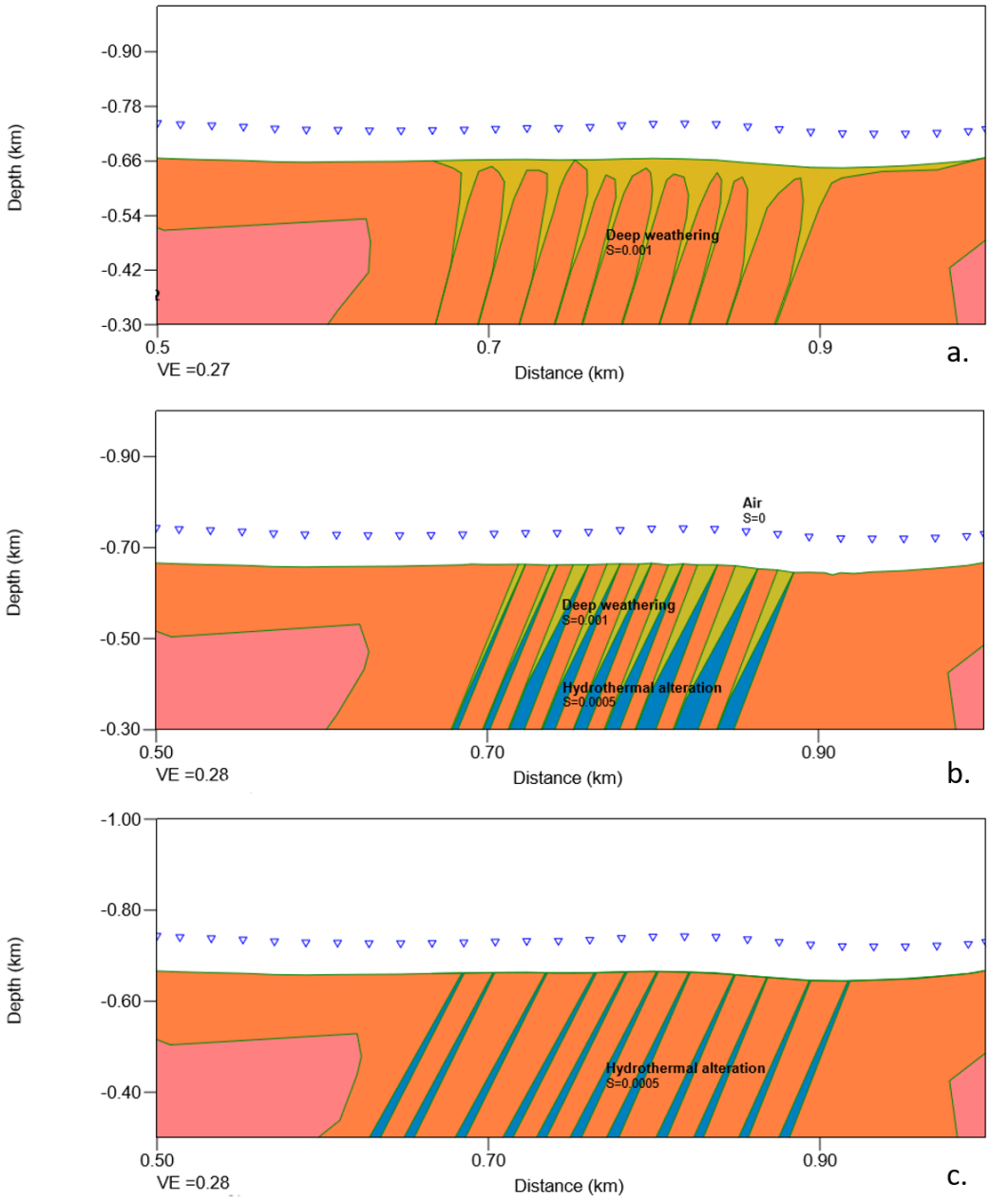

Figure 60. Shallow crustal levels of models 4a (a.), 8 (b.) and 6 (c.). Illustrates details of susceptibility reduction in fault profiles close to the surface. S: susceptibility, VE: vertical exaggeration.

5.4.2 Assumptions and limitations of the models

Relevant field observations and rock samples assist in constraining the structural, geometrical and petrophysical framework for the 2D model of the anomaly associated to the Fisarbakken lineament. Various models were constructed in to test and evaluate different fault concepts, representing different tectonic scenarios. Model 8 is determined to best resemble the observed magnetic field over the Fisarbakken lineament. This section describes the assumptions and limitations associated with the models, with a focus on Model 8, and discusses how these affect the feasibility of the model.

The c. 17 km long Fisarbakken lineament has a relatively uniform signature and a very linear character. Therefore, there is reason to believe that structural and petrophysical characteristics should remain relatively constant throughout the entire lineament. Consequently locality 49 can be assumed to be representative for the modelled profile, although locality 49 and the profile are located c. 1 km apart along strike. The structural features (fault plane orientations, slip-lines and fractures) observed at locality 49 (e.g. Fault A, Figure 42) correspond to the fault data of Set 1 observed throughout the entire studied area. Therefore, it seems reasonable to believe that these structural features are of significance also along the modelled profile, which is partly confirmed by the asymmetry of the magnetic anomaly over the lineament, indicating a dipping structure. A fault zone consisting of a series of faults dipping steeply towards NW is introduced based on these structural assumptions. A maximum width of the fault zone is determined based on the distance between fractured and faulted outcrops on either side of the anomaly, approximately 180–250 m. (The area between these two outcrops was overgrown). With this as a constraint, an 'ideal fault zone width' of 180 m is incorporated in Model 8. This 'ideal fault zone width' was determined based on the width at which the calculated response resembled with the observed response. However, this width will vary based on several other properties as well; the width of the individual faults, the vertical extent of deep weathering, and the contrast in susceptibility values between the fault rock and the surroundings.

The width of the individual faults (or rather, width of susceptibility reduction within each fault), in Model 8 is between 5 and 15 m. These widths are largely determined also by how well the calculated curve resembles the observed curve. Fault A at locality 49 serves as a proxy for the faults of the Fisarbakken lineament. The weathered fault core of Fault A is 1 m thick, which is narrower than what is modelled. However, assuming a combination of deep weathering *and* hydrothermal alteration, a wider combined zone of reduced susceptibility may be feasible. It is also likely that the faults located along the centre of the lineament are of greater width relative to faults located at the flanks. In terms of hydrothermal alteration alone, an altered zone of c. 10 m is feasible. Meller et al. (2014) found through a study of hydrothermally altered zones in granite that alteration zones around fractures could reach a lateral extent of up to tens of metres.

The vertical extent of the deep weathering within the faults is determined by the point at which the minima of the calculated response coincides with the minima on the measured magnetic field. Model 4a determine this depth to be of c. 250 m. This depth is largely dependent on the susceptibility of the weathered material. A sensitivity test is conducted in Model 4b, by introducing an increased susceptibility to the weathered profile, thereby decreasing the magnetic contrast between the background and modelled fault zone. A three-fold increase in the susceptibility of the weathered material (from 0.001 SI to 0.003 SI) results in model where the vertical extent of weathering is three times greater than the initial model (Model 4a). This effect depends significantly on the geometry of the

weathered profiles. Since the calculated response is more sensitive to shallow bodies than deeper ones, the very narrow weathering profiles at depth are not as influential on the calculated response as the wider profiles at shallow depths. Accordingly, the depth at which the gradually narrowing weathering profiles extend is somewhat uncertain. Nevertheless, the sensitivity test proves that varying susceptibility values of the weathered material has significant implications on the model depth of the weathering profiles and demonstrates that uncertainties associated to susceptibility values need to be considered.

Sample 528 from the weathered core of Fault A, with a susceptibility of c. 0.001 SI, is assumed representative for the deep weathered material in the fault zone. Through processes of exhumation and erosion, this material is now exposed at the surface. The original properties of the deep weathered rock are also altered by surface weathering conditions. The susceptibility may therefore not be entirely representative of material weathered exclusively at depth. Another uncertainty associated to susceptibility values arises from a statistical point of view; the susceptibility of the deep weathered material should ideally be based on more than one sample. The samples assumed representative for hydrothermal alteration (samples 530 and 539) are collected from localities 49 and 66. Although these two samples are collected from opposite ends of the Fisarbakken lineament, both give a noticeably similar susceptibility of 0.0005 SI. This provides a fair statistical strength. However, uncertainty due to a low statistical basis is an issue also here. Although the significant low susceptibility of samples 530 and 539 are thought to result from hydrothermal alteration, this should be confirmed with proper mineralogic analysis comparing magnetite-to-hematite ratios of altered and unaltered rock. Such analysis is not conducted in this study.

The background susceptibility of the granitic gneiss on either side of the anomaly was assumed based on an average value of pristine granitic gneiss sampled from both the north and south side of the Fisarbakken lineament. Bodies of lower susceptibilities were introduced as a framework outside of the anomaly to accommodate for the fluctuations in the measured response (Model 2, Figure 46). The susceptibilities of these bodies are based on measured petrophysical data collected from granitic gneiss throughout the study area and are thus within a representative range of values. The distribution and geometries of these bodies, however, are purely hypothetical. The background susceptibility in the model influences the modelling of the fault zone. A different background framework may therefore lead to a different conceptualization of the fault zone than that of Model 8.

The measured total magnetic field is a cumulative response from subsurface properties. This means that sources to the magnetic response may also result from deeper subsurface features that cannot be hypothesised from outcrop observations. Alternative explanations for the magnetic anomaly are different types of magnetic contrast, situated at a larger depth and possibly related to a lithological contact with magnetic properties varying from those of the granitic gneiss. To investigate this possibility, neighbouring lithological domains are considered. The Nissedal Supracrustals (amphibolites) are located just south of the Fisarbakken lineament, and generally have a lower magnetic signature than the granitic gneiss of the Vråvatn complex (Figure 8). The Nissedal Supracrustals dip towards the SE, away from the Fisarbakken lineament, and will therefore not introduce a lithological and magnetic contrast beneath the anomaly.

5.4.3 Conceptual model

Despite uncertainties related to assumptions made in the modelling process, Model 8, incorporating a fault zone affected both by deep weathering and hydrothermal alteration, is regarded as the *most viable* model.

Structurally, the NE–SW striking Fisarbakken lineament is associated to the Set 1 fault population observed throughout the studied area. The correspondence to Set 1 is determined based on a) the strike of the lineament and b) lineations on striated fault planes of Fault A, which is assumed representative for faulting along the lineament. Set 1 faulting is interpreted to have initiated in an NW–SE extensional regime associated to the collapse of the Sveconorwegian orogeny at c. 850 Ma. The NE–SW faults of Set 1 likely experienced several reactivations. It is reasonable to assume that a major structure like the Fisarbakken lineament also experienced reactivation. In fact, faults representative of Set 2 faulting are also observed at locality 49. The NE–SW faults of Set 2 is interpreted as a reactivation of pre-existing Set 1 faults by an E–W transpressive regime – likely associated to an early phase of the Caledonian orogeny at c. 450 Ma. A fault gouge from a NE–SW striking fault within the study area is dated to c. 220 and provides evidence for yet another reactivation of NE–SW faults – perhaps also of the Fisarbakken lineament.

Hydrothermal alteration is caused by the circulation of O_2-rich fluids heated by a subsurface source. Periods of increased magmatic activity associated to rifting phases may serve as a thermal source in a hydrothermal system (Sharma & Srivastava, 2014). Towards the end of the Sveconorwegian orogeny (Early Neoproterozoic), the gneiss complexes and supracrustal sequences of the Telemarkia lithotectonic unit were intruded by granitic plutons (Bingen et al., 2003). In the studied area of Drangedal and Nome, this corresponds to the Tørdal granite intruding the Vråvatn Complex and the Nissedal Supracrustal Complex (Andersen et al., 2007). The intrusion of these granitic bodies likely provided a sufficient thermal source for hydrothermal alteration to occur in the Drangedal and Nome area. For hydrothermal alteration to occur in fault zones, the heated O_2-rich fluids must be able to circulate along fault and fracture-planes. Tectonic activity will create a network for fragments in a fault zone, thereby increasing the permeability and allowing fluids to circulate. Faults of Set 1, including the Fisarbakken lineament, are proposed to originate in the Neoproterozoic, around 850 Ma, slightly postdating the magmatic activity associated to the intrusion of the Tørdal granite. Conclusively, the thermal activity *and* faulting of the NE–SW faults occurring in the Neo-proterozoic, facilitated fault zone 'environments' in which hydrothermal alteration could occur.

In addition to causing susceptibility reduction within fault zones, hydrothermal alteration has a sealing effect on fractures within the faults, preventing further alteration until another tectonic event occurs to re-fracture the fault zone. Such a sealing will also prevent deep weathering processes by blocking meteoric water from percolating into the fault zone. However, in the assumed concept of Model 8, both hydrothermal alteration *and* deep weathering influence the fault zone. Assuming a hydrothermal alteration and sealing of fractures occurring in the Neoproterozoic, deep weathering processes must have occurred *after* a reactivation and re-opening of fractures within Fisarbakken fault zone. Reactivations are assumed in relation to the early phase of the Caledonian orogeny (Set 2) and a late Triassic extensional regime (Set 1 and/or Set 2). Another significant temporal constraint regarding the deep weathering process, is the climatic environment. Saprolitization occurs in tropical climates, which for Scandinavia means that this may have occurred in the Mesozoic (Brekke & Olaussen, 2007). By the late Triassic, basement

rocks of southwestern Scandinavia were exposed to an intense weathering (Fredin et al., 2017). In 2017, the BITE-team collected a sample of deep weathered material from a fracture in the southern part of the study area. This weathered material was dated to c. 150 Ma corresponding to a Cretaceous age (Torgersen, pers. comm., 2018). Using this as a proxy, the deep weathering assumed in the Fisarbakken fault zone may also have occurred in the Cretacous, after the late Triassic reactivation of NE-SW faults within the studied area.

Considering a significant erosion and uplift influencing the morphology over the past c. 220 Ma, a conceptual pre-erosive deep weathering-profile must have extended to greater depths than the extent of erosion so that the weathered rock could have been preserved in the fault zone until today. Rohrman et al. (1995) suggests two influential periods of uplift and erosion in southern Norway, the first in Triassic to Jurassic time, and the second starting at the end of the Oligocene. Assuming deep weathering in the Fisarbakken fault zone occurred in the Cretaceous (based on the sampled deep weathering material in the southern part of the study area), the first period of uplift and erosion proposed by Rohrman et al. 1995 will *predate* the deep weathering process. This period is therefore not of relevance when conceptualizing the pre-erosive deep-weathering profile. The second phase of uplift and erosion proposed by Rohrman et al. (1995), however, *postdates* a Cretaceous weathering and therefore needs to be considered. Through APFT calculations, the total uplift and erosion starting in the late Oligocene and including the latest glacial erosions, is quantified between 500 m and 1.5 km (Rohrman et al., 1995). Model 8 estimates a *current* vertical extent of deep weathering to c. 250 m. Combining this estimate with an assumed uplift and erosion between 500 m and 1500 m, gives a conceptualized pre-erosive deep weathering profile with a minimum vertical extent of 750 m and a maximum vertical extent of 1750 m. At increased depths, the rate of weathering stagnates, due to a slower circulation of meteoric water. Therefore, a pre-erosive weathering depth in the lower end of the range (750 m to 1000 m) is likely more feasible than the maximum depth of 1750 m.

6. CONCLUSION

This thesis presents a multidisciplinary multiscalar analysis of brittle deformation in southern Norway. Results from remote sensing, structural field data, microstructural data, paleo-stress inversion analysis and 2D forward magnetic modelling analysis are combined to give a regional- to microscope-scale understanding of structures associated with the brittle deformation of the bedrock in Drangedal and Nome, central Telemark.

Although the fieldwork covers a limited area within the entire study area of Drangedal and Nome, a good correspondence in orientations of lineaments and faults makes it reasonable to relate the data acquired by field-work to brittle structures indicated by remote sensing of the entire study area. Based on the structural field data, a paleo-stress inversion identified three paleo-stress regimes of significance in creating the faults observed in the study area of Drangedal and Nome:

- *Set 1*: NE–SW extensional faults generated in a NW–SE extensional regime
- *Set 2*: NE–SW dextral strike- to oblique-slip faults generated in an E–W transpressive regime
- *Set 3*: NW–SE extensional to dextral oblique-slip faults generated in a NE–SW extensional regime

By assessing these paleo-stress regimes and associated fault sets in a regional tectonic setting, the following temporal evolution is proposed:

- *Stage 0: Pre-Sveconorwegian (Gothian)*. Ancient fracturing which is not kinematically represented in the field data, but *likely* provided necessary pre-existing planes of weakness for later Set 3 faulting.
- *Stage 1: Post-Sveconorwegian*. NW–SE extension due to orogenic collapse caused the development of Set 1 NE–SW extensional faults.
- *Stage 2: Rifting of Rodinia.* NE–SW extension causing the development of Set 3 faults – *likely* as a reactivation of ancient pre-Sveconorwegian fractures. It remains uncertain whether the early (e.g. Egersund dyke swarm) or late stage (e.g. Fen complex) was significant.
- *Stage 3: Caledonian collision.* Early E–W compression of the collision caused Set 2 faulting – *likely* as a reactivation of pre-existing tectonic foliation planes and Set 1 faults.
- *Stage 4: Late Triassic regional extension.* NW–SE (?) extension causing reactivation of NE–SW faults of Set 1 and/or Set 2. Possibly initiated in the early Permian with the development of the Oslo Rift.

The largest lineaments in the study area are characterized by significant topographic *and* aeromagnetic signatures (Hilde Gunleiksrud, 2017). These are interpreted as brittle structural features. In an effort to understand the cause of the anomalous magnetic signatures associated with such lineaments, a 2D profile was modelled across the NE–SW striking Fisarbakken lineament – one of the most dominant lineaments (both topographically and magnetically) within the study area. Introducing a combination of deep weathering and hydrothermal alteration as mechanisms to reduce the susceptibility

within a c. 180 m wide fault zone lead to a model that resembles the measured aeromagnetic signature. Integrating these fault-zone mechanisms into a tectonic and geomorphological context, the following evolution of the fault zone in the Fisarbakken lineament is proposed;

1. Early Sveconorweigan magmatic activity causing granitic intrusions to act as thermal sources in a hydrothermal system.

2. NW–SE extension in *Stage 1* to generate faults of the Fisarbakken lineament. A network of open faults and fractures allowed circulation of hydrothermal fluids – causing a reduction of magnetic susceptibility within the fault zone and ultimately sealing the fractures.

3. Regional extension in Late Triassic reactivated the Fisarbakken lineament. Fractures were re-opened and allowed meteoric water to percolate along the fault- and fracture planes.

4. A tropical climate in the Cretaceous caused extensive chemical weathering (saprolitization) across southwestern Scandinavia. Open fractures in the Fisarbakken lineament allowed deep weathering to extend nearly 1 km into the crust.

5. Significant uplift and erosion beginning in the Oligocene removes much of the deep weathering material, leaving the faults of the Fisarbakken lineament with deep weathered material extending c. 250 m below the surface. Below this, the fault rock remains hydrothermally altered.

Results from this multidisciplinary study of Drangedal and Nome show a system of brittle structures which are proposed to originate in the Sveconorwegian orogeny and the rifting of Rodinia, with reactivation occurring in at least two phases, likely associated to the Caledonian orogeny and Permian to Triassic rifting. Throughout this brittle evolution, it is proposed that the faulted and fractured bedrock of the study area was subject to hydrothermal alteration, likely in the Neo-Proterozoic, and tropical deep weathering, likely in the Cretaceous.

7. REFERENCES

Allmendinger, R. W. (2018). Stereonet 10. Retrieved from http://www.geo.cornell.edu/geology/faculty/RWA/programs/stereonet.html

Andersen, T., Griffin, W. L., & Sylvester, A. G. (2007). Sveconorwegian crustal underplating in southwestern Fennoscandia: LAM-ICPMS U–Pb and Lu–Hf isotope evidence from granites and gneisses in Telemark, southern Norway. *Lithos, 93*, 273–287. doi:10.1016/j.lithos.2006.03.068

Angelier, J. (1979). Determination of the mean principal directions of stress for a given fault population. *Tectonophysics, 56*, 17-26.

Angelier, J. (1984). Tectonic analysis of fault slip data sets. *Journal of Geophysical Research: Solid Earth, 89*(B7), 5835-5848. doi:10.1029/JB089iB07p05835

BGS. (2015). System for Integrated Geoscience Mapping (SIGMA). Retrieved from https://www.bgs.ac.uk/research/sigma/home.html

Bingen, B., Demaiffe, D., & van Breemen, O. (1998). The 616 Ma Old Egersund Basaltic Dike Swarm, SW Norway, and Late Neoproterozoic Opening of the Iapetus Ocean. *The Journal of Geology, 106*, 565–574.

Bingen, B., Nordgulen, Ø., Sigmond, E.M.O., Tucker, R., Mansfeld, J., & Högdahl, K. (2003). Relations between 1.19–1.13 Ga continental magmatism, sedimentation and metamorphism, Sveconorwegian province, S Norway. *Precambrian Research, 124*, 215–241. doi:10.1016/S0301-9268(03)00087-1

Bingen, B. & Solli, A. (2009). Geochronology of magmatism in the Caledonian and Sveconorwegian belts of Baltica: synopsis for detrital zircon provenance studies. *Norwegian Journal of Geology, 89*, 267-290.

Brekke, H. & Olaussen, S. (2007). Høyt hav og lave horisonter. In I. B. Ramberg, I. Bryhni, & A. Nøttvedt (Eds.), *Landet Blir Til* (pp. 416-439). Trondheim.

De Caritat, P., Hutcheon, I., Walshe, J.L. (1993). Chlorite Geothermometry: A Review. *Clays and Clay Minerals, 41*(2), 219-239. doi:10.1346/ccmn.1993.0410210

Delvaux, D., & Sperner, B. (2003). Stress tensor inversion from fault kinematic indicators and focal mechanism data: the TENSOR program. Retrieved from http://damiendelvaux.be/Tensor/WinTensor/win-tensor.html

Dons, J.A. & Jorde, K. (1978). Berggrunnskart Skien M 1:250 000.

Falkum, T. (Cartographer). (1982). Geologisk Kart over Norge, Berggrunnskart MANDAL - 1:250 000

Fossen, H., Pedersen, R.B., Bergh, S., & Andresen, A. (2007). Creation of a mountain chain. In I. B. Ramberg, I. Bryhni, & A. Nøttvedt (Eds.), *Landet blir til - Norges geologi* (Vol. 2). Trondheim: Norsk Geologisk Forening (NGF).

Fredin, O., Viola, G., Zwingmann, H., Sorlie, R., Bronner, M., Lie, J.E., & Knies, J. (2017). The inheritance of a Mesozoic landscape in western Scandinavia. *Nat Commun, 8*, 14879. doi:10.1038/ncomms14879

Færseth, R.B., Knudsen, B.-E., Liljedahl, T., Midbøe, P.S., & Søderstrøm, B. (1997). Oblique rifting and sequential faulting in the Jurassic development of the northern North Sea. *Journal of Structural Geology, Vol. , No. , pp., 19*(10), 1285-1302.

Gabrielsen, R.H., Braathen, A.,J.,D., & Roberts, D. (2002). Tectonic lineaments of Norway. *Norwegian Journal of Geology, 82*, 153-174.

Gabrielsen, R.H., Faleide, J.I., Pascal, C., Braathen, A., Nystuen, J.H., Etzelmuller, B., & O'Donnell, S. (2010). Latest Caledonian to Present tectonomorphological development of southern Norway. *Marine and Petroleum Geology, 27*, 709–723. doi:10.1016/j.marpetgeo.2009.06.004

Gabrielsen, R.H., Nystuen, J.P., & Olesen, O. (2017). Fault distribution in the Precambrian basement of South Norway. *Journal of Structural Geology, 108*, 269-289. doi:10.1016/j.jsg.2017.06.006

Geosoft Inc. (2015). GM-SYS version April 26, 2016 – User's manual. Northwest Geophysical Associates Ltd. 101 pp. Retrieved from https://www.geosoft.com/products/gm-sys/

Heeremans, M., & Faleide, J.I. (2004). Late Carboniferous - Permian tectonics and magmatic activity in the Skagerrak, Kattegat and the North Sea. *Geological Society, London, Special Publications, 223*, 157-176.
Henderson, I.H.C., & Ihlen, P.M. (2004). Emplacement of polygeneration pegmatites in relation to Sveco-Norwegian contractional tectonics: examples from southern Norway. *Precambrian Research, 133*, 207–222. doi:10.1016/j.precamres.2004.05.011
Hilde Gunleiksrud, I. (2017). *Multiscalar Lineament Study of the Drangedal and Nome Area Using Topographic and Magnetic Data* Norwegian University of Science and Technology, Norwegian Geological Society. 55 pp.
Hinze, W., Von Frese, R., & Saad, A. (2013). Introduction. In W. Hinze, R. Von Frese, & A. Saad (Eds.), *Gravity and Magnetic Exploration: Principles, Practices, and Applications* (pp. 1-16). Cambridge: Cambridge University Press
Hossack, J.R., & Cooper, M.A. (1986). Collision tectonics in the Scandinavian Caledonides. *Geological Society Special Publications, 19*, 287-304.
Kartverket (Cartographer). (2018). Norgeskart. Retrieved from https://www.kartverket.no
Larsen, B.T., Olaussen, S., Sundvoll, B., & Heeremans, M. (2008). The Permo-Carboniferous Oslo Rift through six stages and 65 million years. *Episodes, 31*(1), 52-58
Li, Z.X., Bogdanova, S.V., Collins, A.S., Davidson, A., De Waele, B., Ernst, R.E., & Vernikovsky, V. (2008). Assembly, configuration, and break-up history of Rodinia: A synthesis. *Precambrian Research, 160*, 179–210. doi:10.1016/j.precamres.2007.04.021
Lidmar-Bergstrom, K., Ollier, C.D., & Sulebak, J.R. (2000). Landforms and uplift history of southern Norway. *Global and Planetary Change, 24*, 211–231.
Marret, R., & Allmendinger, R.W. (1990). Kinematic analysis of fault slip data *Journal of Structural Geology, 12*(8), 973-986.
Meert, J.G., Torsvik, T.H., Eide, E.A., & Dahlgren, S. (1998). Tectonic Significance of the Fen Province, S. Norway: Constraints from Geochronology and Paleomagnetism. *The Journal of Geology, 106*, 553–564.
Miller, H.G., & Singh, V. (1994). Potential field tilt a new concept for location of potential field sources. *Journal of Applied Geophysics, 32*, 213-217.
Miyawaki, R., Momma, K., Yokoyama, K., Shigeoka, M., & Matsubara, S. (2015). Mn-bearing Hellandite-(y) from the Heftetjern Pegmatite, Tørdal, Norway. *The Canadian Mineralogist, 53*, 345-356. doi:10.3749/canmin.1400068
Morley, C.K. (1983). *The Structural Geology of the Southern Norwegian Caledonides in the Oslo Graben and Sparagmite Region.* (Doctor of Philosophy), City of London Polytechnic, Falburgh House, Bigland Street, London, 71 pp
Mulch, A., Cosca, M.A., Andresen, A., & Fiebig, J. (2005). Time scales of deformation and exhumation in extensional detachment systems determined by high-spatial resolution in situ UV-laser 40Ar/39Ar dating. *Earth and Planetary Science Letters, 233*, 375–390. doi:10.1016/j.epsl.2005.01.042
Nemcok, M., & Lisle, J. (1995). A stress inversion procedure for polyphase fault/slip data sets. *Journal of Structural Geology, 17*(10), 1445-1453.
Neumann, E.R., Olsen, K.H., Baldridge, W.S., & Sundvoll, B. (1991). The Oslo Rift: a review. *Tectonophysics, 208*, 1-18.
NGU (2018). 1:250 000 berggrunnskartdatabase harmonisert, unpublished.
Olesen, O., Brönner, M., Ebbing, J., Gellein, J., Gernigon, L., Koziel, J., Lauritsen, T., Myklebust, R., Sand, M., Solheim, D. & Usov, S. 2010: New aeromagnetic and gravity compilations from Norway and adjacent areas – methods and applications*. Petroleum Geology Conference series 7*, 559-586.
Odling, N.E. (1992). RIFT, a model of sedimentary basin evolution of finite rate, non-uniform, pure shear extension of the lithosphere. In R. M. Larsen, H. Brekke, B. T. Larsen, & E. Talleraas (Eds.), *Structural and Tectonic Modelling and its Application to Petroleum Geology, Norwegian Petroleum Society (NPF), Special Publications, 1*, 457-467

Olaussen, S., Larsen, B.T., & Steel, R. (1994). The Carboniferous-Permian Oslo Rift; Basin Fill in Relation to Tectonic Development. *Pangea: GLobal Environments and Resources, 17*, 175-197.
Olesen, O., Dehls, J.F., Ebbing, J., Henriksen, H., Kihle, O., & Lundin, E. (2007). Aeromagnetic mapping of deep-weathered fracture zones in the Oslo Region – a new tool for improved planning of tunnels. *Norwegian Journal of Geology, 87*, 253-267.
Olvmo, M., Lidmar-Bergström, K., Ericson, K., & Bonow, J.M. (2005). Saprolite remnants as indicators of pre-glacial landform genesis in southeast sweden. *Geografiska Annaler: Series A, Physical Geography, 87*(3), 447-460. doi:10.1111/j.0435-3676.2005.00270.x
Park, R.G. (1983). *Foundations of Structural Geology*: Blackie and Son Ltd. Glasgow, 135 pp, 3
Piper, J.D.A. (2009). Uplift and cooling magnetisation record in the Bamble and Telemark terranes, Sveconorwegian orogenic belt, SE Norway, and the Grenville-Sveconorwegian loop. *Tectonophysics, 463*, 185–207. doi:10.1016/j.tecto.2008.10.001
Oxford Instruments, plc. (2018). INCA. Retrieved from https://nano.oxinst.com/products/inca/incamineral
Rodionov, A., Ofstad, F., Stampolidis, A., & Tassis, G. (2014). *Helicopter-borne magnetic, electromagnetic and radiometric geophysical survey in the Hjartdal-Rjukan-Flesber area, Telemark and Buskerud*. NGU Report 2014.052, 29 pp.
Rohrman, M., van der Beek, P., Andriessen, P., & Cloetingh, S. (1995). Meso-Cenozoic morphotectonic evolution of southern Norway: Neogene domal uplift inferred from apatite fission track thermochronology. *Tectonics, 14*(3), 704-718.
Scheiber, T., Fredin, O., Viola, G., Jarna, A., Gasser, D., & Łapińska-Viola, R. (2015). Manual extraction of bedrock lineaments from high-resolution LiDAR data: methodological bias and human perception. *GFF, 137*(4), 363-372. doi:10.1080/11035897.2015.1085434
Scheiber, T., & Viola, G. (2018). Complex Bedrock Fracture Patterns: A Multipronged Approach to Resolve Their Evolution in Space and Time. *AGU, 37*(4), 1030-1062. doi:10.1002/2017tc004763
Sharma, R., & Srivastava, P.K. (2014). Hydrothermal Fluids of Magmatic Origin. In *Modelling of Magmatic and Allied Processes* (pp. 181-208).
Sibson, R.H., & Howard Poulsen, F.R.K. (1988). High-angle reverse faults, fluid-pressure cycling, and mesothermal gold-quartz deposits. *Geology, 16*, 551-555.
Spencer, C.J., Roberts, N.M.W., Cawood, P.A., Hawkesworth, C.J., Prave, A.R., Antonini, A.S.M., & Horstwoodb, M.S.A. (2014). Intermontane basins and bimodal volcanism at the onset of the Sveconorwegian Orogeny, southern Norway. *Precambrian Research, 252*, 107–118. doi:10.1016/j.precamres.2014.07.008
Stampolidis, A., & Ofstad, F. (2014). *Helicopter-borne magnetic and radiometric geophysical at Drangedal, Telemark County*. NGU Report 2014.044, 28 pp.
Torgersen, E. (2018). Personal communication.
Torsvik, T.H., Smethurst, M.A., Meert, J.G., Van der Voo, R., McKerrow, W. S., Brasier, M.D., Walderhaug, H.J. (1996). Continental break-up and collision in the Neoproterozoic and Palaeozoic - A tale of Baltica and Laurentia. *Earth-Science Reviews, 40*, 229-258.
Valle, P., Færseth, R.B., & Fossen, H. (2002). Devonian-Triassic brittle deformcition based on dyke geometry and fault kinematics in the Sunnhordland region, SW Norway. *Norwegian Journal of Geology, 82*, 3-17.
Viola, G., Henderson, I.H.C., Bingen, B., & Hendriks, B.W.H. (2011). The Grenvillian–Sveconorwegian orogeny in Fennoscandia: Back-thrusting and extensional shearing along the "Mylonite Zone". *Precambrian Research, 189*, 368– 388. doi:10.1016/j.precamres.2011.06.005
Voorde, M.T., Flerseth, R.B., Gabrielsen, R.H., & Cloetingh, S.A.P.L. (2000). Repeated lithosphere extension in the northern Viking Graben: a coupled or a decoupled rheology? *Geological Society, London, Special Publications, 167*, 59-81.

Vorren, T.O., & Mangerud, J. (2007). Glaciations come and go. In I. B. Ramberg, I. Bryhni, & A. Nøttvedt (Eds.), *Landet blir til - Norges geologi* (pp. 480-533). Trondheim.

Walderhaug, H.J., Torsvik, T.H., Eide, E.A., Sundvoll, B., & Bingen, B. (1999). Geochronology and palaeomagnetism of the Hunnedalen dykes, SW Norway: implications for the Sveconorwegian apparent polar wander loop. *Earth and Planetary Science Letters, 169*, 71–83.

Žalohar, J., & Vrabec, M. (2007). Paleostress analysis of heterogeneous fault-slip data: The Gauss method. *Journal of Structural Geology, 29*(11), 1798-1810. doi:10.1016/j.jsg.2007.06.009

8. APPENDICES

8.1 Appendix 1

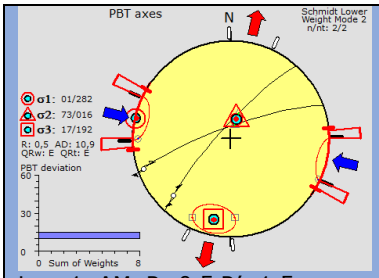

Loc. 1. AM. R=0,5 R'=1,5. Transpression

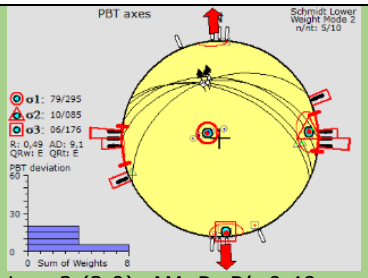

Loc. 2 (2,0). AM. R=R'=0,49. Extension

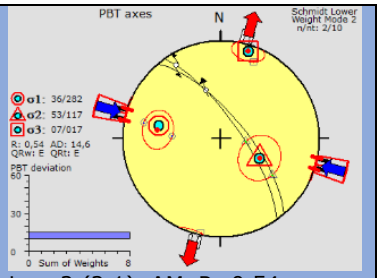

Loc. 2 (2,1). AM. R=0,54 R'=01,46. Extension

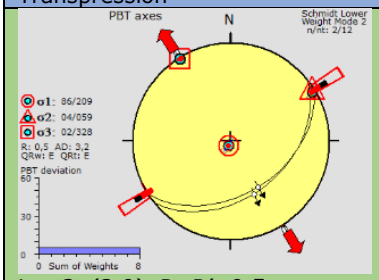

Loc 3. (3,0). R=R'=0,5. Extension

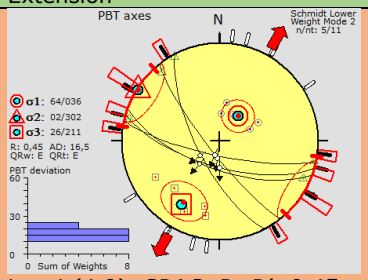

Loc 4 (4,0). GRAG. R=R'=0,45. Extension

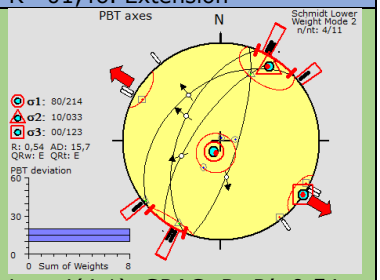

Loc. 4(4,1). GRAG. R=R'=0,54. Extension

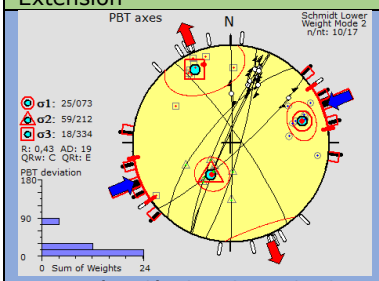

Loc. 14(14,0). GRAG. R=0,43 R'=1,57. Transpression

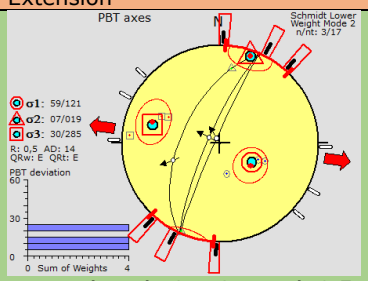

Loc. 14(14,1). GRAG. R=R'=0,5. Extension

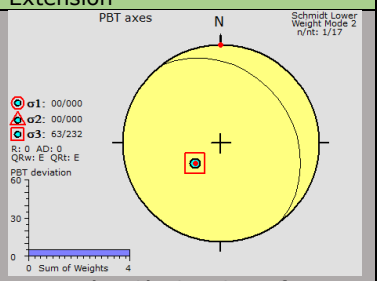

Loc. 14(14,2). GRAG. Mafic intrusion. Undetermined kinematics

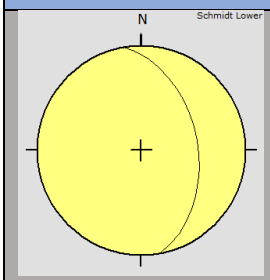

Loc. 17(17,0). GRAG. Weathered fault zone. Undetermined kinematics

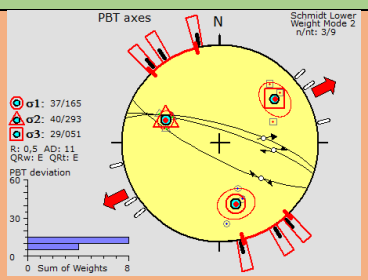

Loc. 17(17,1). GRAG. R=0,5 R'=1,5. Transpression

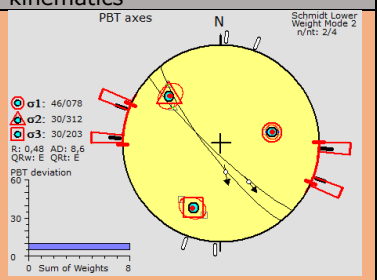

Loc. 18(18,0). GRAG+AM. R=R'=0,48. Extension

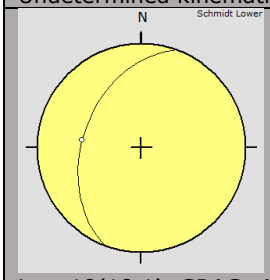

Loc. 18(18,1). GRAG+AM. Undetermined kinematics

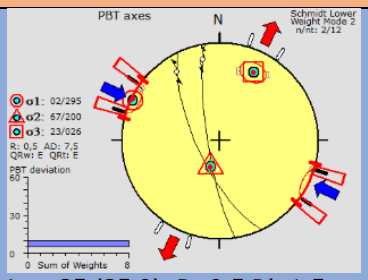

Loc. 35 (35,0). R=0,5 R'=1,5. Transpression

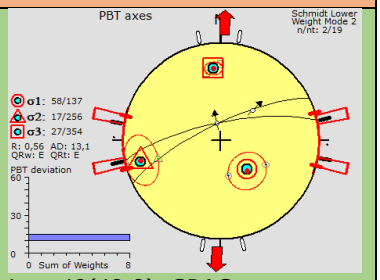

Loc. 49(49,0). GRAG. R=R'=0,56. Extensional

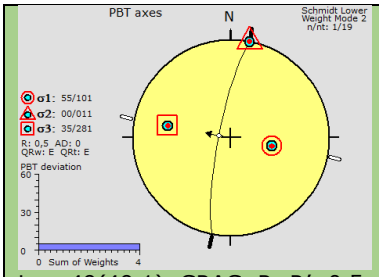 Loc. 49(49,1). GRAG. R=R'=0,5. Extension	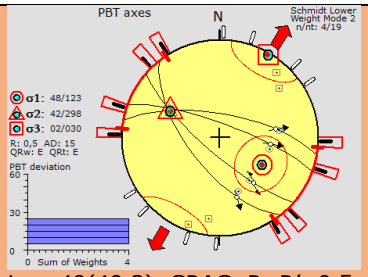 Loc. 49(49,3). GRAG. R=R'=0,5. Extension	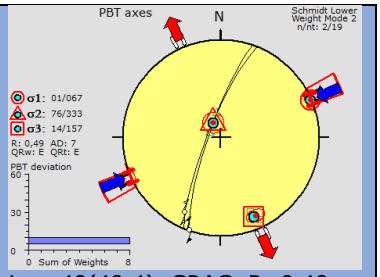 Loc. 49(49,4). GRAG. R=0,49 R'=1,51. Transpression
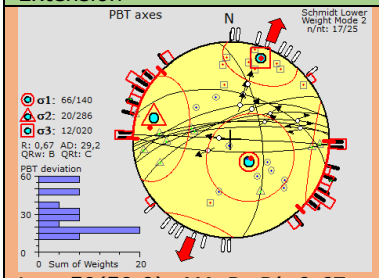 Loc. 59(59,0). AM. R=R'=0,67. Extension	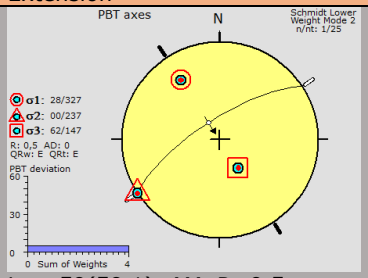 Loc. 59(59,1). AM. R=0,5 R'=2,5. Compression	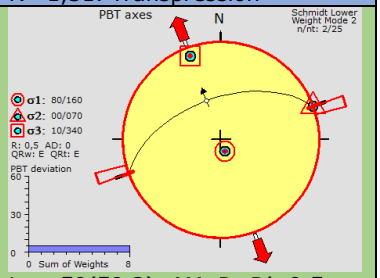 Loc. 59(59,2). AM. R=R'=0,5. Extension
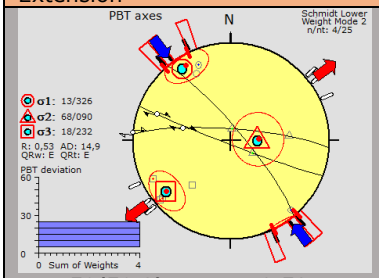 Loc. 59(59,3). AM. R=0,53 R'=1,47. Transpression	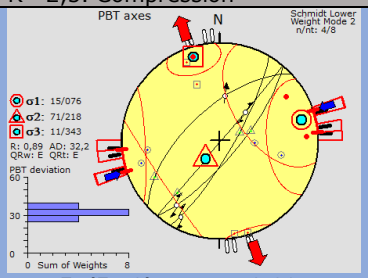 Loc. 57(57,0). AM. R=0,89 R'=1,11. Transtension	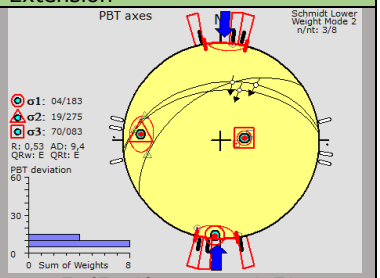 Loc. 57(57,2). AM. R=0,53 R'=2,53. Compression
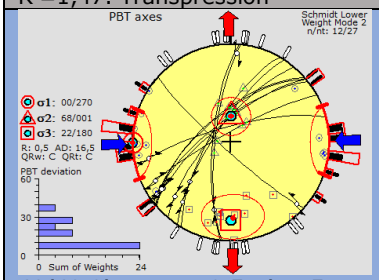 62(62,0). AM. R=0,5 R'=1,5 Transpression	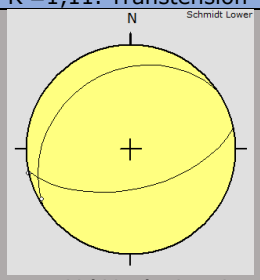 Loc. 62(62,1). GRAG. Undetermined kinematics	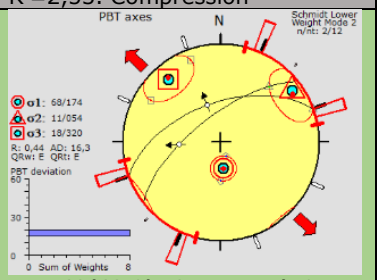 Loc. 63(63,0). GRA. R=R'=0,44 Extension
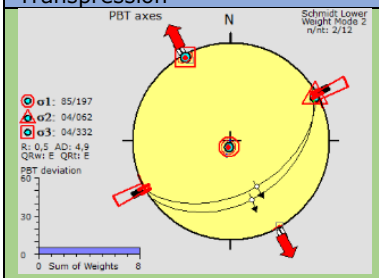 Loc. 73(73,0). GRA. R=R'=0,5 Extension	LEGEND: AM: amphibolite GRAG: granitic gneiss GRA:granite Green: Set 1 Blue: Set 2 Red: Set 3 Grey: miscellanous	

Summary of sub-sets compiled from key localities. Sub-set number is given in brackets behind the locality number. Stress tensors are reconstructed in the Win-Tensor program (Delvaux & Sperner, 2003). Stress regimes (extension, compression, transtension or transpression) are determined based on the stress ratios, R and R'. Based on the sub-sets' stress regimes and the orientations of the stress fields, the sub-sets are grouped into three colour-coded sets. The sub-sets with grey cell colour did not fit into any of the three sets.

Ida Hilde Gunleiksrud

Brittle Deformation in Central Telemark, South Norway

NTNU
Norwegian University of
Science and Technology

NORGES
GEOLOGISKE
UNDERSØKELSE
· NGU ·